NASA-CR-191333

BAUER ASSOCIATES, INC.
ELECTRO-OPTICAL SYSTEMS

P.96

177 WORCESTER RD, SUITE 101
WELLESLEY, MA 02181
TELEPHONE (617) 235-8775
FAX (617) 235-2274

DEVELOPMENT OF A MEASUREMENT OF UPPER MID FREQUENCY ERRORS ON ARBITRARY GRAZING INCIDENCE OPTICS

NASA SBIR Phase II Final Report

Contract NAS5-30311

12/5/90

Author, Principal Investigator:

Paul Glenn

(NASA-CR-191333) DEVELOPMENT OF A MEASUREMENT OF UPPER MID FREQUENCY ERRORS ON ARBITRARY GRAZING INCIDENCE OPTICS Final Report, Oct. 1988 - Oct. 1990 (Bauer Associates) 96 p

N93-20731

Unclas

G3/74 0143391

TABLE OF CONTENTS

LIST OF TABLES

LIST OF FIGURES

I. Introduction

Below we summarize the innovation and general instrument concept, review the original Phase I results, define the Phase II objectives, and give a brief overview of the Phase II results.

I.1 Summary of the Innovation and Instrument Concept

(In this section we discuss the innovation and instrument concept in general terms. We refer the reader to recently published Phase-III-related papers[1,2,3] by this project's Principal Investigator for additional general information.)

The control and therefore the measurement of midfrequency surface errors have become increasingly important. Midfrequency surface errors (i.e., errors midway in spatial frequency between high frequency micro-roughness and low frequency full-aperture figure errors) largely determine the near-image scatter characteristics of high performance visible light systems. Moreover, they are crucial in their effect on scatter and contrast performance of extreme ultra violet and x-ray systems.

The measurement and characterization of these errors have lagged far behind those of micro-roughness and full-aperture figure errors. Micro-interferometers are commonly used to measure micro-roughness with maximum spatial periods on the order of 1 mm, while conventional interferometers are commonly used to measure full-aperture figure errors with typical spatial periods on the order of 100 mm or more. To measure surface errors in the midfrequency range (i.e., errors with periods on the order of 1 mm to 100 mm), the micro-roughness and the full-aperture approaches have been extended with some success. Fringe scanning[4] and slope profiling[5] techniques have also been successfully used. However, further improvements in accuracy and flexibility are desirable[6]. These improvements have been achieved using our innovation - a new curvature profiling technique.

To put this innovative new curvature profiling technique in the context of more conventional techniques, the matrix in Figure I.1 is useful.

As shown, Figure I.1 differentiates the measurement techniques both by the physical quantity being measured, and by whether the measurement is differential (two simultaneous measurements) or non-differential (a single measurement).

In the upper left corner of Figure I.1 are stylus profilometers and interferometers, which measure surface height directly on a point-by point basis. (In reality, these techniques are of course differential in that they compare the test surface height

with that of a known reference. None-the-less, they are not differential in the sense that the test surface is not compared with itself.) In the upper right corner are shearing interferometers and slope-measuring interferometers, which can rightly be thought of as a subset of the shearing interferometers. These techniques measure surface height in a differential manner. In the lower left corner are autocollimators and alignment instruments for x-ray telescopes[7]. Although these specialized instruments are seldom used for generalized surface metrology, they are examples of techniques that measure surface slope directly on a point-by-point basis. The section of Figure I.1 which has been unfilled until now is the lower right corner, for techniques that measure surface slope differentially. Since the differential of slope is curvature (at least in the small angle approximation), these techniques can be called curvature profiling techniques. (Surface height is obtained by numerically integrating the curvature twice.)

Before describing the curvature profiling technique in detail, it is useful to note the primary advantage of measuring curvature. Because of the differential nature, the technique is self-referencing. But, it is self-referencing in a far more important respect than the differential height measuring techniques. This is because slope, even when it is obtained with differential height measurements, is still a relative quantity. In other words, the slope of a test piece can only be defined relative to the slope of the measurement apparatus, just as the local surface height can only be defined relative to the measurement apparatus' height. Curvature, however, is unique because its value is intrinsic to the test piece - it is an absolute as opposed to a relative quantity. This makes the measurement of curvature fundamentally immune to any rigid body drifts in position or angle during the measurement, since such drifts do not affect the measured curvature. As we shall demonstrate, this permits measurement accuracies that are orders of magnitude smaller than the accompanying drifts and scanning errors.

Another inherent advantage to our particular implementation lies in the fact that the detectors are two dimensional. Therefore, we are sensitive not only to the derivative of longitudinal surface slope (i.e, longitudinal curvature), but also to the derivative of lateral surface slope. We have shown in a separate Phase-III-related publication[2] that for anamorphic test pieces, this quantity is proportional to the angular misalignment of the scanning direction relative to the principal axes of the test piece. Therefore, in testing anamorphic optics (including cylinders) where alignment is critical, we can use this quantity not only to sense the misalignment, but also to compensate for its effect on the measured curvature values. The instrument is therefore fully insensitive to alignment errors.

As summarized above, the curvature profiling technique involves measuring the local curvature of the test piece by simultaneously measuring its slope at two slightly displaced locations. As the pair of sensing beams is scanned along the test piece, a profile of curvature is built, from which the height profile is deduced by double integration.

Figure I.2 shows schematically how surface slope is measured at a single point. A pencil beam is reflected by the test piece, through a lens, and onto a position sensitive detector at the lens's focal point. The position of the focused spot on the detector is proportional to the slope of the incident beam, and therefore also to the local test piece slope.

Figure I.3 shows schematically how the slope measurement is made differential. A calcite plate is added before the test piece to produce two parallel beams of opposite linear polarization. (The incoming beam can be circularly polarized, or linearly polarized at a 45-degree angle.) After being reflected by the test piece and focused by the lens, the beams are separated by a polarizing beam splitter, and focused onto separate detectors - one for each beam on the test piece. The difference between sensed positions on the detectors is thus proportional to the difference in test piece slope at the two measurement locations.

Figure I.4 shows schematically some of the more important features incorporated in our design. Figure I.4 follows the actual mechanical layout generally, showing a steering mirror inside a measurement arm (enclosed by a dotted line), rigidly attached to the main instrument body (also enclosed by a dotted line). In the normal measurement mode, the entire instrument (including the main body and the measurement arm) is scanned along the test piece.

The first important feature in Figure I.4 is the steering mirror shown immediately before the test piece. The steering mirror is moved under closed loop electronic servo control in both axes so as to keep the focused spots centered as well as possible on the two detectors. This maintains an essentially constant incidence angle on the test piece, and uses the detectors in their best characterized and most accurate regions. Most importantly, since the steering mirror operates on both beams simultaneously, it has no effect on the differential measurement. In short, the steering mirror is used to maintain the intended viewing geometry on the test piece, while not degrading (and in fact enhancing) the measurement accuracy. Using an all-flexure support system, we have implemented the steering mirror so that it can steer the beams over a $\pm$30 degree range in both directions over a 30 Hz bandwidth. This allows the instrument to accommodate optics as fast as F-0.5, while easily compensating for any reasonable jitters and drifts. A further important benefit of the steering

mirror is that it can be used in an open loop mode to find the test piece - i.e., to perform automatic self alignment. The steering mirror is simply steered under computer control in an expanding pattern until the beams land on the detectors. The steering mirror is then returned to its closed loop mode. Using this technique, we have found that we can quickly compensate for alignment errors in the range of degrees.

The second important feature shown in Figure I.4 is the movable nature of one of the detectors. This is used to accommodate test pieces with a wide range of base radii of curvature, as follows: With the steering mirror temporarily fixed to keep the focused spot centered on the fixed detector, the movable detector is positioned so that it too is centered on its focused spot. The steering mirror is then returned to the mode of trying to maintain centering for both detectors simultaneously. The required displacement of the movable detector can be seen to be proportional to the base radius of the test piece. We have found that test piece radii from approximately 25 mm convex to approximately 25 mm concave can be accommodated using our baseline instrument parameters.

I.2 Phase I Results

During the Phase I effort, we accomplished all of the technical objectives laid out in the original proposal. The results were as follows:

(1) A set of quantifiable conclusions on the feasibility of the proposed instrument;
(2) Predictions of instrument performance over a wide range of operating parameters; and
(3) A baseline instrument design where the various subsystems were detailed to the level required to demonstrate feasibility and predict performance.

As summarized briefly below, technical accomplishments were in the following areas: (1) systems analysis and engineering; (2) optical design and analysis; (3) mechanical design; and (4) electronic design and analysis.

In the systems analysis and engineering effort, we developed an error budget that supported a 1 Angstrom rms performance level for surface spatial periods from 0.5 to 5.0 mm. In doing this, we developed detailed specifications for the optical, mechanical, and electronic subsystems. We defined appropriate data analysis algorithms, and developed a detailed system performance prediction that showed the instrument's response would be linear and unattenuated over wide ranges of both horizontal scale (down to approximately twice the test beam diameter) and vertical amplitude (from sub-Angstrom features, to features so large that

their rms value over a beam diameter was over one-tenth wave).

In the optical design and analysis, mechanical design, and electronic design and analysis efforts, we followed up on the specification work by designing and analyzing all subsystems to the point required to demonstrate feasibility and predict performance. In the optical design, this meant specifying component quality, showing that exotic optics were not required. In the mechanical design, it meant arriving only at rough (and sometimes conceptual) layouts. In electronic design, it meant coming up with complete, detailed strawman designs (even though they could be expected to change greatly during Phase II), so that detailed noise analyses and performance predictions could be performed.

To summarize, the Phase I study was very successful. We arrived at a general concept for a baseline instrument. Much more importantly, though, we showed by detailed modeling that the full range of testing parameters appeared to be achievable. In particular, we showed the feasibility of achieving (1) 1 Angstrom rms sensitivity; (2) ability to test bare or coated samples; (3) measurable spatial periods from 0.5 mm to 5.0 mm and beyond; (4) testable convex and concave radii from 25 mm on up; and (5) reasonable scanning speeds of several mm/sec.

I.3 Phase II Objectives

There were four overall technical objectives in the proposed Phase II effort:

(1) Demonstrate in hardware the feasibility of the critical subsystems;
(2) Perform the detailed designs for, and fabricate a breadboard instrument using the proven subsystems;
(3) Determine through experimentation the accuracy and operating limits of the instrument; and
(4) Define modifications which would be appropriate for a full laboratory version of the instrument, which could be operated by optical metrology personnel.

We summarize each of these objectives in the following sections. For reference, Table I.1 shows the original schedule and task definitions developed to achieve these objectives.

I.3.1 Subsystem Demonstration

The objective in the subsystems demonstration area was to show in hardware the feasibility of the subsystems which were defined as being critical in the Phase I effort. The three critical subsystems were (1) the detection subsystem (an Acousto Optic Modulator (AOM), a four quadrant silicon detector, synchronous

detection and low pass filter circuitry, and analog processing circuitry); (2) a large range servo subsystem (DC motor driven) to actuate the steering mirror in the direction along the scan; and (3) a small range servo subsystem (piezoelectric crystal driven) to actuate the steering mirror in the direction across the scan.

The reason for demonstrating these individual subsystems before fabricating the full breadboard instrument was to take a conservative technical approach. We had found in the Phase I effort that these three subsystems would determine both the accuracy and the range of operating parameters of the instrument. Therefore, while the basic feasibility of the subsystems was shown in Phase I, we felt that the performance of the subsystems should be demonstrated explicitly in hardware before completing the entire breadboard instrument.

I.3.2 Breadboard Instrument Design and Fabrication

Simply stated, the objective here was to perform the detailed designs for, and fabricate a complete breadboard instrument using the proven subsystems. This was intended to be an iterative effort, using the results of the performance assessment effort to define minor reconfigurations. For reference, Table I.2 lists the various subsystems and aspects of the breadboard instrument, and the corresponding technical goals originally envisioned for the Phase II effort. (Not surprisingly, these goals were traded off against one another and changed during Phase II.)

I.3.3 Performance Assessment

The objective here was to determine through experimentation the accuracy and operating limits of the instrument. This was to be an iterative effort whose results would define minor reconfigurations for the design and fabrication efforts.

As opposed to the subsystem performance assessment, where we would restrict ourselves to tests that not involving a real test piece, here we would be selecting and using real test pieces. These could include a variety of research grade spherical, aspherical, and cylindrical lenses and mirrors, as well as (possibly) surfaces from actual Extreme Ultra Violet (EUV) telescopes such as SEUTS, or X-ray telescopes such as the Advanced X-ray Astrophysical Observatory Technology Mirror Assembly (AXAF-TMA).

We were to perform the experiments on test pieces in such a way that we could determine the repeatability, sensitivity, and accuracy of the instrument. Repeatability was to be determined by measuring each of the samples several times in the same position. Sensitivity and accuracy were to be determined using

various methods. For example, we could test the sensitivity and accuracy by making multiple measurement scans which overlap each other.

We were to characterize the repeatability, sensitivity, and accuracy of the instrument as a function of all relative parameters such as scan length, scanning speed, data sampling density, spot size and separation, and test piece radius of curvature and asphericity. The end result was to be a comprehensive set of data defining the instrument's utility as a function of all relevant instrument parameters and test piece parameters. This would aid in the Phase III modification definition effort.

I.3.4 Modification Definition for Phase III

The objective here was to define modifications which would be appropriate for a full laboratory version of the instrument, which could be operated by optical metrology personnel. Issues to be addressed include the parameter ranges which should be accommodated - e.g., spot size on the test piece, separation between the spots, and allowable scanning speeds and lengths as a function of radius of curvature. We expected to find that some of the flexibilities allowed in the breadboard instrument are superfluous, while others need to be broadened further.

I.4 Overview of the Phase II Results

The Phase II project was extremely successful. The critical subsystems (detection and servo) were developed quickly, and they worked reliably at performance levels that were generally more than an order of magnitude better than comparable subsystems in commercial instruments. More importantly, the breadboard instrument as a whole performed remarkably well. Its sensitivity and accuracy were more than an order of magnitude better than the original 1 Angstrom goal within the primary spatial period range of 0.5 mm to 5.0 mm. Finally, we defined a useful set of modifications for Phase III follow-on work. As discussed in Section II.6, we have, using our own R&D and risk funds, already begun some of those modifications, and are pursuing several promising leads for orders for commercial instruments.

II. Detailed Phase II Results

In this section we discuss in detail the results of the Phase II project. We begin with an overview of the electronics used in the two main subsystems (detection and servo), and then discuss the overall subsystems themselves. (For each subsystem, we first describe the electronics in detail, and then discuss the other aspects.) We continue with the breadboard instrument design and fabrication including algorithms and software, and finish with

the performance assessment and Phase III modification definition.

II.1 Electronics Overview

Figure II.1 shows a block diagram of the complete electronics system, with several aspects of the breadboard instrument incorporated as well. The diagram is simplified, but it provides some perspective into the overall operation of the custom electronics.

The Oscillator board generates a 10kHz signal, which modulates the laser and also modulates an auxiliary Light Emitting Diode (LED) mounted directly on the beam-steering mirror. (Beams are modulated to allow for synchronous detection, which reduces noise and rejects ambient light.) The modulated laser light passes through a set of polarization optics which produce a linearly polarized beam oriented at 45 degrees. This beam thus can be thought of as the superposition of two coincident, orthogonally polarized beams. Those beams hit the steering mirror, and then the surface under test. The steering mirror is servo-controlled to have a position appropriate for the beams to retrace their paths after reflection from the test surface.

The test surface typically will create a differing return angle for each of the two beams; the measurement (and interpretation) of that difference is the task of the system. A polarizing beam splitter in the return path diverts each of the two polarized beams to its own photodetector quad diode. If the surface were flat, each beam would hit its photodetector in the same location as the other. The <u>difference</u> between the location of beam A on detector A, and the location of beam B on detector B, is a measure of the curvature of the test piece. Note also that the detectors measure in two dimensions, and thus reflect the ability to characterize not only the curvature of the test piece, but also a quantity that can be shown to be proportional to 45 degree astigmatism. (Not shown is a focusing lens whose focal plane lies at the detectors. This lens assures that the beams' lateral positions on the detectors are proportional to the beams' slope angles, independent of the beams' lateral positions.)

The synchronous detectors provide a very low noise way of converting the signals from the light hitting each photodetector quad diode to a set of four voltages representing horizontal and vertical beam location on the detector. Those four voltages are converted at high speed to numbers by Analog-to-Digital (A:D) converters inside the computer. Those numbers are operated on by the computer to characterize the test piece.

Not included in the diagram is a computer controlled translation stage. That stage allows the characterization of curvature at a large number of points on the test piece by moving the entire

instrument along a straight line over the test piece.

In operation, the steering mirror servo amplifier accepts the same information as the computer, and operates to maintain the spot as close as possible to the centers of detectors A and B.

The extremely high sensitivity of the system makes the active range of the detectors A and B very small; until the laser spot is located someplace on the photodetectors, however, there is no servo information available for moving the spot. Therefore, it is necessary before measuring a test piece to find some position for the steering mirror where the spot falls on the detectors. To accomplish this, a secondary feedback path is provided directly from the LED on the back of the steering mirror assembly through Synchronous Detector assembly C, to the steering mirror servo. This servo path allows the computer to set the steering mirror in any desired position simply by commanding an offset from the voltages from Detector C. The computer uses this capability to "search" for a position where the beam falls on detectors A and B, and then switches the servo over to track either detector A or the average of A and B. Thus, Detector C is provided solely as a means for automating the signal acquisition process, and is not used during actual measurements.

Having given an overview of the electronics, we can now describe in detail the two critical subsystems - detection and servo.

II.2 Detection Subsystem

The first critical subsystem is detection, consisting of the Acousto Optic Modulator (AOM), a four quadrant silicon detector, synchronous detection and low pass filter circuitry, and analog processing circuitry. The three corresponding electronics boards are the Oscillator / Feedback Selector (to provide the modulation and the synchronizing signal for synchronous detection, and also to select the detector signals to be used in adjusting the steering mirror); the Detector Preamplifier (to preamplify the raw detector signals at a detector so as to minimize noise); and the Synchronous Detection board (to perform the synchronous detection on the preamplified signals). We discuss each board in turn below, and then discuss the overall performance of the detection subsystem.

II.2.1 Oscillator / Feedback Selector Board

Figure II.2 shows a block diagram of the Oscillator / Feedback Selector board. The oscillator section consists of a 10kHz analog function-generator type oscillator with distortion-reducing filtering, and a buffer to offset and drive (level and offset adjustable) an AOM modulator which, in turn, controls and modulates the laser beam of the system. The 10kHz signal is

zero-crossing detected to generate a synchronizing signal for the Synchronous Detection circuits of the system described in Section II.2.3. The 10kHz signal is also buffered, level-shifted, and voltage-to-current converted to drive a small LED mounted on the rear of the servo-controlled mirror assembly. The light created by the LED is position-sensed and finally detected by an auxiliary synchronous detector circuit (Detector C) to provide absolute position feedback for the mirror during setup.

The second function of this board is the selection of mirror position feedback signal (determined by the computer with a simple digital interface on this board) from the choices of Detectors A or (A+B)/2 (signals created by the primary laser-beam detectors), or from Detector C (local absolute mirror position feedback). In all cases, the computer is provided with the capability of generating a position offset in both the x and the y directions to provide for position trimming and ease of calibration.

Figure II.3 shows the schematic for the oscillator section of the board. The oscillator consists of two sections of the quad TL074 op-amp, U1. Section 1 is a hysteretic voltage comparator, which switches states whenever the section 2 output exceeds a threshold of +1 or -1 volt (depending on state), while section 2 is configured as an integrator, converting the Zener diode clamped voltage output of section 1 to a positive or negative voltage ramp of about 2 volts per 50 microseconds. The exact integration constant of the second section is adjusted by R4 to provide an oscillation frequency of 10kHz. (See the waveform diagrams on Figure II.3 for a better understanding.) The 10kHz triangle wave resulting from the basic oscillator circuit is approximately waveshaped to a sine wave (about 2% distortion) by CR3 and CR4 diodes, then tightly bandpass filtered to remove the remaining distortion components by an LC filter feedback around section 3 of U1. Section 4 of U1 plus transistor Q1 provide the signal required by the RF driver to the AOM. R51 is an offset trimpot, needed to minimize the distortion of the AOM.

The output of section 3 (a low-distortion 10kHz sine wave) is fed to a zero-voltage threshold comparator (U3, LM311) which creates the synchronizing signal required by the remainder of the system. This synchronizing signal may be jumper-determined inverted by the exclusive-OR 74LS86; the selective inversion allows the choice of zero or first order output from the AOM.

The 10kHz signal is also fed to the "C" detector LED driver, a TL072 dual op-amp. Section 1 of that op-amp is an inverter. Section 2 is driven by the wiper of a potentiometer, R55. One end of R55 is connected to the non-inverted 10kHz signal, the other end to the inverted signal. The potentiometer can be adjusted to feed a signal of either polarity, at any desired

level, to section 2 of the TL072. Section 2 is configured as a voltage to current converter, and results in a low distortion modulation of the mirror-mounted LED. As with the AOM, minimum distortion requires a carefully chosen offset current, controlled by potentiometer R59.

Included on the board, but disabled in this version, is an AOM Automatic Gain Control (AGC) circuit. This function was disabled because of slow beam profile changes caused by changes in the AOM drive level - those slow changes, or drifts, degraded the accuracy of the detector calibration.

The remaining circuitry shown on Figure II.3 is the backplane connector for the board, and the power supply bypassing, shown in one location as an array of capacitors, those capacitors being located adjacent to the indicated IC's.

Figure II.4 shows the schematic for the feedback selector section of the board. The horizontal and vertical feedback signals from the A, B, and C detector boards (which enter the Oscillator board on the backplane connector on Figure II.3) are resistively scaled and summed by resistor array R42. (The array is shown as a thick-film hybrid of equal values. However, in practice, it is an array of resistors selected for appropriate scale factors.) The selection of A, (A+B)/2, or C detectors is by analog switches U6 and U7. The selected feedback signal is buffered by sections 1 and 2 of the TL074 quad op-amp U9. Also summed into the U9 op-amps is a computer generated offset voltage (independent for horizontal and vertical channels) which allows for a trim of the mirror position. The mirror servo operates to reduce to zero the sum of the selected servo control signal and the computer generated offset signal.

To allow for mirror servo circuit configuration, the error signals output from sections 1 and 2 of U7 are inverted by sections 3 and 4. Jumpers for the horizontal and vertical channels allow selection of noninverted or inverted signals for each axis.

The computer controls the servo feedback configuration by means of an 8 bit parallel signal to the board (received on connector J2). The 8 bits are defined in pairs, with each pair resulting in one output bit, detected by the differential receiver U5. One of the four control bits is reserved, a second controls the HOLD function on the sync-detect boards (it freezes the signal to allow simultaneous detection of both the A and B detectors), and the remaining 2 bits define one of four servo feedback conditions: A, (A+B)/2, C, or OFF. The AND gate U8, plus a remaining section of the exclusive OR gate U4 are used to decode the four states to drive the analog switches U6 and U7. A logic truth table is provided in Figure II.4 to clarify the decode

operation.

Note that the input to the differential receiver U5 is resistively biased to define a benign default state (during host system "offline" or bootstrap periods) when the control lines are undefined.

II.2.2 Detector Preamplifier Board

A large-area circular silicon photodiode, scribed to create four equal segments as a quad photodetector, is used to generate an output current from each of the four sections equal to the instantaneous power incident on each section. The laser (or, for photodetector "C," the LED output) is modulated at 10kHz - resulting in an output current from each section likewise modulated at 10kHz. The purpose of the preamplifier is to convert the small photocurrent to a reasonably large voltage, to bandpass filter the resulting signal (rejecting spurious components of the signal, including photodiode leakage currents and any components from stray light), and to send the resulting four signals to the appropriate synchronous detection circuit. Because of the phase-critical nature of the system (described in more Section II.2.3), a phase-trim adjustment is provided to allow static calibration to zero-degree phase behavior at 10kHz.

Figure II.5 shows the schematic for the detector preamplifier board. The common-cathode connection of the photodiode quad is biased to a positive potential by R1 and R2 and filtered by C1. The resulting reverse-bias of the photodetectors reduces (and to a degree stabilizes) the junction capacitance of the diodes, increasing response speed. The anodes of each photodiode connect to their respective op-amps' inverting inputs.

Since the op-amp input sections (section A, pins 1,2,3) are operated in the inverting mode, with the non-inverting input grounded, the anodes of the diodes are at a virtual ground (i.e., maintained by negative feedback) potential. This maintains a constant reverse bias - and a constant junction capacitance - for the diodes.

The op-amp (section A) provides the current to voltage conversion, and the filtering for the signal, and sends its output (with a stability-guaranteeing isolation resistor R4,9,14,19) to the synchronous detector circuit.

There are three feedback loops around the op-amp. The forward path gain of the op-amp as a function of frequency is an intrinsic part of the filter circuit behavior. The junction capacitance of the photodiode is likewise an intrinsic part of the filter circuit behavior. The circuit looks disarmingly simple, but it is not; a full understanding of the circuit

behavior requires either a very good grasp of the complex matrix algebra describing the system, or access to a powerful analog circuit analysis tool, such as Spice or, as used in the system development, MicroCap. Engineers evaluating this circuit (for possible circuit changes) in the future must be aware of the subtle complexities of the circuit, or they are likely first to assume that the circuit can be easily modified for alternative application, then (upon finding the first assumption false) to assume that the circuit cannot work, and find themselves creating a more easily understood replacement with inferior performance.

At high frequencies, the gain of the system is determined by the internal pole of the op-amp compensation network. At low frequencies, the feedback is the non-inverted integral of the section 1 output. (Section 2 is configured as a non-inverting integrator - R5 and C3 define an integrator, up to the frequency where Z(R5)=Z(C3) (amplifier unity gain) - from that frequency up, R6 and C4 define the integration. The circuit has two poles and one zero, the zero canceling (more or less) the pole, with the resultant response being that of a classical integrator.

The feedback loop behavior is, as described so far, a double integration, and thus oscillatory (by design, at the desired center frequency of 10kHz). The oscillation is damped (turning the "oscillator" into a defined "Q" bandpass filter) by the feedback resistance R3.

Unfortunately, the input capacitance of the op-amp and the junction capacitance of the photodetector combine to introduce an additional pole in the feedback loop-gain. This additional pole is canceled (more or less) by a zero introduced by feedback capacitor C2.

The signal through C2 (and thus the location of the response zero) is adjustable for each amplifier section. The exact location of the zero determines the response shape of the amplifier/filter to some degree, but - much more importantly - it allows adjustment of the system phase behavior over a range of about 60 degrees. This phase adjustment is necessary for optimum system behavior.

II.2.3 Synchronous Detection Board

Figure II.6 shows a block diagram of the Synchronous Detection board. The board accepts four 10kHz sine waves (maximum signal level of about 12v p-p) from the photodetector preamplifier board, the signals being proportional to the amount of laser light hitting each quadrant of the diode. The purpose of the Synchronous Detection board is to synchronously detect the signal from each of those diodes, convert the signals to DC, then present the signals to the A:D converter at the computer in the

form

$$\text{Vertical} = K * (A+B-(C+D)) / (A+B+C+D)$$
$$\text{Horizontal} = K * (A+D-(B+C)) / (A+B+C+D)$$

where A, B, C, and D are defined as

A=upper left quadrant signal level
B=upper right quadrant signal level
C=lower right quadrant signal level
D=lower left quadrant signal level

and where K=10v. Note that this provides a possible range of +/- 10v to the A:D converters. Because of the desired system speed, this conversion must be at a reasonably wide bandwidth (>500Hz), while the desired 16 bit conversion accuracy (1 part in 65536) requires the smallest possible noise and spurious response sensitivity for the system.

The noise and bandwidth considerations were addressed as follows:

(1) Use synchronous detection rather than asynchronous Amplitude Modulation (AM) detection for the signals. This reduces noise sensitivity by more than 1.4 times;
(2) Use multiple analog filters to keep the noise bandwidth as small as possible, while maintaining the desired response bandwidth;
(3) Maintain the greatest possible signal level to avoid adding to the input noise;
(4) Use a synchronous sample and hold output circuit to the A:D converters to eliminate aliased introduction of the 10kHz carrier; and
(5) Provide system phase trim capability to maintain the advantage of synchronous detection. (Note, for example, that if the synchronous detection were to be phase-shifted 90 degrees, all signal would be lost.)

Having discussed the basic features of the Synchronous Detection board, we turn to more detailed discussions. For these discussions, refer to Figures II.7 and II.8. Figure II.7 gives the schematic for the filter and the synchronous detector sections discussed in Sections II.2.3.1 and II.2.3.2. Figure II.8 gives the schematic for the normalizer and track and hold sections discussed in Section II.2.3.3 and II.2.3.4.

II.2.3.1 Input Filter

The four quadrant input signals are filtered by a set of four identical 2-pole adjustable center frequency bandpass filters. The filter topology is similar to a Wein-bridge oscillator, with minimum negative feedback at the center frequency, and a Q

determined by positive feedback. The center frequency is trimmed by potentiometers in the input RC network.

The photodetector preamplifier also incorporates 2-pole filtering, and a phase trim to allow setting of the phase relationship to zero degrees, light modulation to output, at 10 kHz. This zero-degree phase relationship is critical to the system behavior.

Because, at the center frequency, the phase of the filter circuit is precisely 180 degrees, and because the oscillator board provides a synchronizing signal at the same 180 degree relationship to the light modulation, the center frequency may be precisely set for each filter by the adjustment of the trim-pots R1, R6, R11, R16 for the ideal full-wave rectified output of the synchronous detector. When the circuit is so adjusted, the filters (all using related sections of a single TL074/AD713J quad op-amp, U1) become effectively identical.

II.2.3.2 Synchronous Detection

The filtered, phase-corrected 10kHz signals are full-wave synchronously rectified by the analog switch U2 and the Quad op-amp U3. When the U2 switches are open, U3 operates as an inverting op-amp with a gain of -1. When the switches are closed, the output of the op-amp may be determined by considering the inverting and the non-inverting behavior independently, then by applying superposition to the result. The inverting gain continues to be -1, while the non-inverting gain is set by equal feedback to inverting input and inverting input to ground resistors at +2. +2 - 1 = +1, the gain when the switches are closed. The phase relationship between the phase-adjusted input signal and the SYNC signal (from the oscillator) controlling the U2 switches is such as to provide a gain of +1 when the input voltage is positive, and -1 when the input voltage is negative. This results in a precise positive full-wave rectification of the input signal.

The advantages of synchronous detection compared to the more typical asynchronous detection become apparent when the phase behavior of the signal is compared to the phase behavior of possible system noise. System noise has a random phase content, while the signal has a known phase content. With asynchronous detection, the detection is independent of the carrier phase - all the signal, and all the noise will be detected with equal efficiency. With synchronous detection, the detection only works for signals in phase with the synchronizing carrier. Since half of the random phase noise contribution will be in phase, and half will be at 90 degrees (and thus undetected), the effective noise power detected is reduced by 50%. (Of course, if the signal is not at precisely the correct phase relationship, its detection

efficiency will likewise drop - thus precise phase control is needed throughout the system.)

The output of the synchronous detector section is a set of four signals, A, B, C and D, proportional to the light falling on each of the photodiode quadrants. This signal consists of a DC component, and an AC component at frequencies which are multiples of the 10kHz carrier, and predominantly even multiples of the 10kHz carrier; the first significant component is at 20kHz.

The rectified (detected) A, B, C, D signal components are resistively matrixed to the required terms by resistor network R28 and quad op-amp U4. (Note the use throughout the circuit of single-substrate parallel components; this inherently improves ratiometric matching beyond the level practical by the use of precision components alone.) The op-amps include capacitors in the feedback loops to reduce the 10kHz (and multiples) carrier frequency components to manageable levels.

II.2.3.3 Normalization

The components A+B, B+C, C+D, and D+A required for proper system operation are relatively easily generated. Referring back to the system introduction in Section II.2.3, we also see that the requirements include a division by (A+B+C+D). Division, particularly division accurate to 1 part in 65536, is difficult, if not impossible, to achieve in the analog domain. This circuit instead works on the realization that it is merely necessary to scale A, B, C, and D together such that the sum A+B+C+D is equal to some constant value.

Consider only the vertical circuit consisting of U5 and U6. U5 is a dual (intrinsically matched) multiplier that provides an output signal of K'*(A+B) for section 1 and K'*(C+D) for section 2. Section 3 of op-amp U6 sums the two product outputs to K'*(A+B)+K'*(C+D), or K'*(A+B+C+D). The output of this summation is presented to integrator section 4 of the opamp. The output voltage of this integrator changes, depending on the value of the summation. The output voltage, times the intrinsic multiplication factor of the multiplier U5, defines the value of K'. The integrator changes so as to force K'*(A+B+C+D) to equal the exact value required for the system. This approach, rather than requiring 1 part in 65536 accuracy for an analog division, (not a feasible proposition) instead requires only that the intrinsic accuracy of the division multiplied by the mismatching of the two sections of the monolithic multiplier be 1 part in 65536, in essence reducing the requirements for each to the square root of 65536, or 1 part in 256. Even this requirement is reduced by the initial calibration of the system, to require that the drift, between calibrations, be - for each error component - 1 part in 256. This is well within the capabilities of current

technology, and within the capabilities of the components selected.

II.2.3.4 Synchronous Track and Hold

The A:D converters used by the host computer require that the signal applied be constant during the conversion cycle. This requires that a track and hold circuit be used to "freeze" the analog voltage level. The track and hold "Tracks" the input signal when its control voltage is a logical 1, and "Holds" the acquired voltage when the control voltage is a logical 0.

A second requirement exists for the system. The host A:D makes its conversions asynchronously with the 10kHz carrier. This means that any residual carrier in the output signal will be "aliased" into the measurement as a spectral component, and if the host A:D conversions are not at a constant frequency, the spectrum will be broad-band, indistinguishable from noise. This potential problem is eliminated by allowing the sample and hold to "grab" the signal only at a fixed phase compared to the input 10kHz signal. U13 uses the SYNC signal to create a phase-constant "Track" pulse, relative to the 10kHz carrier. The host converter has the further capability of eliminating even this track-and-hold update, allowing synchronization of the entire system.

II.2.3.5 Miscellaneous Considerations

The A:D converter in the host has a differential input capability. This intrinsically cancels any noise which might occur on the analog signal path. The board creates this signal by sending the output of the track and hold amplifiers along one wire to the A:D converter input, and by inverting that signal (amplifier U12) and sending that inverted signal to the inverting A:D converter input.

In addition to the output to the A:D converter, the Synchronous Detection board provides mirror positioning servo feedback, and a calibration measure of overall detector light level. The first is provided by independently buffering the detected and normalized signals (also sent to the track and hold circuit) and placing those buffered (U12) signals on the backplane on lines switch selected by SW1. (This allows the same generic board to serve as for Detector A, B, or C). An opamp, U12, sums the A+B+C+D signals, before multiplier normalization, and similarly places them on the backplane (SW1, SW2 selected) for overall light level calibration.

Synchronous Detection "A" and "B" circuits are for detection of the differential position information of Detectors A and B. This detection (and the manipulation of the information gained) is the

primary task of the system. Syncdet "C" has a much more limited task. Its task is to provide servo information only to the mirror positioning servo, generally only during calibration and initial lock acquisition. Synchronous Detection board "C" provides no output to the host computer A:D converter, and thus requires no (costly) track and hold circuits. The "C" board is identical to the "A" and "B" boards except for switch settings, and the elimination of the track and hold amplifiers.

II.2.4 Detection Subsystem Performance

As discussed in Section I.3.1, we considered it unwise to build such an ambitious instrument without having first characterized the most important subsystems separately. This was for two reasons. First, the subsystems were extremely advanced, and it would be better to find the necessary changes early on. Second, it would be extremely difficult to characterize the subsystems once the entire system was assembled.

In the case of the detection subsystem, we concentrated our efforts on characterizing the Noise Equivalent Displacement of a laser spot on a detector. We built a fairly elaborate and flexible setup with which we could send a laser beam (after modulation by the AOM) to a detector mounted on a two-axis micropositioner. (The micropositioner was our own Melles Griot Nanomover system, which we eventually decided was so good that one like it should be used as the detector positioner in the breadboard instrument).

The laser beam's size was continuously adjustable from a small fraction of a millimeter to many millimeters. We achieved the adjustability with a series of reversible beam expanders and a photographic zoom lens. We found, however, that multiple reflections inside these multiple lenses gave very dim ghost images whose positions fluctuated with the jitter of the lenses. The position fluctuations for the ghost images were larger than for the main laser spot, which gave an unrealistically high NED. We therefore abandoned this approach in favor of a simple two lens system that gave a spot diameter on the order of 5 mm. This was somewhat larger than we planned to use on the breadboard instrument, but it was a good choice in that it showed the contribution to NED of the electronics alone, which was what we wanted.

This part of the project was difficult, time consuming, and very important, since it was responsible for improving the electronics where necessary, and for developing adjustment guidelines for the electronics. The results, however, are quite easily stated. We achieved a NED for single measurements taken at a rate of 100 kHz of approximately 1 part in 20,000 of the spot diameter. For boxcar averaging at a rate no faster than 2 kHz, this translates

into an NED of approximately 1 part in 150,000 of the spot diameter. Assuming a spot diameter on the detector of 2 mm, this would give an NED of 13 nm, which was easily good enough to meet our NED error budget of 97 nm. This gave us confidence that the instrument could work beyond its original goals, which was confirmed.

Part of our initial plan for characterizing the detection subsystem was to characterize the detector itself by shining a laser spot on it, and then moving the detector's translation stage so that the spot would be effectively scanned over the entire active area. This was to give us a clear picture of the detector nonuniformity, so that we could define the quality of a given detector. Using a larger spot would allow us to build up a lookup table of spot position versus signal, so that the final instrument would have the greatest accuracy possible.

We embarked on this approach, and developed the algorithms for characterizing detector response in terms of power series functions. We found that all our detectors were comparably good, and that no screening was necessary. Moreover, we confirmed from our polynomial algorithm work that the characterization of a detector depended not only on the detector, but also on the precise nature of the laser beam. We also found that the laser beam changed slightly with time. Of course, measuring a test piece with any considerable curvature would also change the beam profile on the detector. For all of these reasons, we determined that this characterization belonged in the breadboard instrument, and should be performed regularly. As discussed in Section II.4.2, this is what we did, with very good success.

The final planned characterization was for frequency response. We quickly found, however, that (1) there was no inherent loss of response much below 10 kHz; and (2) there would be no need to scan the breadboard instrument at such speeds as to require sampling at frequencies greater than 500 Hz to 1kHz. We therefore inserted simple RC filters on the analog inputs to the computer so that the response was naturally attenuated for high frequencies, with a rolloff occurring at approximately 1 to 2 kHz.

II.3 Dual Range Servo Subsystem

The second critical subsystem is the dual range servo (voice coil driven) to actuate the steering mirror in the directions both along and across the scan. (As discussed in Section II.1.2, the dual range servo subsystem replaced the separate large range and small range servos originally envisioned.) The corresponding electronics board is the Servo Amplifier board. (Of course, the boards discussed in Section II.2 are part of this subsystem as well, in that they give the error signals used as inputs to the

servo.) We discuss the Servo Amplifier board below, and then discuss the mechanics of the servo subsystem, and the subsystem's overall performance.

II.3.1 Servo Amplifier Board

Figure II.9 gives the schematic for the Servo Amplifier board. The board consists of two identical channels (horizontal and vertical), only one of which will be discussed. The operational sections are as follows:

(1) Input Gain Set R30;
(2) Clipping amplifier, U3 Section 2 (Pins 5,6,7);
(3) Response Shaping Amplifier, U3 Section 3 (Pins 8,9,10);
(4) Clipping Level Set R38;
(5) Power amplifier Driver U1 Section 4 (Pins 12,13,14); and
(6) Output drive transistors, Q1, Q2.

The amplifier accepts a signal proportional to position error from the Oscillator / Feedback Selector board, and uses that signal to drive the moving-coil actuators on the steering mirror assembly towards a zero-error condition.

It is important that the constraints of the steering mirror assembly be understood if the servo amplifier operation is to be understood. The steering mirror assembly has a certain amount of mass, and has spring components which define a certain amount of stiffness. The combination of mass and stiffness define a resonant system, one where the resonance is controlled by the damping of the system. In the steering mirror assembly used there are two sources of damping at the fundamental resonance (which is just below 10Hz). The most obvious, but relatively insignificant component, is the mechanical viscosity of the system, the friction internal to the metal spring components, and the friction of the mirror pivot assembly. The more significant component is the damping generated by "short circuiting" the motor coils. As a coil moves in a magnetic field, current and voltage are generated; if the coil is short-circuited, that energy is dissipated as heat creating the damping. The servo amplifier has an output impedance of very nearly 0 ohms, and thus acts as just such a short circuit across the coil, and thus the raw electromechanical behavior of the mirror assembly is that of a fairly well damped mass/compliance system.

A mass compliance system will have, for a constant applied force, constant displacement at low frequencies, and will change to constant acceleration at high frequencies. (At the resonance frequency it may be characterized as "constant velocity.") For a position servo, the optimum (fastest, yet non-oscillatory) behavior results when the amplifier creates a system response velocity proportional to the position error. If the natural

mirror behavior were graphed for velocity as a function of frequency for constant voltage drive, the resulting graph would fall off at 6dB/octave on either side of the resonance frequency of about 10Hz. The amplifier frequency response is designed to have a voltage in to voltage out response characteristic which is the opposite of the mirror response. When the two are connected together, the resulting frequency (and phase) response is, up to a little over 100Hz, very similar to the desired "constant velocity" behavior. (There is some acceptable "peaking" residual at 10Hz.)

While the foregoing discussion takes care of the small signal part of the system, a set of large signal criteria must be met as well. The mirror assembly is fairly fragile; excessive forces, once the mirror has hit a physical limit, can cause damage. This means that the maximum displacement must be limited; this is a low-frequency limit. The maximum accelerations must likewise be limited. Excessive accelerations can place excessive force loads on the mechanical flexures in the driving linkage, and can have the subtle (but catastrophic, for a precision angular measurement system) effect of deforming the mirror. To avoid both those effects (particularly the latter), the accelerations must be limited. The limiting occurs by taking advantage of the finite output capability of the op-amps in the circuit. They inherently cannot have an output beyond the power supply rails. By placing a potentiometer at the output of the last op-amp section before the power amplifier, it is possible to limit both the peak velocity and the peak acceleration of the system, without having a significant effect on the peak velocity in the range of 2Hz to 30Hz.

The exact behavior was chosen on the basis of two frequency-dependent graphs, the first being the graph of maximum allowable displacement (mirror physical limits) and maximum allowable acceleration (1G - about a factor of 4 below any significant mirror deformation for the given mirror geometry), the second graph being the required displacement as a function of frequency to track both mirror curvature and local curvature defects. The available behavior fit in the region between those two curves.

We refer now to Figure II.9 for a detailed discussion of the circuit. U3 section 2 (pins 5,6,7) has a voltage divider on the output, limiting the output voltage to about +/- 1.5v, and has from that point to the inverting input a 10:1 voltage divider, resulting in a gain of 11. This provides sufficient system gain to require some attenuation in R30, the primary servo gain potentiometer. U3 section 3 (Pins 8,9,10) has the response shaping for the system. The input network provides the required high frequency boosting, while the feedback network provides the low frequency boost. (The 10M resistor limits the gain at very low frequencies, and is normally removed from the system once

initial setup is complete.) The gain at 10Hz is about 1 for the system, but is much higher at very low and very high frequencies. Potentiometer R38 takes advantage of the intrinsic clipping behavior of this amplifier; the amplifier is incapable of clipping at 10Hz, but can clip at very low and very high frequencies (where, as described above, the drive must be limited to avoid damage or bad measurements.) The adjustment of R38 provides the necessary limiting.

Section 4 of U1 is the voltage amplifier part of the power amplifier. It has its own capacitive feedback, effective at very high frequencies, but the greatest part of the feedback around U1 is by means of a 10K resistor from the output of the class B emitter follower transistors (Q1, Q2) to the inverting input. U1 acts as a unity gain follower amplifier.

The output stage consists of a PNP and an NPN Darlington transistor pair. Both are connected as emitter followers. The NPN "sources" current to the mirror motor, and the PNP "sinks" current from the mirror motor. In the region around zero, both transistors are maintained slightly "on" by a series-connected array of 1N914 diodes. The "crossover distortion reduction" current is limited by local negative feedback at the transistors, a 2ohm resistor in series with the emitter of each transistor.

To adjust the servo, R38 (R39) is first adjusted using a very low-frequency square wave input of about 2v to narrowly avoid hitting the mechanical stops of the mirror. The response characteristics of the system are such that this single adjustment is appropriate also for the high-frequency acceleration limit.

With the drive safely limited, the servo amplifier can be connected into the system. R30 should be initially at minimum, and the system should be configured for the "C" detector (steering mirror LED generated) position feedback. The computer should then generate a fairly small 2Hz square wave "bias" signal, and the "C" detector position measurement should be observed. Adjust R30 for an oscilloscope display showing a representative square wave with about 20-30% overshoot on the leading edge. Repeat the test using the "A" detector instead. (This requires a test piece, and acquisition of signal on the "A" detector.) If the overshoot with detector "A" is greater than 20-30%, readjust R30. Otherwise leave it alone.

With R30 and R31 adjusted, connect the oscilloscope for an X-Y display, and have the computer generate an identical "bias" 2Hz square wave for both vertical and horizontal axes. Connect the oscilloscope X input to the Synchronous Detection A horizontal output, and the Y input to the Synchronous Detection A vertical output. Adjust R31 for the narrowest possible diagonal line on

the oscilloscope. This completes the servo adjustment.

II.3.2 Mechanical Design

The mechanical design of the servo subsystem was the most complex phase of the project, and the results were some of the most technically impressive. The subsystem consists of a single steering mirror in a two axis gimbal assembly, driven by two voice coil actuators. The rotation axes of the steering mirror meet at the mirror's center on its reflecting surface. The usable range for steering the outgoing beam is +/- 30 degrees in any direction. Every moving element is completely flexure supported, so that there are no moving parts, and absolutely no friction. Below we discuss each component, starting with the mirror and ending with the actuators.

The steering mirror is an ultra-smooth (but commercially available) Zerodur flat with a 15 mm diameter. It is mounted inside a Super Invar cup with three tiny tangential blade flexures. Figure II.10 shows this inner cup with the mirror inside it. The inner cup is rotatable inside an outer stainless steel cup. The attachment is through a pair of commercially available Lucas Flex Pivots, which are cylindrically shaped flexures where one end is rotatable with respect to the other end over a +/- 30 degree range. The outer cup is rotatable inside a fixed cup. The attachment is again through a pair of Flex Pivots, this time oriented at 90 degrees with respect to the first rotation axis. The axes of all the Flex Pivots meet at the center of the steering mirror's reflective surface. Figure II.11 shows the mirror, inner cup, outer cup, and fixed cup.

The assembly of cups is mounted as a unit at the end of the measurement arm. Voice coil actuators at the instrument end of the measurement arm are attached to the inner and outer cup through aluminum actuator arms. The actuator arms are attached both to the mirror cups and to the voice coils with tiny blade flexures to provide the necessary degrees of freedom.

Figure II.12 shows a side view of a voice coil actuator. The permanent magnet part is stationary, and the coil moves axially inside the magnet. The coil is restrained with a single blade flexure that determines the axial twist and the two lateral displacements. The other degrees of freedom are constrained by the combination of the mirror cups and the actuator arm, leaving the axial motion as the only unconstrained motion. (It is precisely this motion, of course, that is controlled by the voice coil actuators.)

Finally, Figure II.13 is a conglomerate cutaway view of the measurement arm, showing all of the components discussed above.

II.3.3 Servo Subsystem Performance

To characterize the limiting accuracy, frequency response, linearity, and range of the servo subsystem, we had originally proposed two separate methods. In the first method, we would sinusoidally drive the mirror, and have the servo subsystem attempt to keep the laser spot centered on the detector. The servo subsystem's characteristics would then be defined by measuring the compensated spot position as a function of time. In the second method, we would add a sinusoidal bias to the detector signal which serves as input to the servo subsystem. In this method, the servo subsystem would think that the spot position was moving, and would therefore attempt to compensate for it. We would then define the servo subsystem's characteristics by measuring the sum of the true spot position and the sinusoidal bias as a function of time.

We determined during the project that this characterization was exactly equivalent to the more standard procedure of characterizing the servo's phase shift and gain as a function of frequency. We performed that test, and discussed the results in detail in Section II.3.1. To resummarize briefly, the gain of the servo subsystem is the product of the amplifier gain and the physical mirror/actuator gain. The amplifier gain has a minimum at 10 Hz, and rises at 20 dB per decade both below and above 10 Hz. The physical mirror/actuator gain is fairly flat below 10 Hz, has a peak at the resonance point of 10 Hz, and falls at 40 dB per decade above 10 Hz. The product, then, is a rather straight response falling at 20 dB per decade for all frequencies, but with a mild peaking at 10 Hz. The overall level of the gain curve is adjustable with a potentiometer to give the highest possible gain without introducing oscillatory behavior.

Although we de-emphasized the driving of the steering mirror with an added sinusoidal voltage, the insight gained from the analysis of the approach was extremely valuable. It led to our automatic alignment approach, whereby the steering mirror is servoed to Detector C, and the computer adds voltages to the Detector C voltages to steer the mirror to any desired angle. The mirror can thus be steered in a spiral pattern until the beams reflected by the test piece find their way onto Detectors A and B.

The performance of the servo system can also be conveniently summarized in a very different way. It is less rigorous and informative, but is useful nonetheless. We can simply describe the Root Mean Square (rms) residual jitter during typical instrument conditions. We have found that, with the instrument stationary and servoing on Detector C, the rms steering mirror jitter is approximately 5 arc seconds. Servoing on the more sensitive Detectors A and B, the jitter is almost undiscernible with the instrument stationary, and increases to approximately

0.5 arc second rms during a typical scan. This is easily good enough to keep the laser spots on the calibrated areas near the detector centers during a scan.

II.4 Breadboard Instrument Design and Fabrication

In this section we describe the finished breadboard instrument. We do not give great detail on the development process itself, although the development was of course the main body of the work. Rather, we describe the breadboard instrument in some detail, and comment on the development process wherever it contributes to the understanding of the need for a particular component or approach.

II.4.1 Optical and Mechanical Design

We implemented the breadboard instrument using a modular approach. The measurement arm discussed in Section II.3 was used without modification, and was simply attached to one end of a large baseplate. We used a sturdy aluminum box to enclose Detectors A and B and Detector B's micropositioners. We attached the box to the baseplate with wire flexures, and mounted all the other optical components directly to the baseplate. We scanned (translated) the instrument by attaching the baseplate to a large motorized stage.

Figure II.14 shows the optical baseplate from above, and shows the locations of the major components. (Figure II.14 can be easily compared to Figure I.4, which showed a much more conceptual but very similar instrument layout.) The optical path can be traced through the various components to the test piece as follows (neglecting simple flat mirrors):

(1) laser;
(2) Acousto Optic Modulator (AOM);
(3) half waveplate (followed by optional polarizer);
(4) lens 1;
(5) pinhole;
(6) lens 2;
(7) nonpolarizing beamsplitter;
(8) measurement arm (with calcite plate inserted);
(9) steering mirror; and
(10) test piece.

After the two measurement beams are reflected from the test piece, they proceed back to the detector box as follows (again neglecting simple flat mirrors):

(1) steering mirror;
(2) measurement arm (with calcite plate inserted); and
(3) nonpolarizing beamsplitter;

The lens that focuses the beams onto the detectors forms the porthole into the detector box. Thus, the optical path length from the porthole to each of the detectors inside the box is equal to the focal length of the lens, which is 1000 mm. Figure II.15 is a top view of the inside of the detector box, showing the folding of the long optical path before the beams encounter the polarizing beam splitter, which sends one beam straight to the fixed detector (Detector A), and the second beam downward to the movable detector (Detector B).

There are several notable features of the mechanical and optical implementation which are summarized individually below.

II.4.1.1 Flexure Supports

As previously mentioned, we used flexure supports to attach the detector box to the optical baseplate. We used a series of three bipods, each of which was made up of two wire flexures. Figure II.16 is a side view of a flexure bipod. We simply bolted one of the aluminum blocks to the baseplate, and the other to the detector box. The individual wire flexures were made by drilling axial holes through two setscrews, and then silver soldering a stainless steel wire through the two setscrews. Each of two finished wire/setscrew assemblies was then screwed into tapped holes through the two aluminum blocks.

It can be shown that, for a wide range of orientations, the set of three bipod flexures provides an entirely kinematic support. A kinematic support is one which fully constrains the rigid body motions (three translations and three rotations), but imposes no internal non-rigid body stresses. Two properties of a kinematic support such as this are that (1) the support system would collapse upon the failure of any single flexure element; and (2) non-rigid body deformations either of the flexures or of the piece being supported (e.g., thermal growth) do not impose internal non-rigid body stresses.

Because of the advantages discussed above, we emphasized the use of kinematic flexure supports. As discussed in Section II.5.3, we in fact found that the instrument incurred a very large systematic measurement error when we failed to use a flexure support of the instrument from the moving stage. Our work at the end of the project showed, however, that well designed fixed mechanical supports could give the same performance as the flexure supports in terms of eliminating systematic measurement errors. In addition, the fixed mechanical supports are much simpler, and are not susceptible to rapid thermal changes as are the wire flexures. We therefore have settled on fixed mechanical supports for commercial versions of the instrument.

II.4.1.2 Beam Conditioning Optics

The beam conditioning optics consist of a first lens to focus the laser beam, a pinhole to 'clean up' the focused spot (i.e., to eliminate the random intensity fluctuations outside, say, two 1/e^2 diameters), and a second lens to reconverge the beam and put its waist onto the test piece. (The waist of a laser beam is its narrowest point. The beam is collimated at the waist, and gradually diverges and expands in both directions.) By using two lenses, we have the flexibility to put a waist of any desired size at any desired location. The parameters to be varied are the two lenses' focal lengths and the spacing between them.

We found that we could get an effectively unlimited range of spot size on the test piece by using commercially available lenses and reasonable spacings. Table II.1 shows eight examples using various focal lengths and spacings, with resulting spot radii from 33 microns to 133 microns.

The most important knowledge gained in this area concerned the pinhole. We found that the pinhole did effectively clean up the beam and thereby put a cleaner focused spot on the detectors. However, we found that minute alignment drifts in the system caused the beam to change its location slightly within the pinhole. This resulted in corresponding slight changes in the intensity profiles of the focused spots on the detectors. Since system calibration implicitly assumes an unchanging spot profile on the detectors, these otherwise innocuous alignment drifts had the bad effect of degrading the calibration and therefore the measurements. We found that when we removed the pinhole, this component of drift went away. We concluded, therefore, that we should delete the pinhole and accept the less clean spots.

II.4.1.3 Calcite Windows

The calcite windows are simple plane parallel plates of calcite, with anti-reflection coatings on both sides. Because the increase in cost was negligible, we had a series of plates fabricated by Karl Lambrecht with slightly different thicknesses. This gave us the option of using coaligned plates in series to give the effect of a single window with a thickness equal to the sum of the individual thicknesses. It also gave us the option of using a pair of oppositely aligned plates to give the effect of a single window with a thickness equal to the <u>difference</u> of the individual thicknesses. We thus had effective thicknesses available over a range from approximately 0.1 mm to 4.0 mm. In practice, we found that two thicknesses (1 mm and 2 mm) were sufficient to cover the full range of measurement conditions and objectives.

To facilitate the removal or exchanging of the calcite windows,

we installed them in standard lens holders which we could quickly mount on our optical bench.

II.4.1.4 Detector Micropositioners

The detector micropositioners are used to center Detector B on its focused laser spot. As previously discussed, this allows for compensation for a very wide range of concave and convex base radii of curvature on the test piece.

With the steering mirror servoed to keep the spot focused on Detector A, the micropositioners are also used for an important calibration step, where Detector B is moved in a raster pattern around its laser spot to characterize output signal as a function of spot position.

This calibration step imposes particularly tight requirements on the accuracy of the micropositioners, since it is this step that lets us infer a particular curvature value from a given set of output signals. To get the required accuracy, we used the Melles Griot Nanomover system originally used in the breadboard demonstration phase. This system has 0.05 micron resolution, 0.10 micron repeatability, and 1.0 micron absolute accuracy (calibratable to 0.10 micron).

The positioning system consists of the Nanomover motorized micrometers, and a stacked pair of standard Melles Griot 160 mm steel translation stages. As discussed in Section II,6, we made an important observation late in the project that the stacking of two stages allows angular errors (particularly in the bottom stage) to manifest themselves as positional errors at the detector. Naturally, in-plane straightness errors are always a problem in a two-axis system. Unfortunately, the angular tolerances on these stages are a factor of 20 looser than on, for example, high quality air bearing stages. In short, although the Nanomover system is well suited to a single axis, the imperfections in the stages limit performance when a large calibration range is required. (This is the case when testing exotic aspheres.)

II.4.1.5 Instrument Scanner

One of the single most important features of our measurement approach is that it is insensitive to all rigid body disturbances of the test piece. That is, if the test piece vibrates or drifts in position, our measurements are unaffected, since we measure curvature rather than height or slope, and since curvature is invariant with respect to rigid body motions. It is clear, then, that small errors in the instrument's scanning trajectory <u>also</u> have no effect on our measurements. This is extremely important, since it allows us to use an easily obtained and reasonably

priced translation stage instead of a one-of-a-kind, ultra-precise, extremely expensive stage.

For the breadboard instrument, we selected a precision grade Daedal stage with a 10 by 10 inch mounting surface and an 8 inch travel range. The straightness is quoted by the manufacturer at 8 microns peak to valley (80,000 Angstroms) per 100 mm of linear travel. As discussed in Section II.5.2, our measurement accuracy over a 100 mm scan is on the order 6 Angstroms rms, or something on the order of 30 Angstroms peak to valley. In other words, our measurement accuracy for a 100 mm scan is on the order of 3000 times better than that of the scan trajectory. This demonstrates quite graphically our immunity to rigid body motions. In fact, it demonstrates the great advantage of the measurement approach, since there is probably no translation stage in the world that could do a 100 mm scan with a 30 Angstrom peak to valley straightness.

II.4.2 Algorithms and Software

Software development was a very large and important phase of the project. Software was written from the lowest levels (controller routines for the various hardware components) to the highest levels (executive programs for running the instrument and displaying the measured data). At the middle level, we designed and implemented several sophisticated algorithms, especially in the area of calibration. The calibration algorithms in particular are responsible for much of the instrument's accuracy. In this section, we first discuss the calibration and other algorithms, and then summarize the major software modules. See Section III for a detailed list of the software routines and modules.

II.4.2.1 Calibration Algorithms

Our approach to calibration is a powerful two step procedure that gives extremely high accuracy without requiring any calibrated hardware other than the Detector B positioners. One can imagine that two steps are required, since there are two detectors. More importantly, only one of the detectors is movable. Finally, the sensitivity of the detectors is finer than the resolution of the detector positioners. All of this makes an innovative calibration procedure very desirable.

The first step of our calibration procedure is the more important step. It involves characterizing the <u>difference</u> in response between the two detectors. Put another way, it allows us to differentiate between <u>common mode</u> spot motions on the detectors (caused by vibrations and steering mirror jitter), and <u>differential</u> motions (caused by true test piece curvature changes that are the quantity we are interested in). We perform the

calibration by moving the steering mirror over a small raster pattern so that the spots are moved on the A and B detectors over a small region near the centers. (Typically, the region is a square resulting in detector signals of ±20% of full scale reading.) We then use standard least squares techniques to express the B detector response in terms of the A detector response. If u and v are the signals (scaled from -1 to +1) corresponding to motions in the x and y directions, we can express the least squares fit results as follows:

$$u_B = \sum_{i=0}^{N} \sum_{j=0}^{N-i} CABU_{ij}\, u_A^{\,i}\, v_A^{\,j} + \text{Residual} \qquad (1)$$

and

$$v_B = \sum_{i=0}^{N} \sum_{j=0}^{N-i} CABV_{ij}\, u_A^{\,i}\, v_A^{\,j} + \text{Residual} \qquad (2)$$

where N is the order of the fit, $\{CABU_{ij}\}$ and $\{CABV_{ij}\}$ are the fitted coefficients, Residual is the unfitted residual, and (u_A,v_A) and (u_B,v_B) are the signals from the A and B detectors. As an example, note that if the detector responses were identical, then (u_B,v_B) would equal (u_A,v_A), and we would have

$$CABU_{10} = CABV_{01} = 1 \qquad (3)$$

with all other $\{CABU_{ij}\}$ and $\{CABV_{ij}\}$ being zero. Any departure from this set of coefficients represents the inequality in the detector responses.

This first step in calibration is the most important, since it is this step that allows us to eliminate common mode spot motions. We simply map a measured (u_A,v_A) to a corresponding (u_B,v_B) through Equations 1 and 2. Then, any <u>deviation</u> of the measured (u_B,v_B) from the corresponding signals mapped from (u_A,v_A) represents a true change in test piece curvature. Of course, the beauty of this approach is that no mechanical precision is required. The raster pattern of the steering mirror can be quite erratic. All this is needed is to collect many data points within the desired range of signals. The least squares fit then provides the mapping, with accuracies typical of the <u>detector resolution</u>. (Recall that typical detector resolutions are on the order of 0.01 micron, which would be extremely difficult if not impossible to achieve with any mechanical accuracy.)

The first calibration step, then, gives us tremendous accuracy in rejecting common mode spot displacements. In short, for a set of real test piece measurements, it gives us a corresponding set of Detector B signal variations that are more or less proportional to the changes in test piece curvature.

The second calibration step is to map the Detector B signal variations to physical spot displacements. We call this step the B-B calibration, since it tells us the signal-to-displacement mapping for the B detector. The requirements here are much less demanding, since they basically affect the shape of the instrument's measurement response, rather than the (much more important) common mode rejection. Put another way, if the second calibration step is not performed accurately, then a 5 Angstrom test piece bump might be measured as 4.5 Angstroms, and a 7 Angstrom bump might be measured as 7.2 Angstroms, but a perfect test piece would be measured as perfect.

The approach to this second calibration step is straightforward. Detector B is moved by its positioners in a known raster pattern, and the signals (u_B, v_B) are measured. The positions (x_B, y_B) are fit using least squares techniques to (u_B, v_B) as follows:

$$x_B = \sum_{i=0}^{N} \sum_{j=0}^{N-i} CBBX_{ij}\, u_B^{\,i}\, v_B^{\,j} + \text{Residual} \qquad (4)$$

and

$$y_B = \sum_{i=0}^{N} \sum_{j=0}^{N-i} CBBY_{ij}\, u_B^{\,i}\, v_B^{\,j} + \text{Residual} \qquad (5)$$

where, again, N is the order of the fit, $\{CBBX_{ij}\}$ and $\{CBBY_{ij}\}$ are the fitted coefficients, and Residual is the unfitted residual. In reality, we did not perform exactly the fit defined in Equations 4 and 5. Rather than fit the positions to a polynomial series in the raw signals, we fit them to that series <u>added</u> to the analytical form that would hold if the detector were perfect and if the spot were perfectly Gaussian, allowing for ellipticities and axis skewing. This reduced the accuracy and dynamic range requirements on the least squares fit. The basic form for a perfectly Gaussian spot was found simply by moving the detector in a very small range over four points near the center, and four spots at the edge. Without going into the derivation details of this nominal Gaussian response, we simply state that the perfect positional response (x,y) of the detectors in such a case is given by

$$x = (w_{det:x} / 2^{1/2})\, \text{erf}^{-1} \left((u/u_{full}) \cos\theta_u + (v/v_{full}) \sin\theta_u \right) \qquad (6)$$

and

$$y = (w_{det:y} / 2^{1/2})\, \text{erf}^{-1} \left(-(u/u_{full}) \sin\theta_v + (v/v_{full}) \cos\theta_v \right) \qquad (7)$$

where $w_{det:x}$ and $w_{det:y}$ are the 1/e^2 radii of the spot on the detector in the x and y directions; erf^{-1} is the inverse error function; u_{full} and v_{full} are the full scale readings of the detectors in the u and v directions; and θ_u and θ_v are the

angular misalignments of the detector's u and v axes. (Again, $w_{det:x}$ and $w_{det:y}$, u_{full} and v_{full}, and θ_u and θ_v are found in terms of the readings at four points very near the center and four spots near the edge.)

Now, of course, the accuracy of this fit depends completely on the mechanical accuracy of the positioners. Our Melles Griot Nanomover system has resolutions of 0.05 micron and single axis accuracies of 0.1 to 1.0 micron. However, errors resulting from angular deviations on the first axis turning into positional errors on the second axis appear to limit accuracy to the 1.0 micron regime. As discussed in Section II.5.2, this was good enough to beat our performance goals by an order of magnitude. However, as discussed in Section II.6, we will want to use an improved positioner system to allow us to test large, exotic aspheres.

To summarize the calibration procedure, then, we calibrate in two steps. First, we determine the Detector B signals that would correspond to measured Detector A signals for a perfect test piece. We then determine the relationship between measured Detector B signals and physical spot motions. When we perform a measurement and collect measured data for (u_A,v_A) and (u_B,v_B), we first map the (u_A,v_A) values to corresponding (u_B,v_B) values using the first ("A-B") calibration step. The difference between these mapped (u_B,v_B) values and the actually measured (u_B,v_B) values indicates true changes in test piece curvature. To calculate the actual differential spot motions, we map these differential (u_B,v_B) values to physical spot motions using the second ("B-B") calibration step. What we have, then, is a set of data for the differential spot motions as a function of measurement location on the test piece. We briefly summarize in Section II.4.2.2 how this information is turned into a profile of test piece surface height.

II.4.2.2 Other Algorithms

The calibration algorithms discussed above are the most critical in terms of getting the highest performance from the instrument. The other algorithms are straightforward, and are discussed in this section. They include (1) the conversion from differential spot displacements to test piece curvature; (2) the conversion from test piece curvature to surface height for near-flat test pieces; (3) extensions to non-flat test pieces; and (4) data windowing for the calculation of Power Spectral Densities (PSD's).

The first algorithm defines the conversion from differential spot displacements to test piece curvature. This involves only a simple scale factor. We note first that curvature (at least for near-flat test pieces) is equal to the second derivative of

surface height, or the first derivative of surface slope. Thus, the test piece curvature is equal to the difference in surface slopes, divided by the spot separation d. The difference in surface slopes, in turn, is equal to one half the corresponding difference in reflected ray slopes. And, finally, the difference in reflected ray slopes is equal to the difference in spot displacements, divided by the focusing lens focal length f. In short,

$$\Delta\text{-disp} = (\text{test piece curvature})\ (2\ d\ f) \qquad (8)$$

or $$(\text{test piece curvature}) = \Delta\text{-disp} / (2\ d\ f) \qquad (9)$$

where Δ-disp is the differential spot displacement on the detectors, d is the spot separation on the test piece, and f is the focusing lens focal length.

The next algorithm defines the conversion from test piece curvature to surface height for near-flat test pieces. In this limit, since the curvature is equal to the second derivative of the surface height, the height is simply the second integral of the curvature. The two resulting constants of integration correspond to the rigid body piston and tilt, and are thus unimportant. We analyzed two options for performing the double integration. The first involved Fourier transforming the data, dividing by the square of the spatial frequency, and inverse Fourier transforming. This approach had some promise for giving the best response characteristics at high spatial frequencies, but it was plagued by edge effects. The second approach involved approximating each of the two integrals as a simple numerical running sum of the data, multiplied by the sample length. This gave slightly attenuated response at the highest spatial frequencies, but was extremely fast, and completely free of edge effects. Since our sampling intervals are always much smaller than the natural limiting horizontal resolution of the instrument, we found that the additional attenuation at the highest frequencies was not at all detrimental, and in fact was a help. Therefore, the simple numerical integration approach was selected. To avoid shifting the data by a single pixel's length, we summed first in the forward direction, and then in the backward direction. This gave complete symmetry, not only avoiding the shifting, but also assuring zero phase shift (because of the symmetry) for all spatial frequencies.

The next algorithm defines the extension of the double integration approach to non-flat test pieces. As the test piece deviates significantly from flatness, the curvature deviates significantly from the second derivative. In general, it can be shown that the curvature C and the second derivative z" are related as follows:

$$C = z'' / (1 + (z')^2)^{3/2} \quad (10)$$

where z' is the first derivative, or surface slope. For small values of slope, Equation 10 can be approximated as

$$C \approx z'' (1 - (3/2) (z')^2) \quad (11)$$

The approximation thus grows worse quadratically with the non-flatness of the test piece. When the non-flatness is significant, we defined an algorithm where the surface height at each successive measurement point is calculated using simple geometry, given the previous height and slope and the measured curvature. In this method, height and slope are derived simultaneously. Since all of our important test work was with near-flat test pieces, and since the near-flat algorithm can still be used to determine repeatability for non-flat test pieces, we used the near-flat algorithm exclusively. The non-flat algorithm was left as a Phase III improvement, discussed in Section II.6.

The final algorithm defines data windowing for the calculation of Power Spectral Densities (PSD's). It is well known that edge effects are troublesome when Fourier transforming data to obtain a PSD. Put another way, the resulting Fourier transform is actually the convolution of (1) the Fourier transform of the true statistics being sampled, and (2) the Fourier transform of the windowing (or sampling) function. (If no windowing is performed, the sampling function is simply a top hat function whose width is the length of the data.) From this argument, it is clear that the function of a window is to provide a function whose Fourier transform is narrow, and falls off rapidly with spatial frequency. The PSD of a top hat function falls off as the square of the spatial frequency. Thus, if no windowing is performed, then no PSD can be accurately characterized if it falls off faster than the square of the spatial frequency. As discussed in Section II.5.2, our surface height noise PSD should fall off as the <u>fourth</u> power of the spatial frequency. Since the noise PSD is one of the most important parameters to characterize, windowing is clearly necessary.

We selected the Hann, or Hanning, window, because its PSD falls off as the <u>sixth</u> power of the spatial frequency, giving us the ability to characterize a wide variety of actual PSD's. The normalized Hann window function, H(x), is the function by which the data is multiplied before Fourier transforming. It is defined by

$$H(x) = (6^{1/2} / 3) (1 - \cos (2 \pi x / L)) \quad (12)$$

where L is the length of the scan. This window is thus a smooth sinusoid with a single cycle, biased to be zero at its endpoints.

II.4.2.3 LINSCAN Module

Having defined the appropriate algorithms, we can now summarize the functioning of the five major software modules. The most comprehensive module is LINSCAN, which we cover in this section. LINSCAN performs a surface measurement with complete data analysis capabilities. The other modules essentially give subsets of the LINSCAN functions, for our own diagnostic use during instrument development. For all of the modules, we summarize the various functions performed and the numerical and graphical outputs. But, because of the R&D nature of this contract, we do not give the level of detail that would be needed for a users' manual. The programs are fairly self explanatory, though, and could be run by an interested NASA user with access to the appropriate computer hardware, given the delivered hardware and software from this project.

After reading in a file ("CONFIG.DAT") containing various numerical parameter values (e.g., focusing lens focal length, motor hardware parameters, etc.), LINSCAN begins by prompting the user for the parameters of the scan. These include scan location and length, pixel size, and scan velocity. It then sends the scanner to the center of the scan, and acquires the test piece. By this we mean that it performs an automatic alignment operation, moving the steering mirror in a spiral pattern until Detectors A and B register the laser spots. It then transfers control of the steering mirror servo to Detector A, so that Detector A is from then on assured of having its spot very near its center. (See Section II.4.2.5 for a further discussion of the initial alignment.)

With the test piece acquired, LINSCAN performs a B-B calibration (see Section II.4.2.1). The user can store the B-B calibration results in a disk file. Also, instead of performing a new B-B calibration, the user may read in the results of a previous B-B calibration from a disk file.

Finally, before performing the actual scans, LINSCAN centers the B detector on its laser spot in order to compensate for whatever base curvature is on the test piece. With the B-B calibration and the centering of Detector B completed, LINSCAN then performs two scans in succession. Before and after each scan, it automatically performs an A-B calibration (see Section II.4.2.1).

Each scan results in a set of data quadruplets (u_A, v_A, u_B, v_B), one for each pixel. Within each pixel, the instrument collects as many samples as possible and averages. The raw data is then operated on to give surface height profiles and other information. The first optional operation is to apply a top hat filter to the raw data, whereby the data is Fourier transformed,

multiplied by a top hat (to remove selected low or high frequency content), and inverse Fourier transformed. In practice, we found that the natural high frequency filtering characteristics of the instrument worked extremely well, eliminating any need for the Fourier filter. The low frequency filter naturally tended to introduce bad edge effects. We therefore used a simple polynomial removal function (discussed below) to remove any low frequency effects. In short, then, we eventually discarded the use of the Fourier filter on the raw data.

After collecting and optionally filtering the raw data, LINSCAN uses the A-B and B-B calibration data (see Section II.4.2.1) to convert the raw data to surface curvature values. (In reality, LINSCAN calculates delta-ray-slope, which is proportional to surface curvature as discussed in Section II.4.2.2.) LINSCAN then integrates the curvature data twice (see Section II.4.2.2) to obtain first surface slope, and then surface height. At each point (raw data, curvature, slope, and height), LINSCAN gives the user the option to view the data. The data may be viewed with a user selectable number of polynomials removed. In addition, the PSD can be viewed, with or without the windowing discussed in Section II.4.2.2.

Figures II.17 through II.20 show sample plots of raw detector data, delta-ray-slope (curvature), surface slope, and surface height. (These plots were taken from one of the several test pieces sent to us for evaluation from potential Phase III customers. Additional plots from these test pieces are discussed further in Section II.5.2). Note that each plot shows the results of both scans together. The user can optionally view the results of either scan individually, or of the difference between the two scans.

Other informative but more diagnostic plots are not discussed here. These include a dual oscilloscope type plot that shows the positions of the two laser spots on the detectors in real time. This is discussed generically in Sections II.4.2.4 through II.4.2.7, and has several different applications.

Finally, LINSCAN offers several options not discussed here. For example, the user can input a previously stored disk file of raw data for further analysis and display. Also, the user can disable the automatic A-B calibration and use a manual calibration instead, where he is required to move a steering mirror by hand. (This option was used during the first phases of the project, before we had implemented the automatic steering mirror.) These and other options were important during the development of the instrument, but were not used at the end of the project.

II.4.2.4 SCOPE Module

The SCOPE module gives the user a real time view of what the detectors are seeing. To this end, it displays two rectangular grids that are to be interpreted just like the display of an oscilloscope. One grid is for Detector A, and the other for Detector B. A cursor moves on each grid, with the instantaneous position in x and y being proportional to the u and v signals from the detector. The user can select any magnification, with unit magnification corresponding to full scale detector readings mapping to the edges of the scope displays. Figure II.21 shows a typical SCOPE display, showing additional numeric displays at the bottom. These numeric displays give the detector signals, and the inferred spot positions in mm. Note also the reference at the side to the coarse and fine cursors. There are two cursors present on each display. The coarse cursor uses the stated magnification, and the fine cursor uses a ten times greater magnification.

SCOPE has several different operational modes. The detectors can be viewed in their raw form, or an A-B calibration can be applied to Detector A, and those results viewed with the actual Detector B results. In addition, for either of these modes, the half-sum and half-difference of Detectors A and B can be viewed. This is particularly useful for monitoring drift. To monitor drift, one looks at the half-sum and half-difference of (1) Detector A mapped to Detector B (with A-B calibration); and (2) the true Detector B. The half-difference is directly indicative of drift. In all cases, the parameters being viewed can be graphed versus time over time intervals from a minute to arbitrarily long.

Another useful operational mode is for SCOPE to cause the scanner to move during any selected display. This allows the monitoring of vibration, and scan-related drifts (instrument warpage, etc.). Finally, SCOPE allows the user to acquire initial alignment on the test piece as in the LINSCAN module (see Section II.4.2.5 for a further discussion of the initial alignment), or to stay in the open loop steering mode.

II.4.2.5 AUTO_FND Module

The AUTO_FND module exercises the automatic alignment feature used in LINSCAN. While the steering mirror is being moved in its spiral pattern, AUTO_FND shows the scope display, but with the left scope showing the steering mirror position and the right scope showing the results on Detector A. As the spiral pattern progresses, the user develops an insight into the response characteristics of Detector A. This was crucial in programming the acceptance criteria for having a spot on Detector A. (Since the detectors give some in-scale reading even if the spots are completely off the detector, it takes some intelligence in the

program to decide when a reading corresponds to a real spot.)

The spiral pattern proceeds in two steps, each with a different criterion for stopping. The first step is a coarse mode, where the pitch of the spiral is chosen as large as possible while still assuring that the detector will be struck at some point. The stopping criterion is that the spot appear to move on Detector A in the direction anticipated based on the current spiral motion, and with the anticipated magnitude. (It is the allowable tolerance on the notion of "anticipated" that determines the success of the algorithm.)

The second step in the spiral is a fine mode, centered on the point where the coarse mode stops. In the fine mode, the pitch of the spiral is chosen to cover some fraction (typically 10%) of the full scale detector reading. The stopping criteria are that (1) the spot appear to move on Detector A in the direction anticipated based on the current spiral motion, and with the anticipated magnitude; and (2) the spot be within a specified distance of the center (that is, zero readings in u and v).

When the fine spiral mode is completed, the spot is assured of being reasonably well centered on Detector A. At this point, the program changes the servo mode to lock on Detector A. It then varies the offset voltages being sent out in order to center the spot precisely. When this is accomplished, the alignment is complete.

II.4.2.6 RUNCENT Module

The RUNCENT module exercises the Detector B centering feature used in LINSCAN. It begins by performing the automatic alignment discussed in Section II.4.2.5. When the spot is suitably centered on Detector A, the program moves Detector B until its readings are as close to zero as possible. (The program assumes that the spot is <u>somewhere</u> on Detector B, so that the readings are meaningful. This is reasonable unless the test piece base curvature is extreme and unknown. We do require that the user have at least an approximate idea of the test piece curvature, so that Detector B can be placed initially in approximately the right place.)

With Detector B centered, the program proceeds to determine the parameters in Equations 6 and 7 by moving the spot to four spots near the center and four spots near the edges of response. Finally, the program displays the parameters in Equations 6 and 7 and exits. These parameters are useful in assessing the health of a spot. For example, if $w_{det:x}$ and $w_{det:y}$ are wildly different, then something is probably obscuring or interfering with the spot.

II.4.2.7 V_OUT Module

The V_OUT module allows the user to lock the steering mirror either in the open loop mode, or on Detector A (after initial automatic alignment). With the steering mirror constantly servoing, the user can use the arrow keys on the computer keyboard to adjust the offset voltages being sent to the steering mirror. In other words, the user can change the steering angles at will. The program shows two scope displays, the left one showing the voltages output, and the right one showing the results on Detector A. When the user is finished with this mode, he is given the option of output a square wave with selectable amplitude and frequency to either or both channels. This option proved very valuable in assessing the servo performance, and in setting the overall electronic gain of the servos.

II.5 Performance Assessment

In this section we review the performance assessment results. We begin with a summary of the most important alignment and adjustment procedures. We then summarize the final results of assessing the excellent accuracy and repeatability. Finally, we comment on some of the sources of drift that become as important as random noise for longer scans.

II.5.1 Alignment and Adjustment Procedures

Alignment and adjustment can be grouped into electronic and optical categories. We previously covered the electronic adjustments in detail in Sections II.1 through II.3. In this section, we cover the optical alignment. Refer to Figure II.14 for a top overall view of the optics.

There are two main stages of alignment. The first is of the beam without any focusing optics, and the second is with the focusing optics (focusing lens, pinhole, and recollimating lens). The first stage is more complicated. In this first stage (no focusing optics), there are four elements to adjust:

Element 1: the first steering mirror (located at the corner of the baseplate immediately after the laser);

Element 2: the second steering mirror (located on the AOM's mounting plate, just before the AOM itself);

Element 3: the AOM (in particular, its two tilt angles); and

Element 4: the third steering mirror (located at the corner of the baseplate immediately before the leg with the focusing optics).

It is helpful to define each one of these adjustable elements as performing a single task, as follows:

Element 1: adjusts the position of the beam on the AOM;

Element 2: adjusts the position of the beam after it exits the third steering mirror and heads down the focusing path;

Element 3: adjusts the Bragg angle on the AOM; and

Element 4: adjusts the direction of the beam as it heads down the focusing path.

These definitions make it fairly simple to iterate through the four elements in succession, adjusting each one to accomplish its specified task. The trickiest part is that Elements 1 and 3 interact to define not only the peak power in the first diffracted order from the AOM, but also to define the quality of the beam. In particular, if Element 3 (the AOM) is badly adjusted, high finesse fringes can appear in the far field beam pattern on the detectors. (We found empirically that a low quality spot on the detector can lead to instrument drifts. Apparently, the lower the spot quality, the more time dependence there is in its shape. It is this time dependence that contributes to measurement drifts.)

With the first alignment stage complete, the second stage involves having the focusing optics inserted. The pinhole focusing lens goes in first, and its lateral position is adjusted to the point where the beam continues along its original direction. The pinhole is then inserted and adjusted laterally for maximum power from the first diffracted order through the pinhole. The pinhole focusing lens is finally adjusted axially to put the focus at the pinhole.

The last step is to insert the recollimating lens, which is adjusted axially to give the smallest spot on the test piece, and laterally to the point where the beam continues along its original direction.

II.5.2 Accuracy and Repeatability

Overall, the accuracy and repeatability of the breadboard instrument are outstanding. Our original performance goal was to achieve 1 Angstrom rms accuracy and repeatability for surface spatial periods from 0.5 to 5.0 mm. Table II.2 lists the actually achieved accuracies and repeatabilities, showing more than an order of magnitude improvement over the goals.

Note that Table II.2 lists accuracies, rather than repeatabilities. Actually, the accuracy and the repeatability

are essentially the same. With our measurement approach, we are in the very unusual position to be able to characterize both, and to have them be comparable. The method by which we characterize accuracy has many steps, but the most important step is unique. We simply remove the calcite and scan a test piece in the usual manner. Now the measurement beams are exactly coincident, so that the difference in test piece slope that they encounter is exactly zero. In this condition, then, the instrument should produce a surface height profile that is precisely zero. This turned out to be an extremely diagnostic procedure for us. The first time we ran the experiment, as discussed in Section II.5.3, we did not obtain a zero height profile, but a very substantial and repeatable profile. This systematic error was traced to stresses induced by the scanning stage. After we eliminated the stress through modified mounting of the instrument, the systematic error disappeared, and we were left with very small, random surface height profiles. Their amplitude was in fact essentially the same as the repeatability, demonstrating that Table II.2 shows both accuracy and repeatability.

During the course of the project, we performed hundreds of measurements. To repeat them all here would be impractical. Figures II.22 through II.25, however, are representative, showing a 40 mm scan and a 5 mm scan on a piece of BK-7, coated with 100 microns of epoxy and a thin layer of gold. (The test piece was one of several pieces we obtained from potential Phase III customers, and was fabricated to test substrate structural print through on the epoxy outer surface.) Figure II.22 shows the surface height profile from two successive 40 mm scans, and the corresponding difference plot. The notes at the top of the plots indicate that only base curvature,. a second order polynomial, has been removed from the data. Note first that the two profiles are so similar that they are almost indistinguishable. As shown, the difference is a mere 3.37 Angstroms rms. If we divide this by $2^{1/2}$ to get the estimated single scan accuracy, we get approximately 2.4 Angstroms rms. This is entirely consistent with the values shown in Table II.2. Figures II.23 and II.24 show similar information for a 5 mm scan on the same piece, first with only curvature removed (Figure II.23 - '2nd Order Polynomial Removed'), and then with a cubic removed (Figure II.24 - '3rd Order Polynomial Removed'). We emphasize that the plots in Figures II.23 and II.24 correspond with the original goals for the instrument, which defined an rms accuracy of 1 Angstrom for a scan length (longest spatial period) of 5 mm. Note the impressive factor of 10 improvement over the already ambitious goals.

Figure II.25 shows the Power Spectral Density (PSD) functions, first for the two individual 40 mm profiles (see Figure II.22), and then for their difference. The upper plot shows the statistics on the test piece surface, while the lower plot shows

the measurement noise statistics. Note the rapid falloff of the upper plot at a spatial frequency of approximately 3 to 4 cycles per mm. Clearly, the instrument is filtering, or attenuating, the data for higher spatial frequencies. In other words, the upper plot shows the bandpass of the instrument. (Note the improvement over the originally specified cutoff of 2 cycles per mm, or 0.5 mm spatial periods.)

The lower plot in Figure II.25 (the measurement noise PSD) is particularly interesting. To make sense of it, though, we need to describe further the theoretical performance of the instrument. As with any measurement instrument, performance can be conveniently characterized with the PSD of the instrument's noise. The noise PSD is defined as the apparent mean square surface error per unit spatial frequency to be expected in the case of a perfect test piece. A common and reasonable theoretical approach is to assume random white noise in the basic physical measurement. In a non-differential direct height measuring instrument, for example, this would imply a constant surface height noise PSD as a function of spatial frequency. In our case, however, it can be shown that random measurement noise in each of the two slope measurements, with a Root Mean Square (rms) value σ_{slope}, corresponds to a constant surface curvature noise PSD given by

$$PSD_{curvature} = (2\ h\ /\ d^2)\ \sigma_{slope}^2 \qquad (13)$$

where σ_{slope} = rms single point slope measurement error
h = spacing between successive curvature measurements
and d = separation between the two beams on the test piece

(Note that in Equation 13, by virtue of the discrete sampling nature implied by the sampling interval h, the highest spatial frequency defined is f=1/h. Also note that all PSD's defined in this report are single-sided. That is, they are not defined for negative spatial frequencies.)

It can also be shown using Fourier derivative identities that a surface height noise PSD can be related to a curvature PSD as follows:

$$PSD_{height} = (1\ /\ (2\ \pi f))^4\ PSD_{curvature} \qquad (14)$$

Equations 13 and 14 can be combined to give the required surface height noise PSD as follows:

$$PSD_{height} = (h\ /\ (8\ \pi^4\ d^2))\ \sigma_{slope}^2\ f^{-4} \qquad (15)$$

Equation 15, then, defines the theoretical surface height noise PSD as a function of the physical parameters (h, d, σ_{slope}) and the spatial frequency f. Note the strong f^{-4} dependence. This

is simply a consequence of doubly integrating the curvature to obtain height. Now compare this functional form with the lower plot in Figure II.25. A falloff of f^{-4} corresponds to a slope of -4 on a log-log plot. On the particular scales in our plot, a slope of -4 corresponds to diagonals across the rectangular grid cells. And, interestingly enough, the plot has this general falloff over quite a large range of frequencies. Note the rise at the lowest spatial frequencies, though, where drifts are apparently becoming important. Finally, note the rather straight line in the plot, labeled at the top as 'AXAF.' This line is the proposed measurement accuracy requirement for mid spatial frequencies for the Advanced X-ray Astrophysical Facility (AXAF). Since our PSD is that of a difference between two plots, we would expect it to be a factor of two higher than the inherent noise PSD. Taking this factor of two into account, we can see that our instrument meets the AXAF goals (which are probably the most stringent mid spatial frequency measurement goals ever proposed) over the entire specified range of spatial frequencies.

One final piece of information to be extracted from Equation 15 is the implied total rms measurement error as a function of scan length, or longest spatial frequency included. Equation 15 implies that the measurement accuracy decreases as the total scan length increases, since lower spatial frequencies (and therefore higher values of f^{-4}) are then involved. To see this, we write the total rms measurement error as the square root of the integral of the height noise PSD over the proper spatial frequency bandwidth as follows:

$$\sigma_{height} = \left[\int_{f\text{-}min}^{f\text{-}max} PSD_{height}(f)\ df \right]^{1/2} \qquad (16)$$

where f-min and f-max are the minimum and maximum spatial frequencies of interest. In the case of a scan length of L, we have

$$f\text{-}min = 1/L \qquad (17)$$

and $$f\text{-}max = 1/h \qquad (18)$$

Assuming L is much greater than h, Equations 15 and 16 can be combined to give the approximate result

$$\sigma_{height} \approx ((h^{1/2}\ L^{3/2}\ )\ /\ (2\ \pi^2\ 6^{1/2}\ d))\ \sigma_{slope} \qquad (19)$$

(The approximation involves setting f-max to infinity. In practice, where L is usually two or more orders of magnitude larger than h, the error is completely negligible.)

We see from Equation 19 that the total rms height measurement

error increases as the (3/2) power of the scan length. We have verified this behavior on our instrument, and have in fact used measured height noise PSD's to refine our estimates of the single point slope measurement noise. Table II.3 gives typical measurement parameter values used or obtained during our breadboard instrument development. These values give predicted rms accuracies that are generally consistent with Table II.2, although the temporal drifts become important for scans in the range of 50 to 100 mm in length.

To complete this section, Figures II.26 through II.30 show some other miscellaneous measurement plots. Each plot shows the profiles from two independent scans, showing the instrument's sensitivity and repeatability. In each case, the two profiles are nearly indistinguishable. The surfaces cover a wide range of optical forms, from flat to fast asphere to cone-shaped. Each plot is described in detail in its caption.

II.5.3 Sources of Drift

We have referred several times to temporal drift. By this we mean any variation in the curvature perceived by the instrument on the test piece. Drift, then, is a catch-all description for almost all measurement errors, apart from true random electronic and photon noise. The investigation of various kinds of drift occupied a large portion of the project. In this section, we describe (1) several of the most important types of drift found; (2) some factors identified as <u>not</u> contributing to drift; and (3) the last remaining remnants of drift.

One of the earliest forms of drift appeared as a curvature measurement that rose as a linear function of scanning position. Of course, we at first thought that the test piece had such a linearly varying curvature on it. But, the value was large enough to be suspicious, so we ran the same measurement with no calcite in place. (As previously discussed, this the measurement beams are then <u>exactly</u> coincident, so that the difference in test piece slope that they encounter (i.e., the measured curvature) is exactly zero. In this condition, then, the instrument should produce a surface height profile that is precisely zero.) We found that the linearly rising curvature was completely unaffected by removing the calcite. We theorized, then, that the instrument was being warped as it was scanned along the test piece.

To attack this problem, we used several approaches. They all involved mechanically isolating the optics from the stage. We tried different approaches for attaching the detector box to the optics baseplate, and different approaches for attaching the optics baseplate to the stage. Most of the approaches involved wire or blade flexures. The idea was to prevent the very small

(but very powerful) distortions of the stage from similarly warping the optics and giving us an artificial curvature reading. We found that the flexure approaches worked extremely well. Figure II.31 shows two plots of measured curvature as a function of time during a constant velocity scan. (Thus the plots can be thought of as measured curvature as a function of scan location.) The plots were made with no calcite. The first plot corresponds to bolting the optics baseplate directly to the stage, while the second plot corresponds to a flexure attachment. (The "U" and "V" annotations refer to the drift in the u and v, or x and y, directions on the detectors. The "U" direction is the important data, since the u or x direction is along the scan.) Note the tremendous improvement. Note also that there is still some residual jitter, which is due to scanning related vibrations and is unimportant.

As a final note on this first type of drift, we eventually settled not on a wire flexure attachment for the baseplate to the scanner, but on simply using three bolts with flat washers between the baseplate and the scanner. This is a much sturdier mount, with fewer vibration and thermal sensitivities. The in-plane stresses that it allows were found to be unimportant.

A second very interesting drift was a very long term drift (periods of several hours). Since the instrument is recalibrated before and after every scan, such a long term drift would usually not pose a problem, but the magnitude was so large as to be worrisome. Another problem, which we thought was unrelated, was that the power in each of the two laser beams drifted. In particular, the sum of the two powers remained the same, but the split between the two beams changed. We were convinced that thermal changes were ultimately the source of both of these problems. We tried heating and cooling several elements, with little success. The Acousto Optic Modulator (AOM), however, did show a marked sensitivity. After exploring several theoretical possibilities, we performed a complete polarization analysis of the optical train (laser, AOM, half wave plate, and polarizer). We left the rotation angles of all the elements as free parameters, and gave the AOM a variable birefringence as well. The final equations for power in the two beams were, needless to say, extremely complicated. However, they demonstrated very clearly that if the laser's polarization was not aligned with the birefringence axis of the AOM, and if the AOM's birefringence changed (e.g., with temperature), then the power levels would indeed drift. We talked with the AOM manufacturer, and found that the AOM crystal is indeed very birefringent, making a large thermal sensitivity very plausible. Our analysis indicated that the problem would be essentially eliminated by aligning the laser beam carefully with the AOM axis. We did this very carefully, and found that the long term drifts (both in measured curvature and in laser power) all but disappeared. Figure II.32 shows

plots of drift before and after we instituted the polarization alignment step. Note the factor of 15 improvement. Finally, it is interesting to note that we could not find any data on the thermal variation of birefringence in the AOM crystal. Our instrument, though, together with our polarization analysis, provides a very practical method for measuring changes in birefringence.

One possible source of drifts that we have not discussed is the electronics. In general, the electronics have performed superbly, but drift is always a worry. To this day, we have never found any appreciable drift source in the electronics, with one interesting exception. We at one point found a drift that always had equal (and opposite) magnitudes in the u and v directions. It occurred to us that such a drift could be accounted for by a single drifting detector quadrant (or its associated amplifier). If this were the case, we would still see the drift if the spot were placed on a quadrant division line, near the edge of the detector, neighboring the drifting quadrant. We would not, however, see the drift under the same conditions if the spot were not neighboring the drifting quadrant. We performed the experiment, and found that indeed only two of the four spot locations gave drift. This defined the bad quadrant. It also turned out that, because of the final polarizing beam splitter, the handedness of the two detectors is opposite. We showed that this was enough information to tell which detector was drifting. So, we pulled out the preamplifier board for the suspected detector, examined the suspected quadrant op-amp chip, and found a marginal connection in its socket. We then removed both preamplifier boards, removed all the op-amp sockets, and soldered the op-amp chips directly to the boards. We have never been bothered by this type of drift since then.

This completes our summary of the drift sources we have identified. Even though the instrument works an order of magnitude better than originally hoped, though, there will always be some limitation on its performance. In our case, there are still drifts that can be as important as the true random electronic and photon noise for long scan lengths (50 to 100 mm and beyond). These drifts have periodicities of tens of seconds. We do not yet know their source. The drifts do not seem to be present until the instrument has been turned on for a few hours. We therefore suspect thermal effects in general, and specifically that the laser goes through some cyclical mode hopping after it has been on for several hours. Figure II.33 shows first a typical mild case of this drift, and then a case where it seems to be gone entirely.

II.6 Modification Definition for Phase III

The objective in this phase of the project was to define

modifications which would be appropriate for a full laboratory version of the instrument, which could be operated by optical metrology personnel. In addition to identifying certain design improvements, we found that some of the flexibilities allowed in the breadboard instrument were actually superfluous.

The Phase III modifications we defined fell into three categories: (1) optomechanical; (2) electronic; and (3) algorithmic.

In the optomechanical area, we identified five specific modifications. The first was to mount all the optics on a separate baseplate, and to mount the baseplate on its side next to the detector box. Having a separate baseplate improves the mechanical isolation of the optics from the scanner. Turning the baseplate over on its side causes any residual out-of-plane disturbances in it to affect measurements across the scan instead of along the scan, thus improving accuracy. The second modification was to provide a cover for the instrument with vent holes for the laser, and a corresponding thermal shield around the laser itself, so that its considerable heat output does not cause drifts. The third modification was to improve still further the accuracy of the positioners for the movable detector. Although the positioner system works very well for near-spherical test pieces, we have shown that we need to extend the accuracy to get accurate, long profiles of extremely aspheric surfaces (e.g., near-cylindrical elements for extreme ultra violet telescopes). By using small air bearing stages and very high resolution holographic encoders (0.01 micron resolution), we believe that we can improve the accuracy for long aspheric profiles by perhaps an order of magnitude. The fourth modification was to make the calcite removable under remote computer control. As previously discussed, the testing without calcite is an important step in various instrument calibrations. The calcite actuation would need to be done in a way that is very repeatable and stable, imparts negligible stresses to the optics baseplate, and consumes little power. We have performed a conceptual layout of a small, kinematic rotarty actuator that accomplishes these goals. The fifth modification was simply to replace the scanner stepper motor with a brushless DC servo motor to reduce vibration.

In the electronic area, we identified three specific modifications. The first was to give the computer access not only to the Detector A and Detector B outputs, but also to the Detector C outputs and the total incident power levels for Detectors A and B. The Detector C output would be extremely useful for building up a calibrated table of required Detector C offset voltages versus implied steering mirror angles. The Detector A and B power levels would allow us to implement a much faster automatic alignment procedure. (Currently the speed of the procedure is limited by the need to interpret the detector

signals when the spot is actually off the detector. Monitoring detector power would be much more straightforward.) The second modification was to provide a real time, wide dynamic range count of scanner encoder pulses. (The pulse count is used to synchronize the computer's data collection within each pixel.) In the breadboard instrument, we provided an 8 bit count only. This proved to be sensitive to noise and rapid fluctuations, so that occassionally the inferred, accumulated count would be off by a full 8 bits (256 counts). The third modification was to make the servo gains and polarities adjustable under computer control. We found that when testing a highly curved test piece, the gain of the servo could be unsatisfactory. This is because a curved test piece changes the relationship between the steering mirror angle and the resulting angle of reflection from the test piece. In the extreme case, when the test piece center of curvature is at the steering mirror, no amount of steering will change the normal incidence on the test piece. In fact, then, when the test piece center of curvature is below the steering mirror, the sense (or sign) of the gain must be reversed, for the same reason that one's reflection appears upside down in a curved mirror whose center of curvature is between the viewer and the mirror.

In the algorithmic area, we identified two specific modifications. The first, as previously discussed, was to implement the double integration algorithm for non-flat test pieces, where the curvature is no longer equal to the second derivative of surface height. The second modification was to implement a histogram capability in the data display software. This would be particularly useful for making a histogram of surface slopes, which would be directly comparable to a spot diagram for a grazing incidence optic.

As mentioned, we did find that some of the originally envisioned flexibilities seemed to be superfluous for a Phase III version of the instrument. In particular, we had originally planned to make the test spots elliptical (to avoid unwarranted smoothing across the scan), and to make their size continuously variable with a zoom system. We found that the smoothing was not at all troublesome, being on the same order as that from the finite size along the scan and from the finite beam separation. Also, we found that the instrument works so well that the optimization of spot size was not critical. Therefore, we would supply an instrument with a single spot size. An instrument dedicated to a different measurement task, such as very long scans, could be configured with different lenses to give larger spots. In the rare case when two spot sizes are desired, we decided that it would be more efficient to use a mechanism (identical to the calcite insertion mechanism) to switch under computer control between two different sets of previously aligned lenses.

We have actually made great progress in the Phase III modification effort, even before the Phase II effort was complete. Customer interest is high, and most of the modifications are rather easily made. At the time of this report, we are in the process of testing a new set of electronics with all the necessary modifications. A modified optical baseplate has also been fabricated and works very well. The algorithm work is underway.

III. Deliverable Hardware and Software

As specified in the contract, the deliverable items consist of (1) quarterly progress reports; (2) final report; and (3) "Measurement of Upper Mid Frequency Errors on Arbitrary Grazing Incidence Optics consisting of: Piezo Pusher for Beam Control, Dual Range Servo, Calcite Window Set, Initial Alignment System, Instrument Scanner System and any other associated components."

In general, Item 3 describes the breadboard instrument, with the specifically listed components and the other associated components, including software. The specifically listed components consist of (1) piezo pusher for beam control (Burleigh PZ-80 aligner/translator, and Burleigh PZ-70-M high voltage DC op-amp); (2) dual range servo (BEI LA12-12 moving coil linear actuators and associated electronics and machined parts); (3) calcite window set (8 custom order calcite pieces from Karl Lambrecht, 12.7 mm square, 4 each 1.0 mm and 1.2 mm thick); (4) initial alignment system (Melles Griot 11-NCM-001 Nanomovers, and Melles Griot 07-TSC-007 steel translation stages); and (5) instrument scanner system (Daedal 110081P-10E-LH 10" wide preciesion stage, 8" travel, Limit/Home options, Daedal RSF 1-micron resolution encoder, Compumotor PC23 3-axis motor controller card and Compumotor LE57-51 stepper motor/driver).

Physically, the deliverable hardware consists of the breadboard instrument mounted on its translation stage, an electronics rack module containing all of the non-computer resident electronics, and assorted miscellaneous components. User requirements include supplying the computer (IBM PC-AT or equivalent with VGA graphics and 1 Mb of expanded memory), and the data acquisition board (Data Translation DT-2823 with software drivers and Data Translation DT-707 screw terminal panel).

The software modules (LINSCAN, SCOPE, AUTO_FND, RUNCENT, and V_OUT) were described in Section II.4.2. All programming was done in Microsoft FORTRAN and Microsoft C. Table III.1 lists all of the FORTRAN programs and subroutines, and Table III.2 lists all of the C programs and subroutines. Miscellaneous program files include a 'make' file (module_name.MAK) and a 'link' file (module_name.LNK) for each module. (These are standard file types for creating and updating programs in a Microsoft

development environment.) Also, there are various files in an INCLUDE directory used for linking. The INCLUDE files are listed in Table III.3. Finally, some of the most commonly routines have been grouped into two libraries, SCOPE.LIB and FIT.LIB. Table III.4 lists the object files in these two libraries.

IV. Summary

Overall, this Phase II project was a great success. We developed two state-of-the-art subsystems (detection and servo), and achieved performance generally more than an order of magnitude better than comparable subsystems in commercial instruments. Most importantly, though, the breadboard instrument as a whole measured more than an order of magnitude more accurately than the original 1 Angstrom goal within the primary spatial period range of 5.0 mm to 0.5 mm. We have defined a useful set of Phase III modifications. Using our own R&D and risk funds, we have already begun some of those modifications, and are pursuing several promising leads for orders for commercial instruments.

V. References

1. P. Glenn, "Robust, sub-Angstrom level mid-spatial frequency profilometry," Advanced Optical Manufacturing and Testing, Baker, Reid, and Sanger, ed., Proc. SPIE 1333 (1990).
2. P. Glenn, "Robust, Angstrom level circularity profilometry," Advanced Optical Manufacturing and Testing, Baker, Reid, and Sanger, ed., Proc. SPIE 1333 (1990).
3. P. Glenn, "Angstrom level profilometry for sub-millimeter to meter scale surface errors," Advanced Optical Manufacturing and Testing, Baker, Reid, and Sanger, ed., Proc. SPIE 1333 (1990).
4. D. Zweig, A. Ledger, A. Anderson, M. Kasseris, J. Moorehead, L. D. LaFleur, and P. B. Reid, "Improved scanning Fizeau interferometer for measuring large grazing-incidence optics," Advanced Optical Manufacturing and Testing, Baker, Reid, and Sanger, ed., Proc. SPIE 1333 (1990).
5. P. Z. Takacs, S. C. K. Feng, E. L. Church, S. N. Qian, and W. M. Liu, "Long Trace Profile Measurements on Cylindrical Aspheres," Advances in Fabrication and Metrology for Optics and Large Optics, Arnold and Parks, ed., Proc. SPIE 966, 354 (1989).
6. R. G. Lyon, D. A. Zweig, P. B. Reid, and A. Sarnik, "Comparison of mid-spatial frequency axial figure metrology methods for the Advanced X-ray Astrophysics Facility (AXAF)," Advanced Optical Manufacturing and Testing, Baker, Reid, and Sanger, ed., Proc. SPIE 1333 (1990).
7. N. DeFilippis, P. Glenn, and R. Cahill, "Assembly and alignment of the AXAF/TMA," Grazing Incidence Optics, Osantowski and Van Speybroeck, ed., Proc. SPIE 640, 155 (1986).

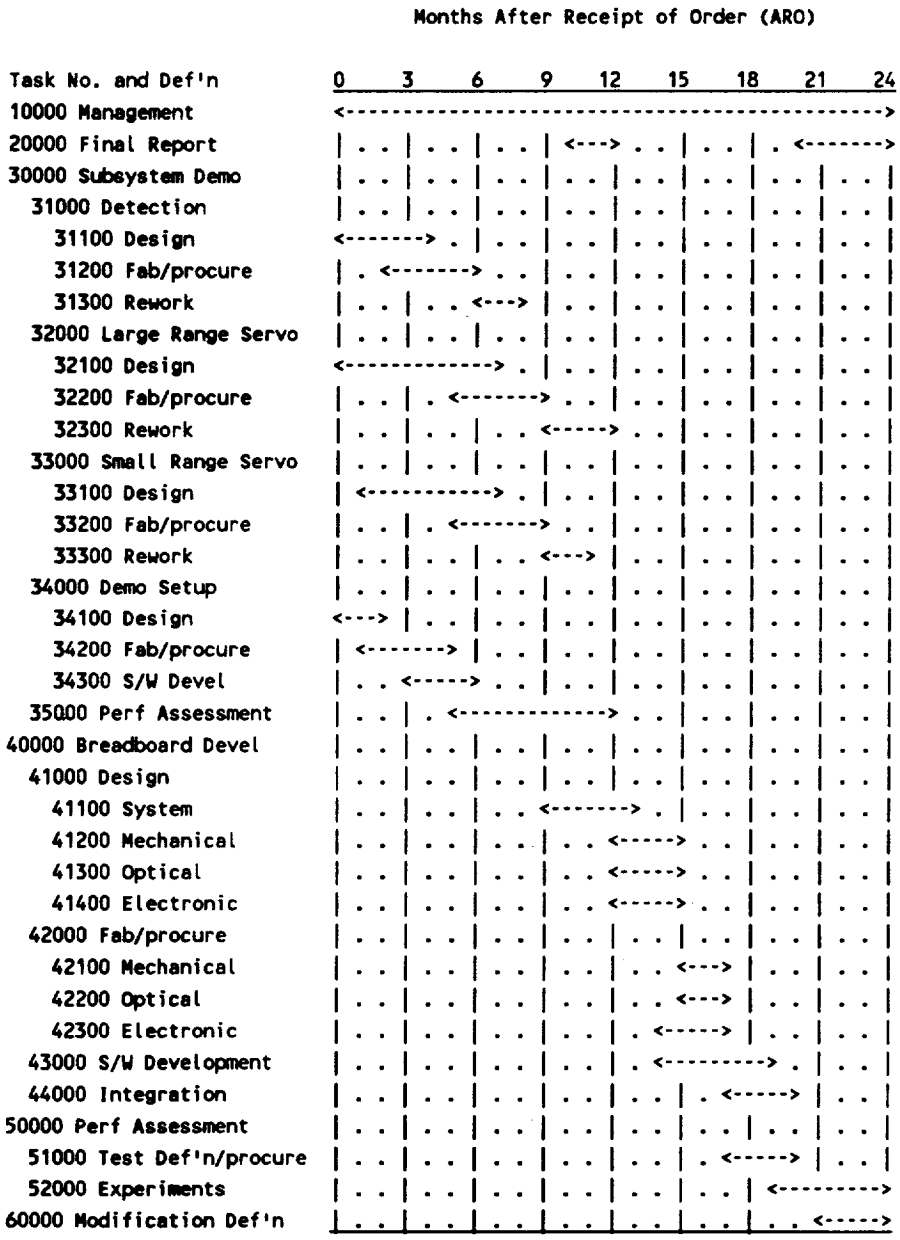

Table I.1 Original schedule and task definitions.

Detection subsystem:
Input: Wavelength = 0.6328 micron; power = 8 micro-watts; modulation rate = 500 kHz
Output: Demodulated, filtered, sampled at 12 bits, 10 kHz

Large range servo subsystem:
Actuator: DC servo motor
Input: (1) Proportional Integral Differential (PID) signal from detection subsystems
(2) Signal from instrument scanner for following test piece base radius
Constant rotation rate: Up to 3 degrees per second
Variable rotation rate: Precision approx 0.1 micro-radian, rate approx 7 kHz

Small range servo subsystem:
Actuator: Piezo electric pusher stack
Input: PID signal from detection subsystems
Range: On the order of 30 microns
Response: Precision approx 0.01 micron, rate approx 1 kHz

Initial alignment subsystem:
Mechanism: Motor driven translation stage
Range: Up to $\pm$25 mm
Response: Precision commensurate with detector error signal noise, rate non critical

Instrument scanning:
Speed: Up to 10 mm/sec
Range: 100 mm for data taking, 300 mm for rough placement

Mechanical structure:
Detector-to-detector vibration of 1/20 wave RMS

Optical train:
RMS wavefront micro roughness < 60 Angstroms RMS (gives < 4% instrument distortion). Wavefront error $\leq$ 1/14 wave RMS, except for spherical aberration < 1/4 wave RMS. Spot radius on test piece from .02 mm to .1 mm.

Software:
Must be modular, user friendly, menu driven, providing the following functions:
Provide control signals for electronic subsystems
Read initial alignment data to give base radius
Read digitally converted instrument data
Process instrument data into height data
Perform Kalman filtering, interpolation, and division by known instrument transfer function
Produce polynomial, PSD, and ACV data
Store, average, subtract, compare data sets

Table I.2 List of the various subsystems and aspects of the breadboard instrument, and corresponding technical goals.

distance (laser - 1st lens):	494	580	494	580
focal length (1st lens):	30	20	30	20
distance (pinhole - 2nd lens):	72.3	72.2	125.4	125.2
focal length (2nd lens):	62.9	62.9	100	100
distance (2nd lens - test piece):	500	500	500	500
1/e^2 radius on test piece:	0.091	0.057	0.052	0.033
distance (laser - 1st lens):	315	315	315	315
focal length (1st lens):	30	40	30	40
distance (pinhole - 2nd lens):	72.2	72.2	125.3	125.5
focal length (2nd lens):	62.9	62.9	100	100
distance (2nd lens - test piece):	500	500	500	500
1/e^2 radius on test piece:	0.098	0.133	0.056	0.076

Table II.1 Design examples for beam conditioning optics. In all cases, the 1/e^2 radius from the laser is 0.405 mm.

Longest Spatial Period Included (mm)	Root Mean Square Accuracy (Angstroms)
1	<0.1
5	<0.1
10	0.2
50	2
100	6

Table II.2 Typical accuracies as a function of scan length, or longest spatial period included.

Parameter	Typical Value Used or Obtained
test beam diameter	0.3 mm
test beam separation (d)	0.3 mm
sample spacing (h)	10 microns
single point slope msmnt error (σ_{slope})	40 nanorad

Table II.3 Measurement parameters used or obtained during breadboard instrument development.

ALLCAL	GET_AB
AR_PSD	GET_BB
AUTO_AB	GSBUMP
AUTO_BB	IFCTR
AUTO_FND	KB_READ
AXSPEC	KB_READY
A_OFFSET	LINSCAN
BBDATA	POW_EVA1
BIAS_MID	POW_EVA2
CAB_MOD	PSD2
CAL_VIEW	RAW_READ
CHAR	RAW_WRIT
CIRCSCAN	RUNCENT
CNFGRD	RUNTURBO
COF_SQR1	SCN_CNVR
COF_SQR2	SCN_DRF1
CRAP	SCN_DRF2
CRC_ENDM	SCN_FILT
CRC_PRMS	SCN_IHGT
CRC_VIEW	SCN_ISLP
CRC_VSUB	SCN_PRMS
CTR_WAIT	SCN_SING
C_CLOCK	SCN_VIEW
DA_ARROW	SCN_VSUB
DET_CENT	SCN_WRIT
DET_RING	SCOPE
DET_SGNL	SCP_CURS
DFOUR2	SCP_DRAW
DNEWT	SCP_INI2
FASTDATA	SCP_INI3
FIL_QY	SCP_INIT
FIL_RD	SCP_TERM
FIL_WR	SCP_UPD2
FIND_A	SCP_UPD3
FIT_FIN1	SCP_UPDT
FIT_FIN2	SCP_WRT1
FIT_FOR1	SHOWKEY
FIT_SIG1	SOLVMAT1
FIT_SIG2	STAT1D
FIT_UPD1	TO_UP
FIT_UPD2	TRY
FOR_EVA1	TURBOBB
FOUR2	TURBOCAL
FOUR2EM	V_OUT
GETCLOCK	

Table III.1 Listing of FORTRAN programs and subroutines.

ALIGN
AR_MAIN
AR_MANIP
CATCH
CATCHTST
DATACOLL
DIGIF
DRIVER
EMMDRIVE
ERROR
EXPANDED
HISTGRAM
INTEREST
MENU
NANO
NANODRIV
OLDDC
PC23
PC23DRIV
PC23TLK
PLOT
PLOTDRIV
RAMDISK
RS232TLK
SRVODRIV
STRINGS
TEST
TRANSACT
T_AND_H

Table III.2 Listing of C programs and subroutines.

BAUER.H
ATLDEFS.H
ATLERRS.H
ERROR.H
BAUER100.H
SCAN1.CMN
SCOPE1.CMN
C_INTRFC.FI
SCOPE.FD

Table III.3 Listing of miscellaneous linking files in the INCLUDE directory.

SCP_CURS	POW_EVA1
SCP_DRAW	POW_EVA2
SCp_INI2	COF_SQR1
SCP_INI3	COF_SQR2
SCP_INIT	FIT_SIG1
SCP_TERM	FIT_FIN1
SCP_UPD2	FIT_UPD1
SCP_UPD3	FIT_UPD2
SCP_UPDT	FIT_SIG2
SCP_WRT1	SOLVMAT1
	FIT_FIN2
	FIT_FOR1
	FOR_EVAL

Table III.4 Object files in the SCOPE (left column) and FIT (right column) libraries.

		Number of simultaneous, neighboring measurement locations	
		One (Non-differential)	Two (Differential)
Physical quantity being directly measured	Surface Height	Stylus profilometers Interferometers	Shearing interferometers Slope-measuring profilometers
	Surface Slope	Autocollimators X-ray alignment instruments	Curvature profiling technique

Figure I.1. Grouping of measurement instruments by the physical quantity measured and the number of simultaneous measurements taken.

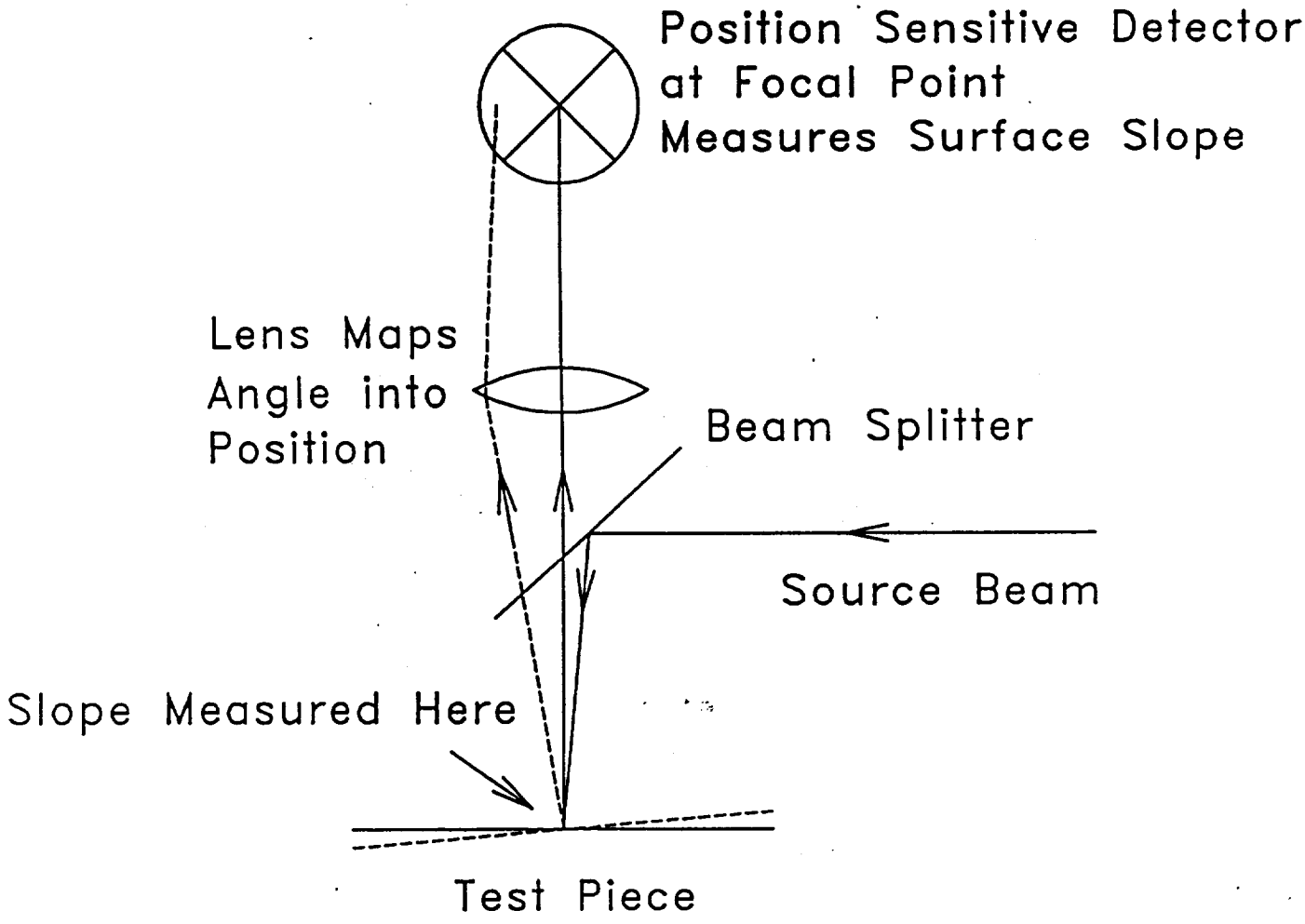

Figure I.2 Slope measurement at a single point. The position of the focused spot on the detector is proportional to the local test piece slope.

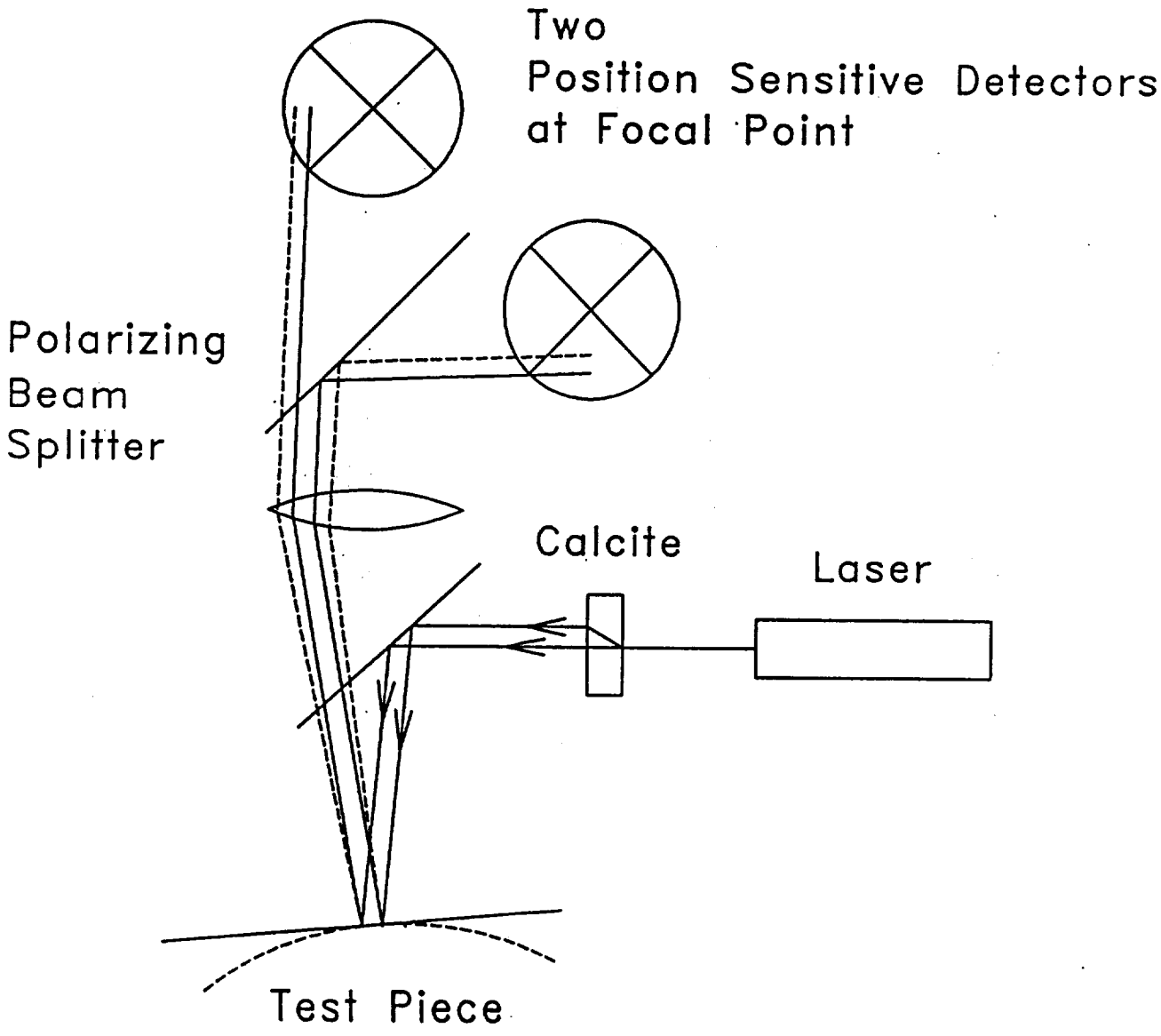

Figure I.3 Differential slope measurement. The difference between spot positions on the detectors is proportional to the local test piece curvature.

Steering Mirror Allows Auto Alignment/Tracking

Movable Detector Allows Base Radius Compensation

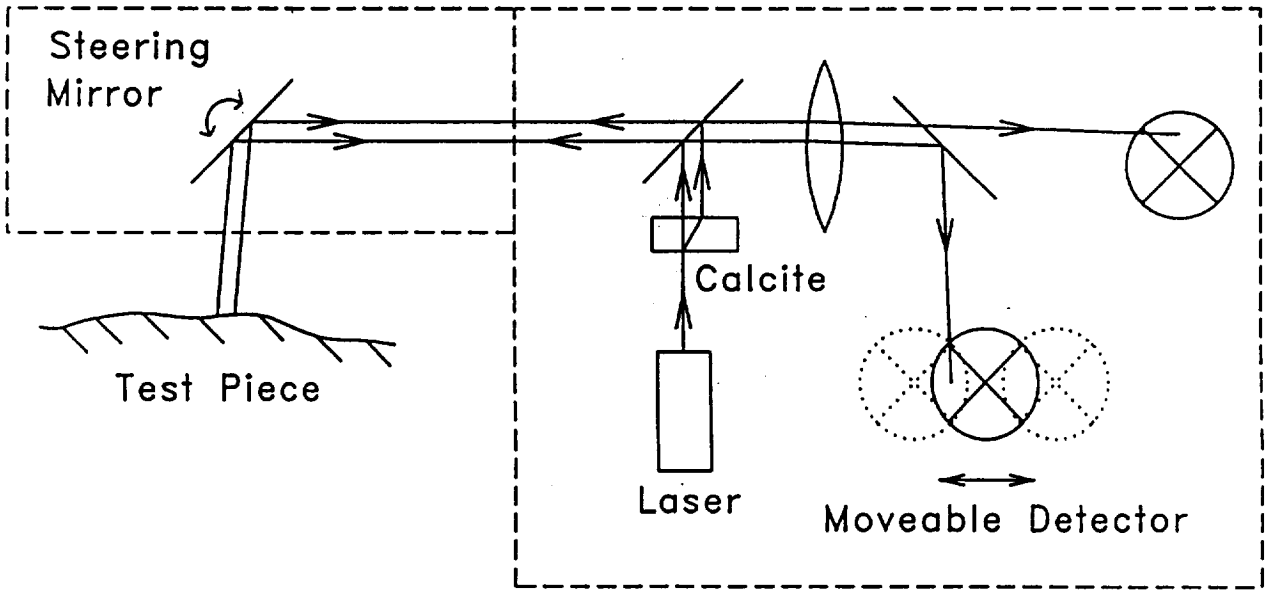

Figure I.4 Steering mirror and movable detector. The steering mirror is inside a measurement arm, which is rigidly attached to the main instrument body. The entire instrument is scanned along the test piece.

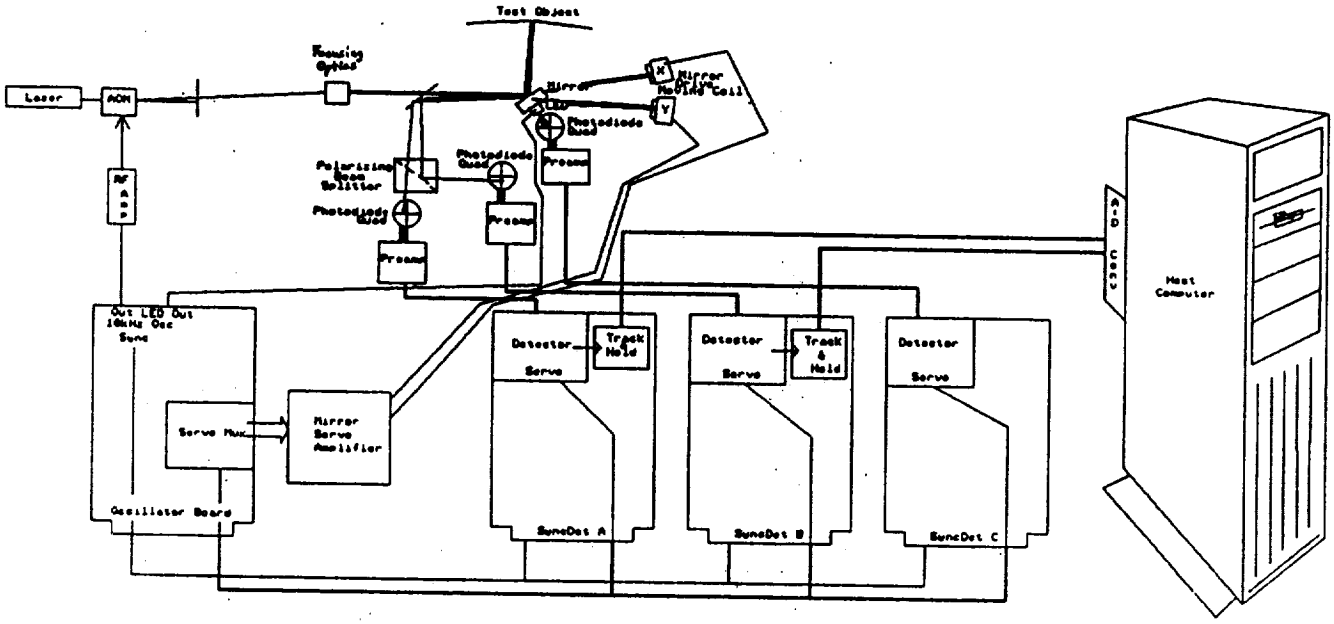

Figure II.1 Electronics block diagram.

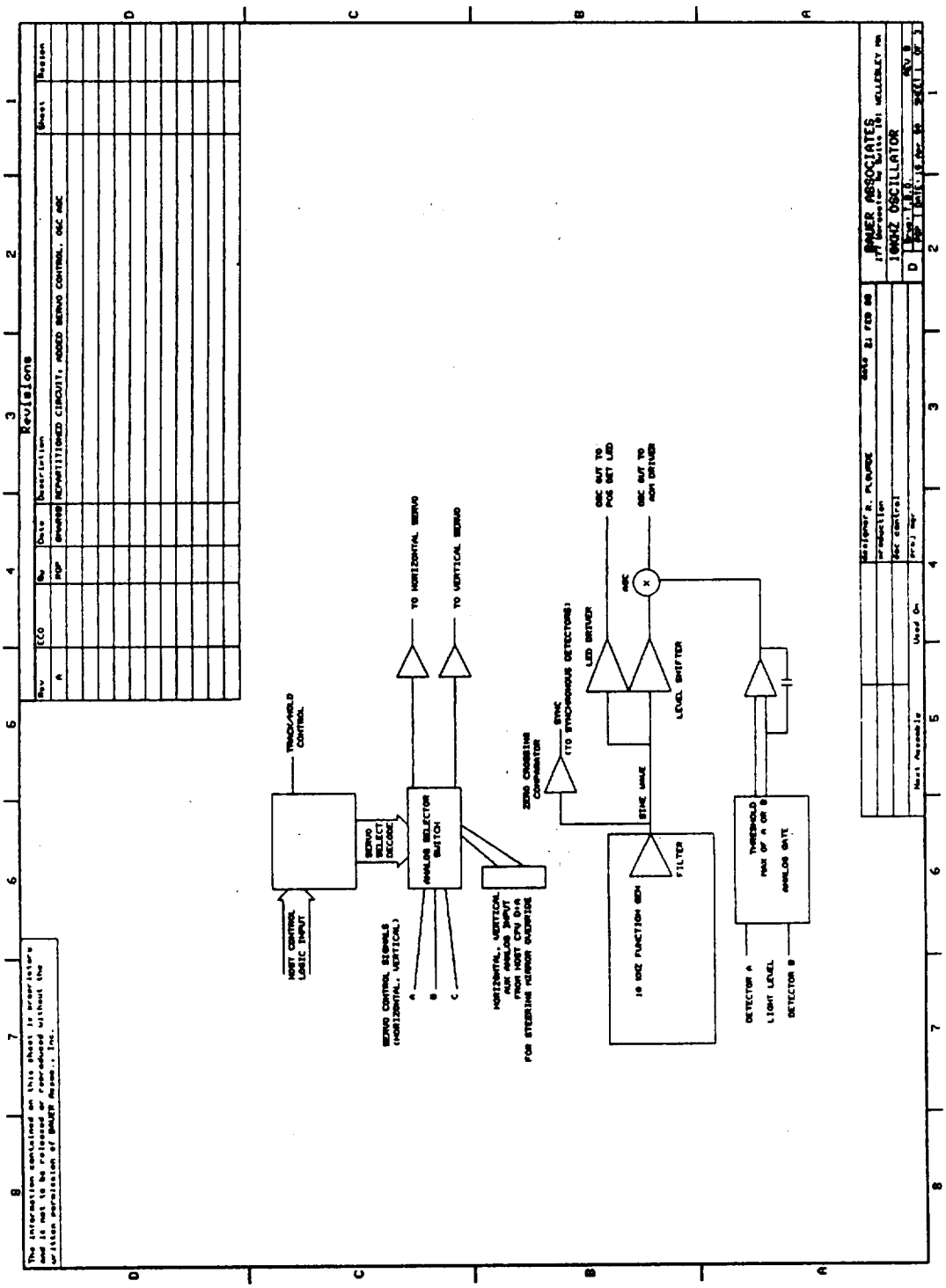

Figure II.2 Oscillator / Feedback Select board block diagram.

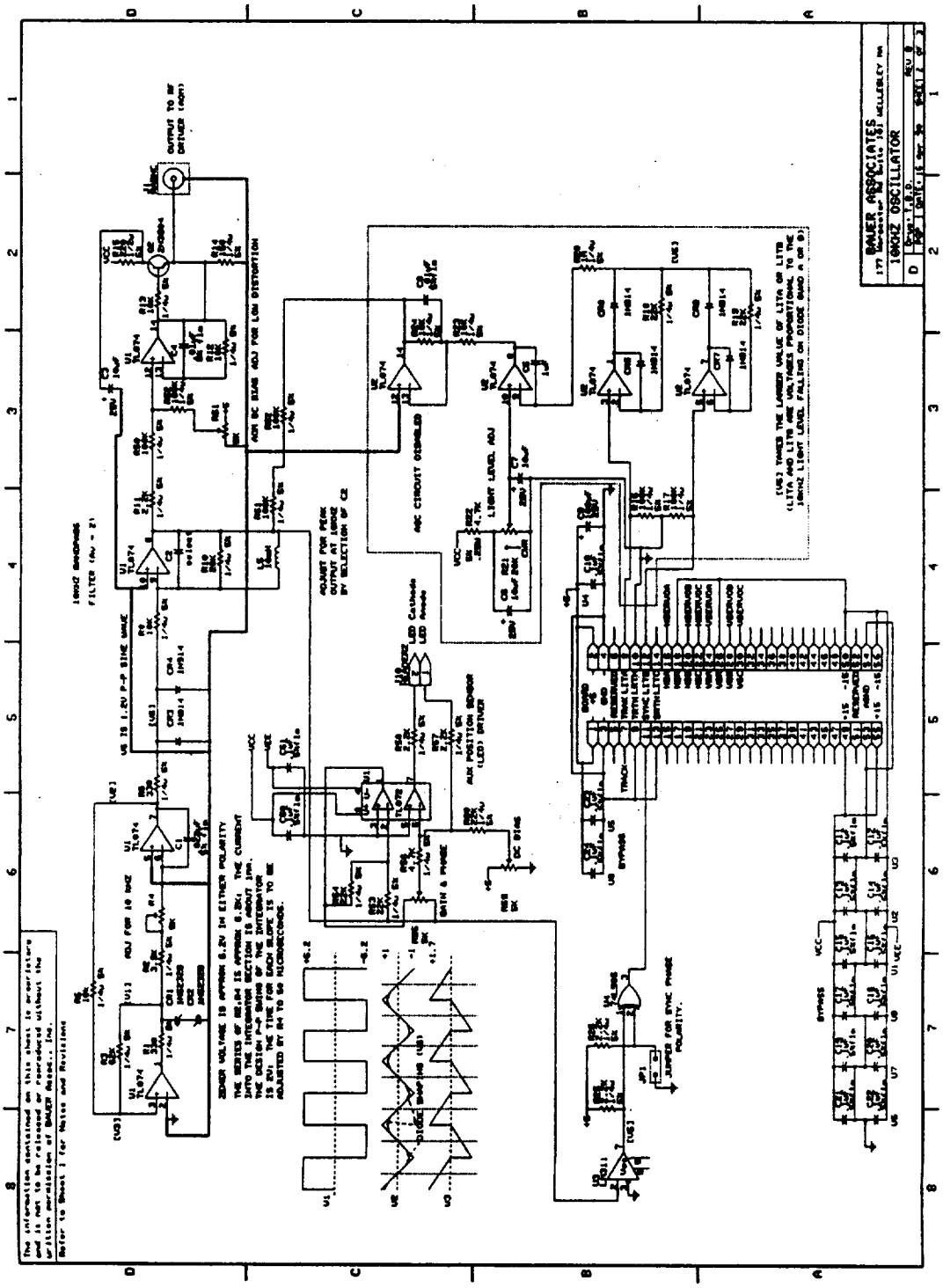

Figure II.3 Oscillator schematic.

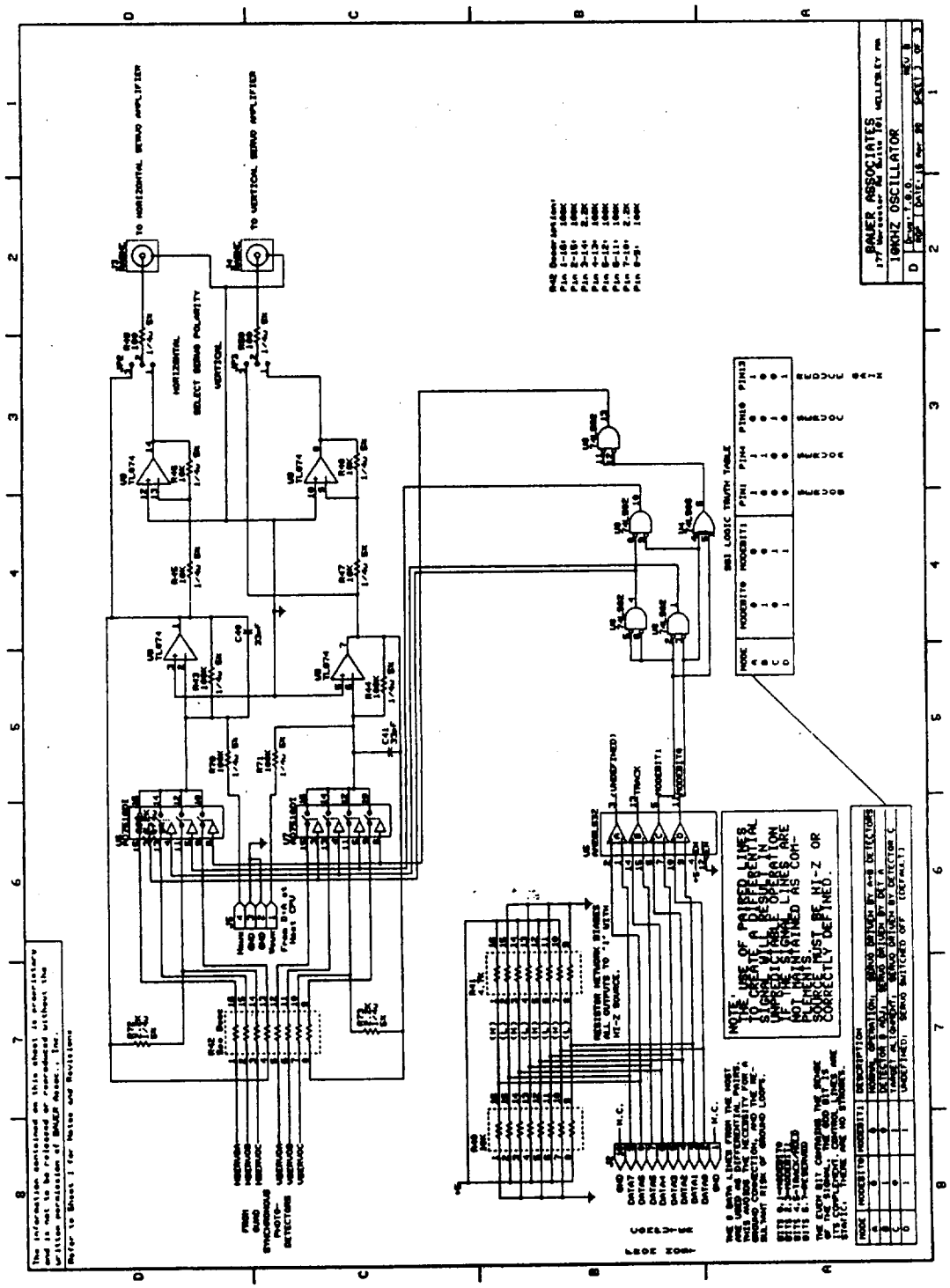

Figure II.4 Feedback selector schematic.

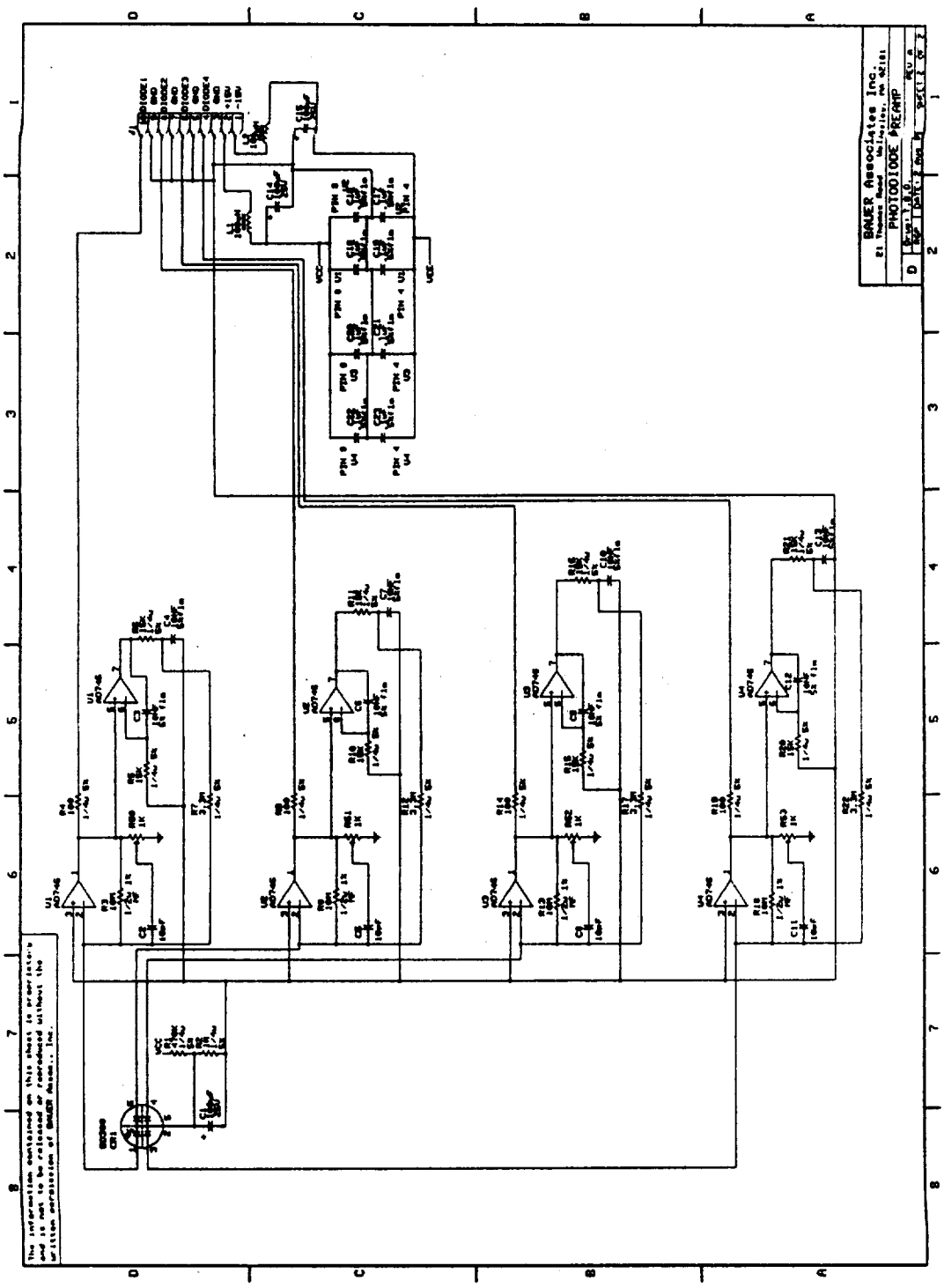

Figure II.5 Detector preamplifier schematic.

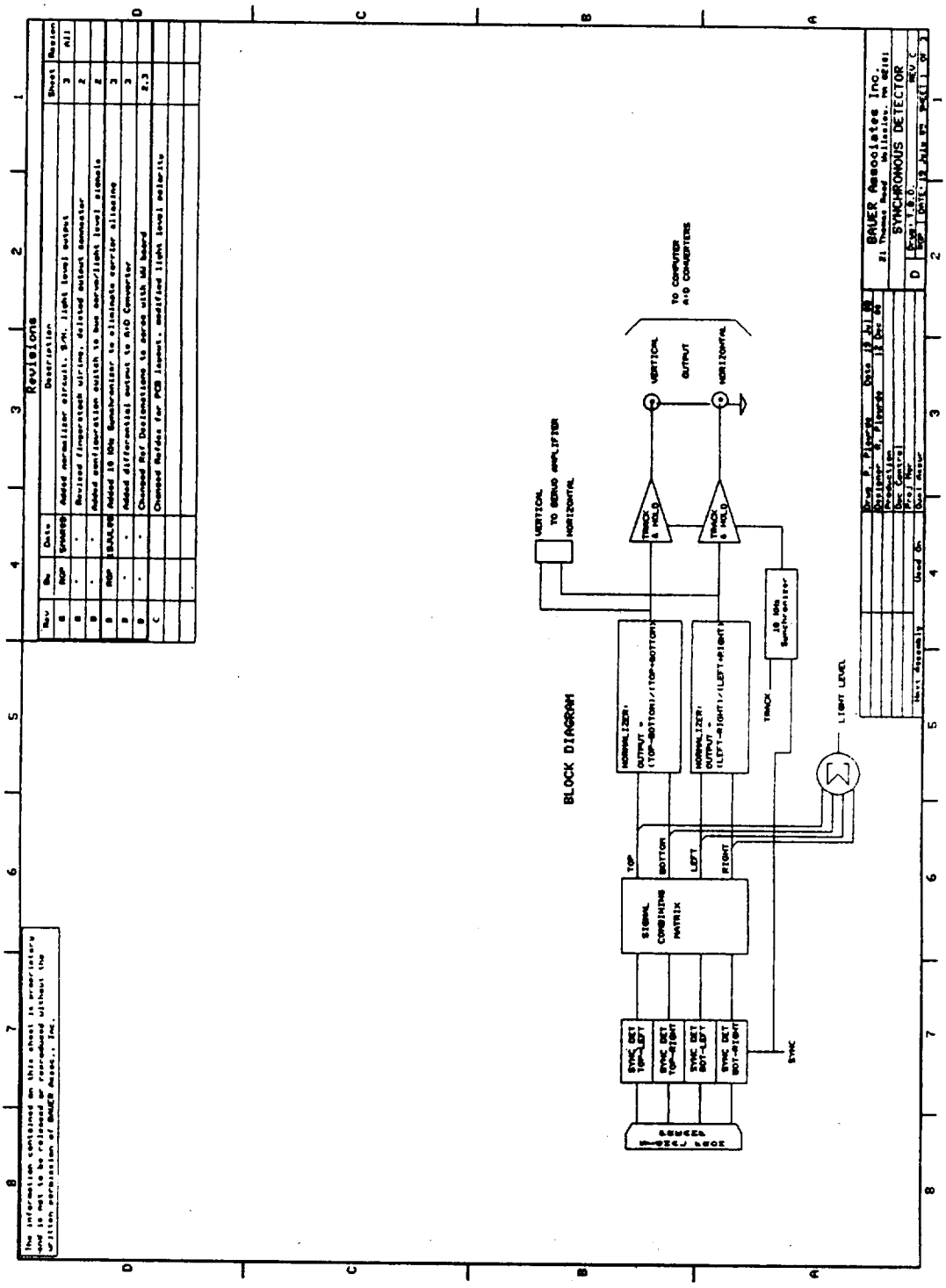

Figure II.6 Synchronous Detection board block diagram.

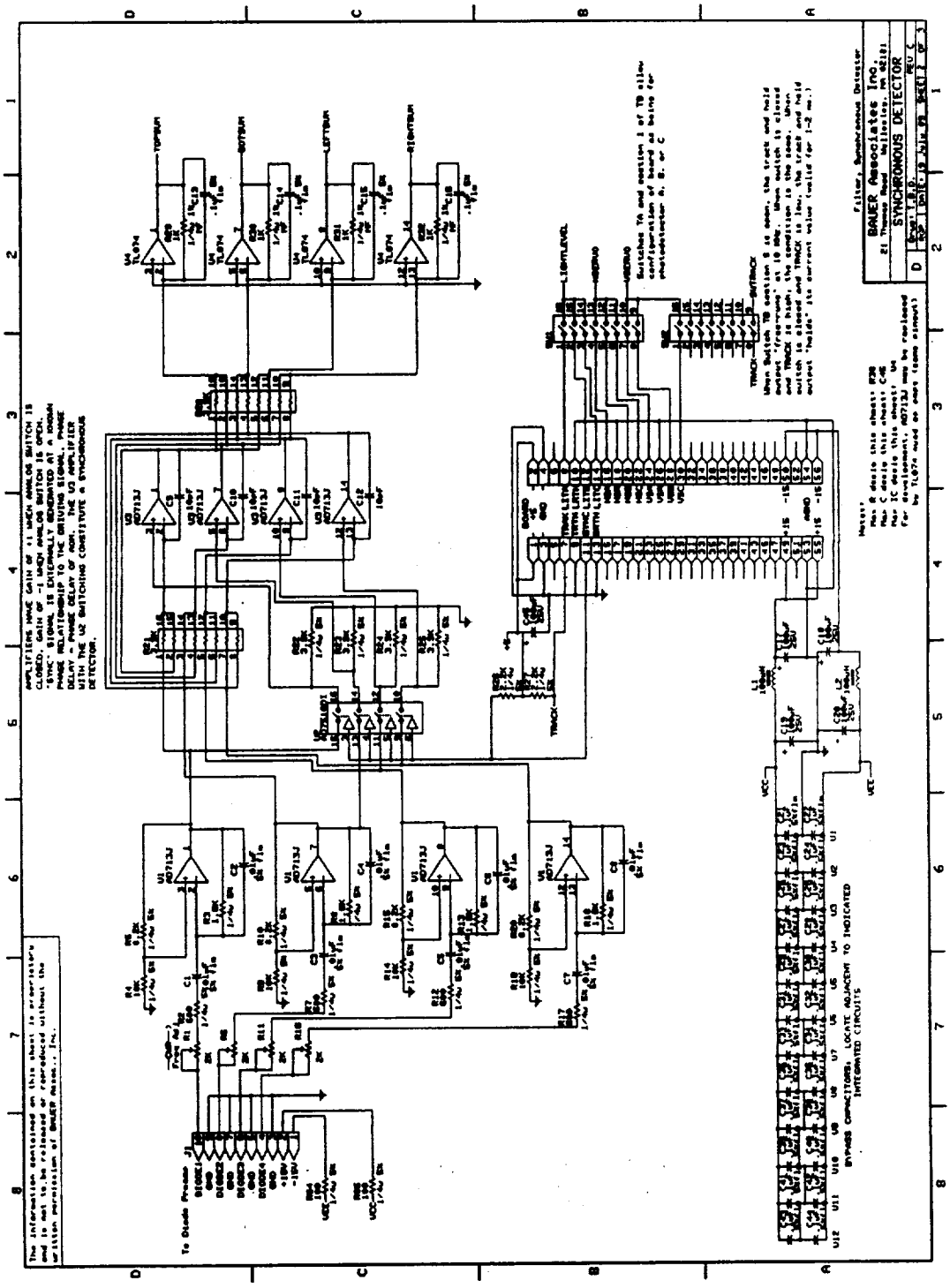

Figure II.7 Filter and synchronous detector schematic.

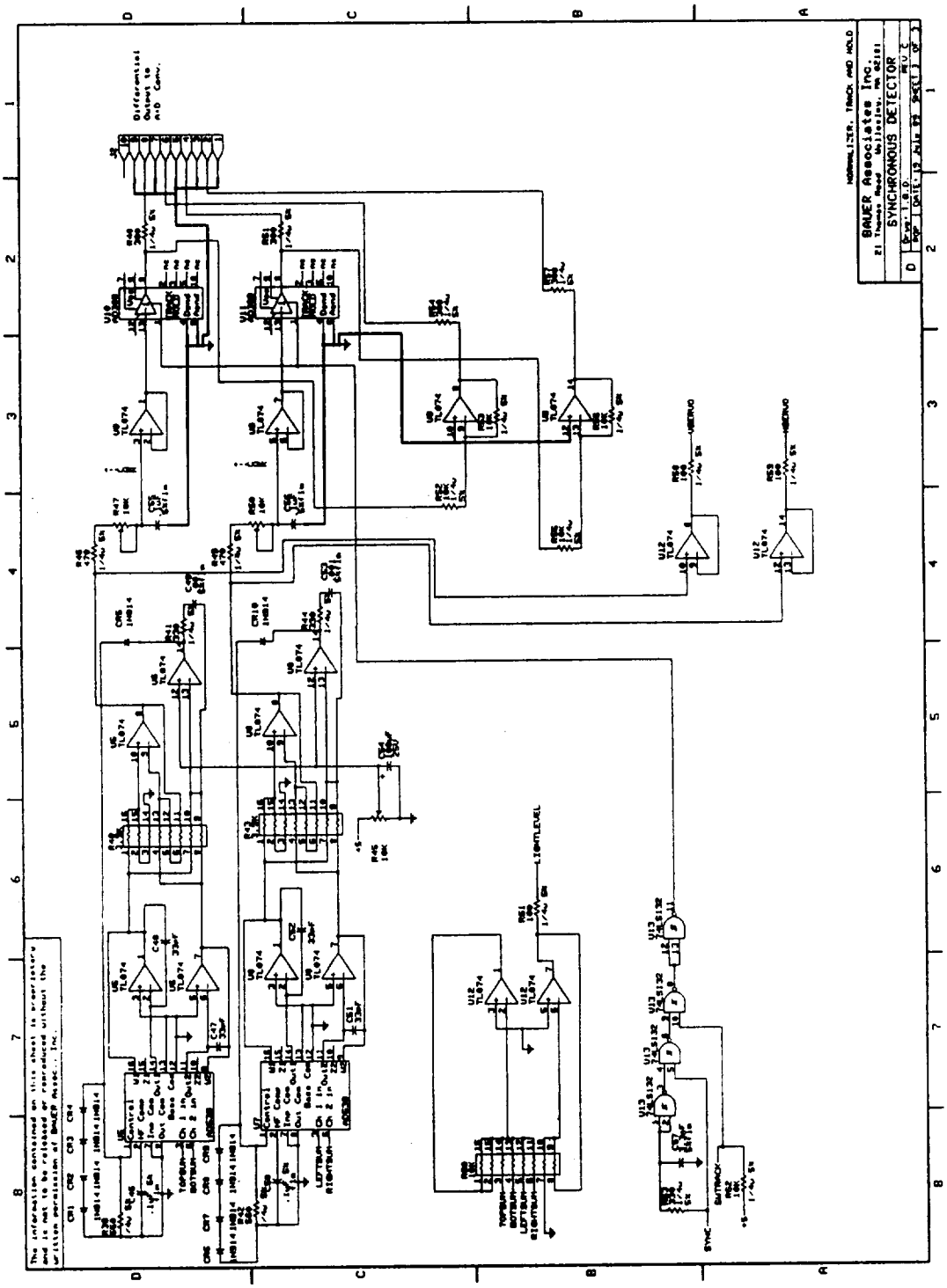

Figure II.8 Normalizer and track and hold schematic.

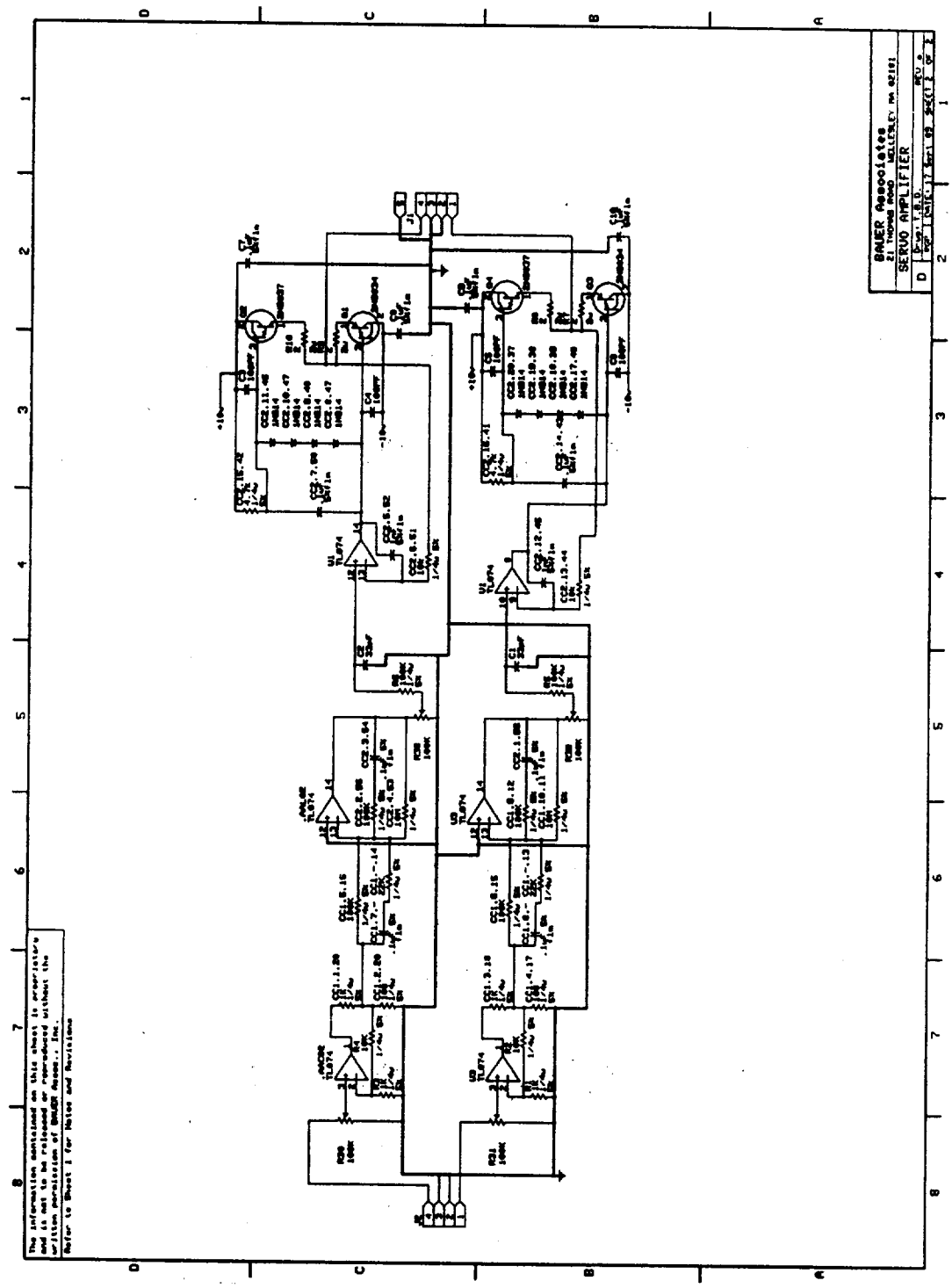

Figure II.9 Servo Amplifier board schematic.

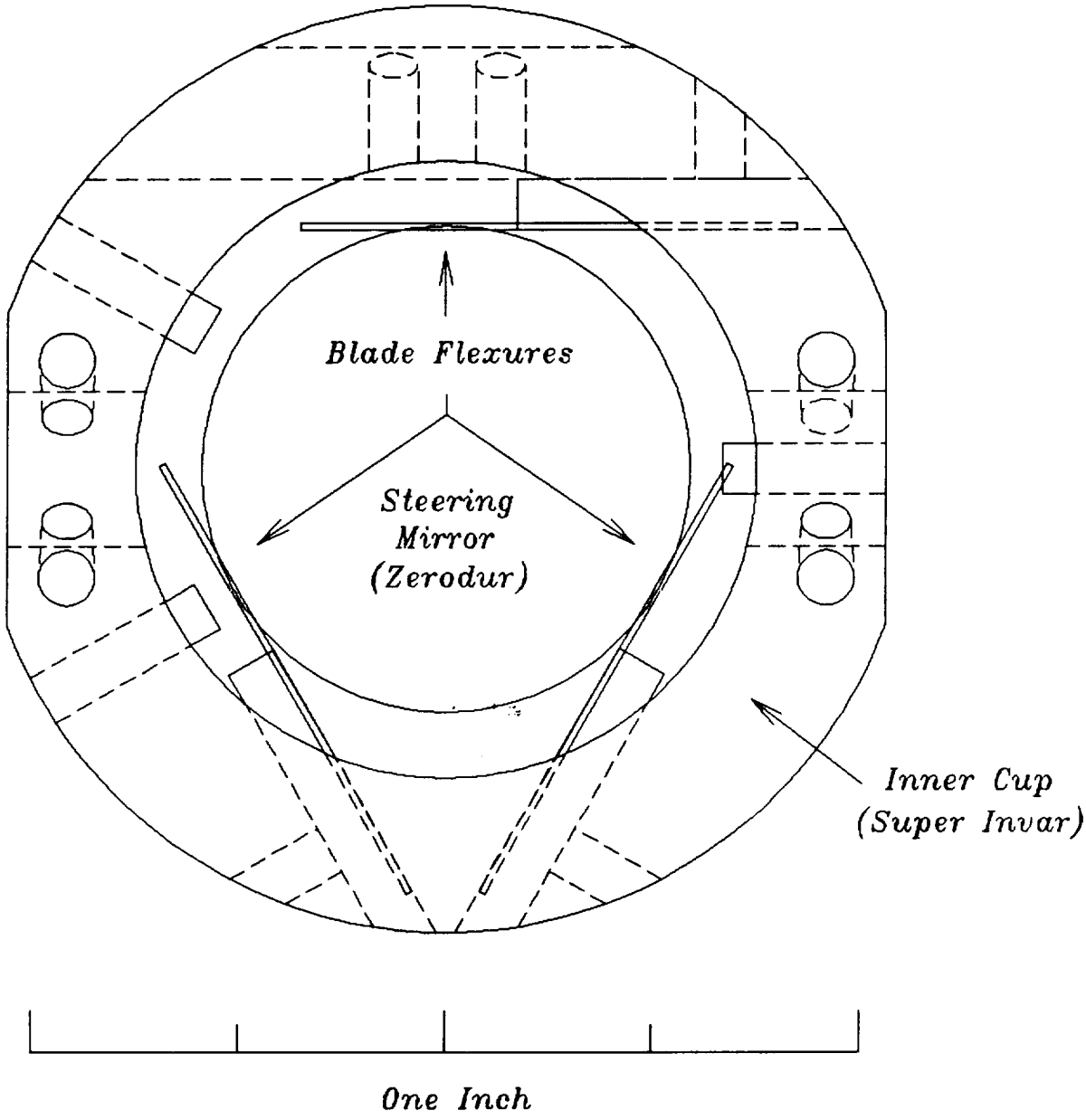

Figure II.10 Steering mirror and inner cup.

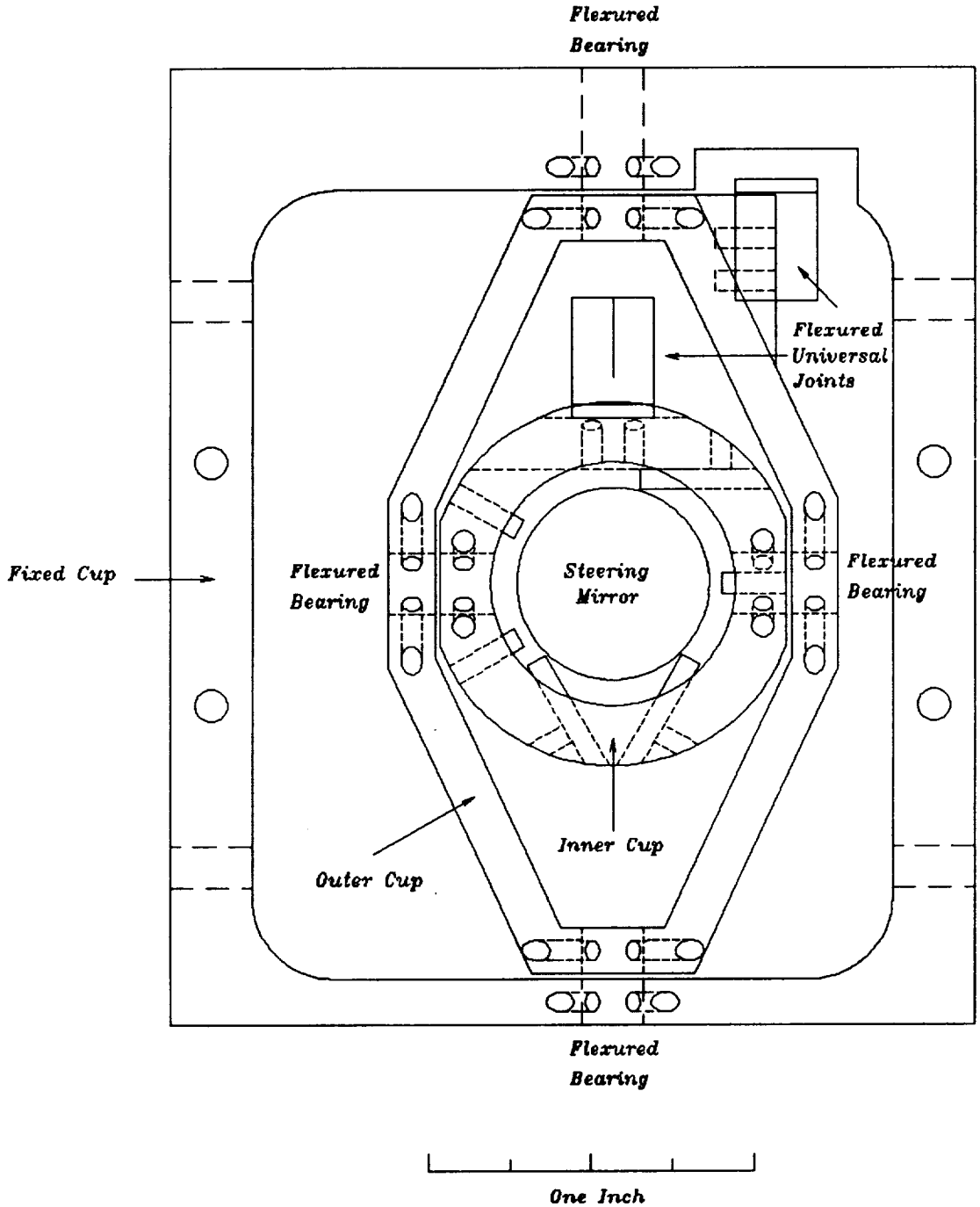

Figure II.11 Mirror, inner cup, outer cup, and fixed cup.

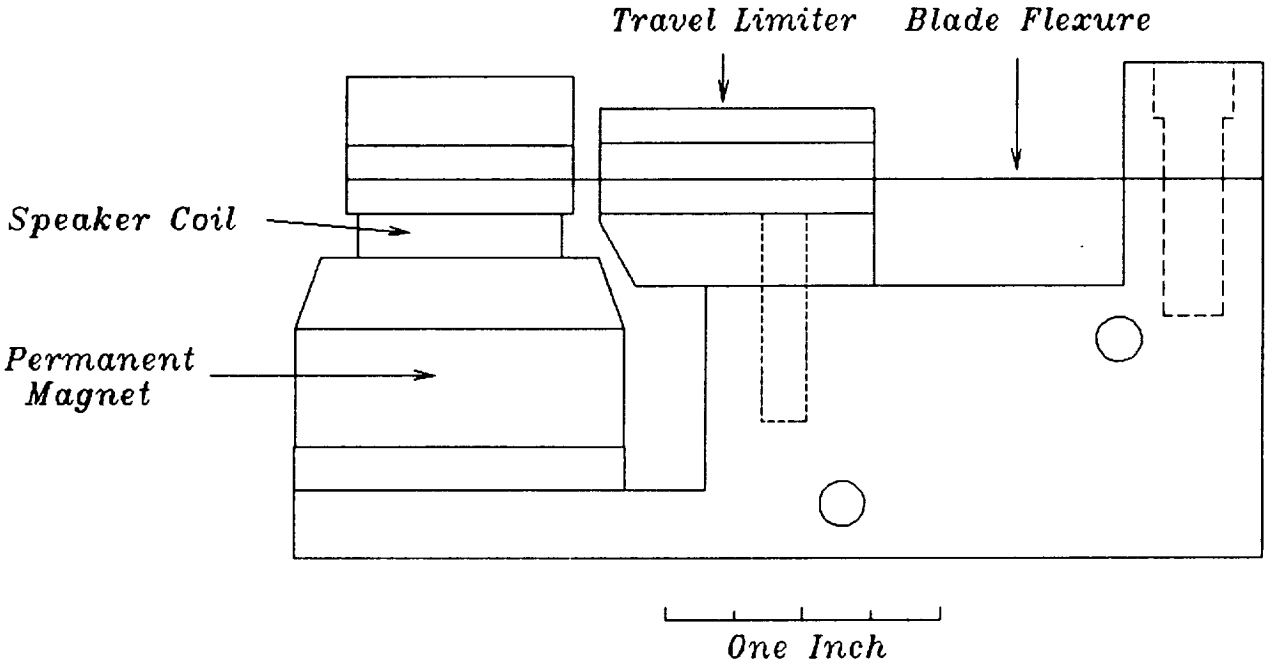

Figure II.12 Side view of a voice coil actuator.

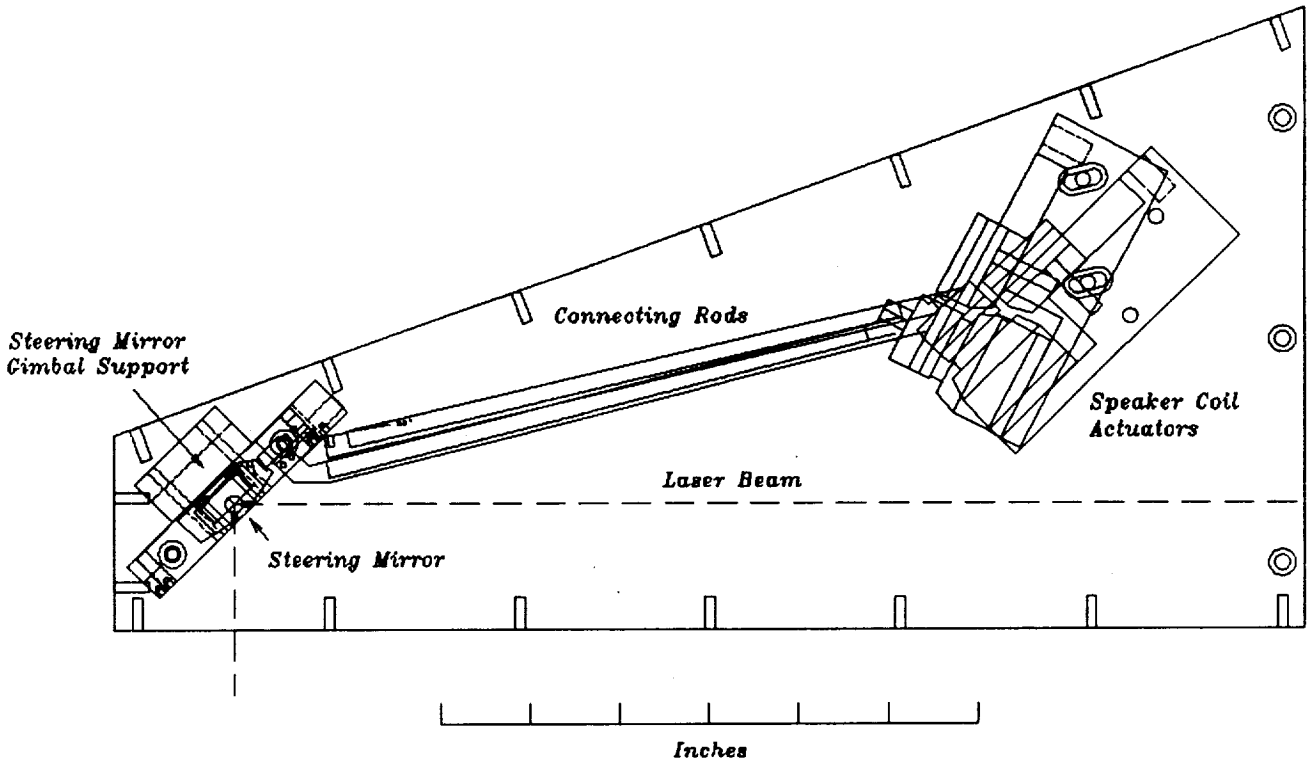

Figure II.13 Measurement arm conglomerate cutaway view.

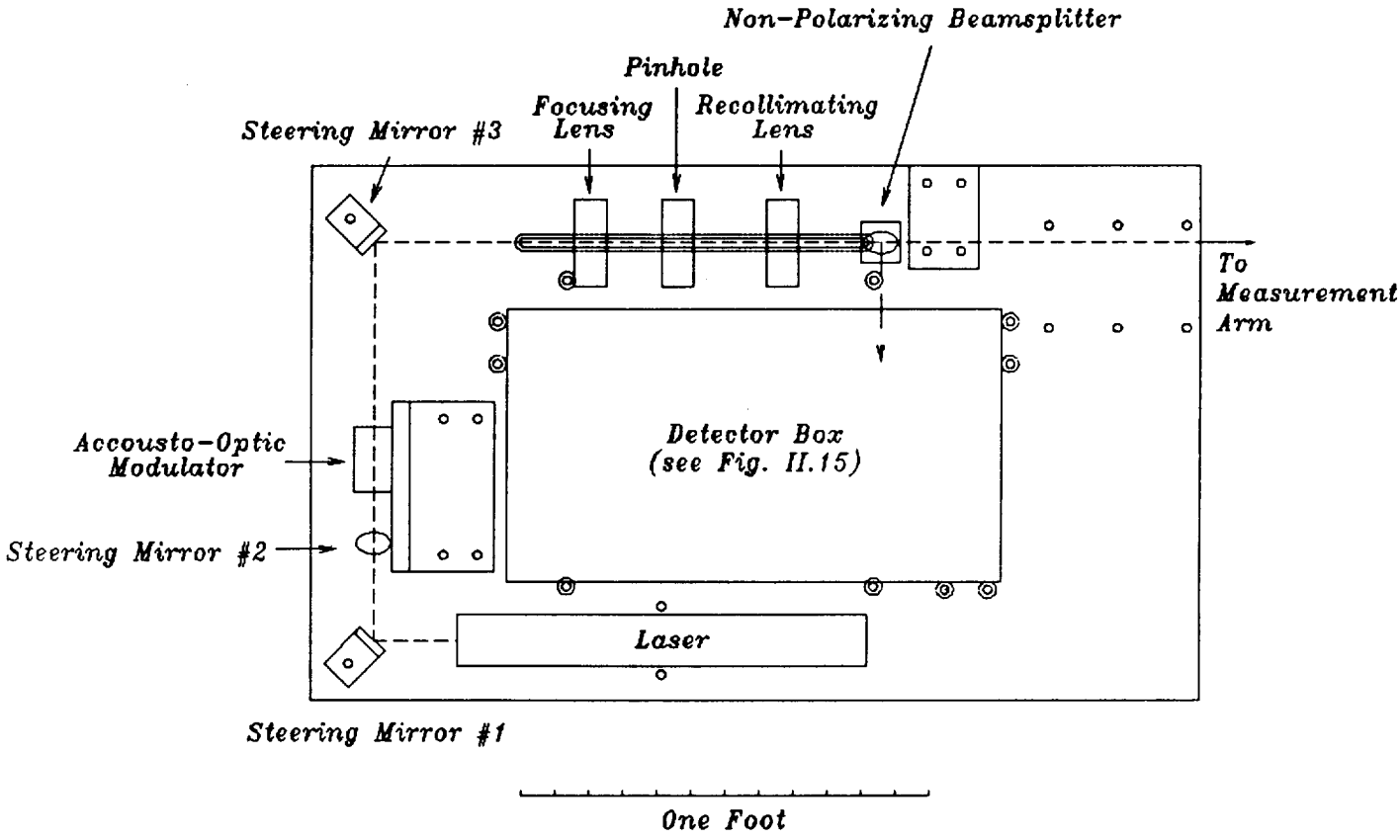

Figure II.14 Optical baseplate top view.

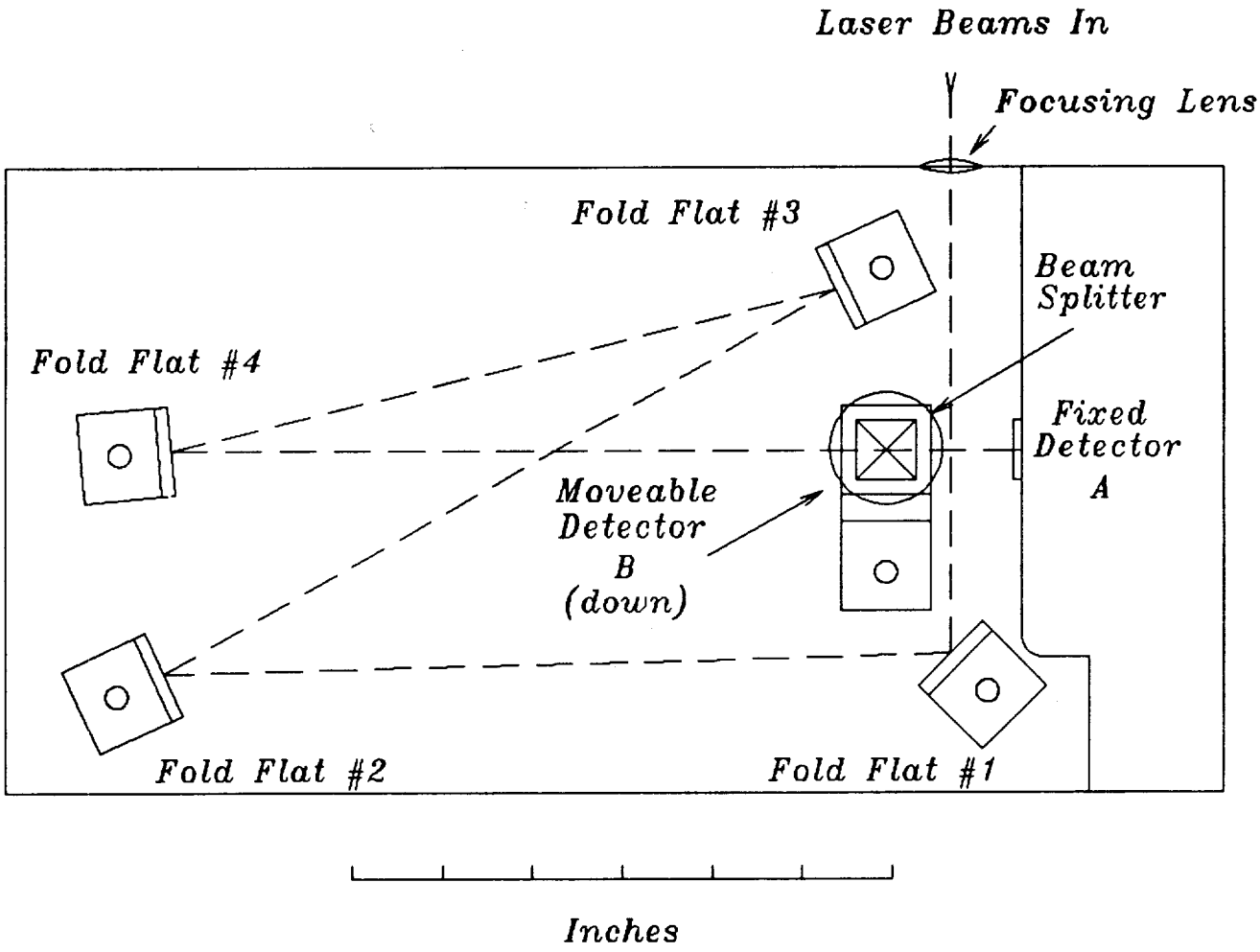

Figure II.15 Detector box top view.

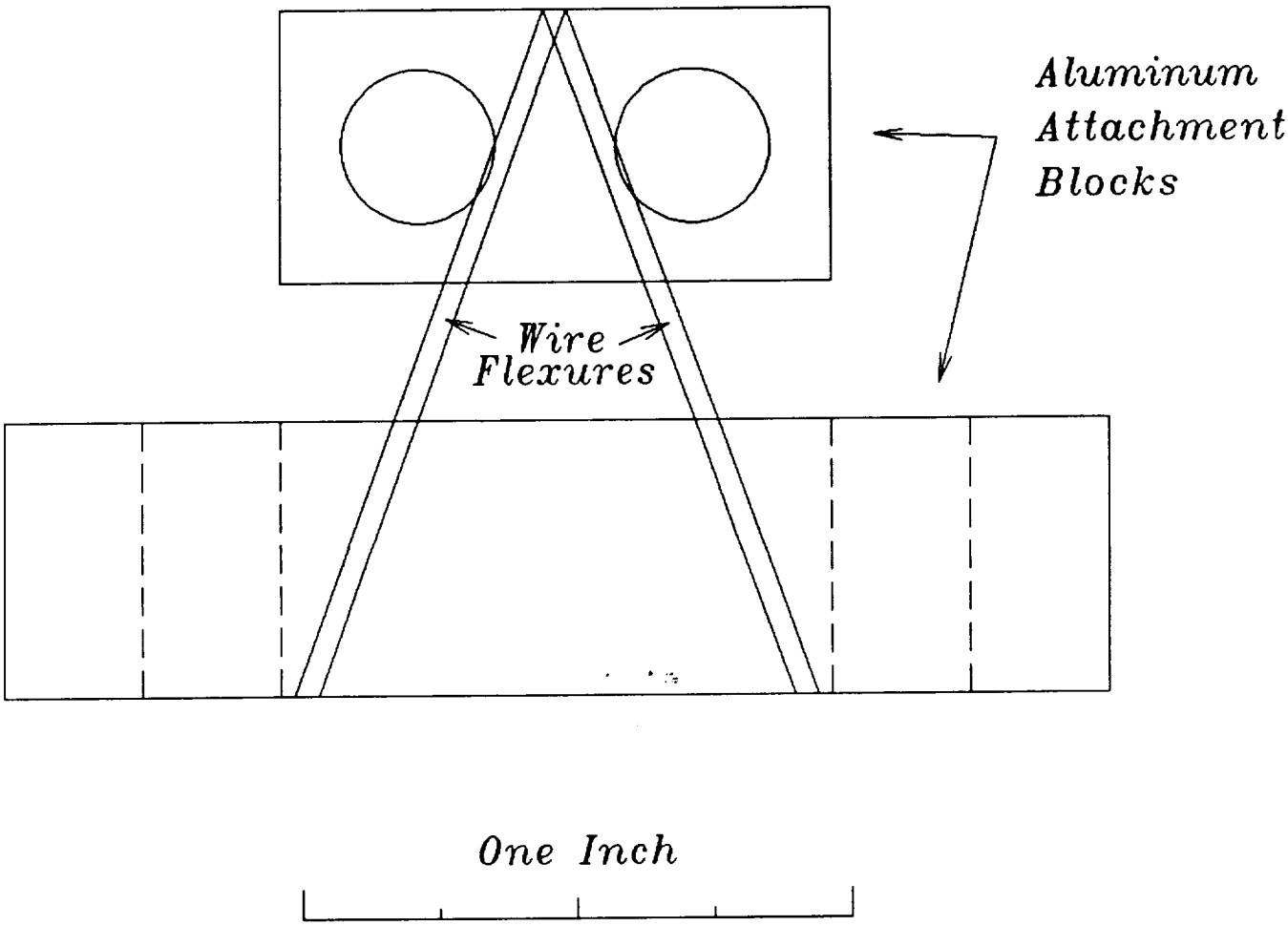

Figure II.16 Flexure bipod side view.

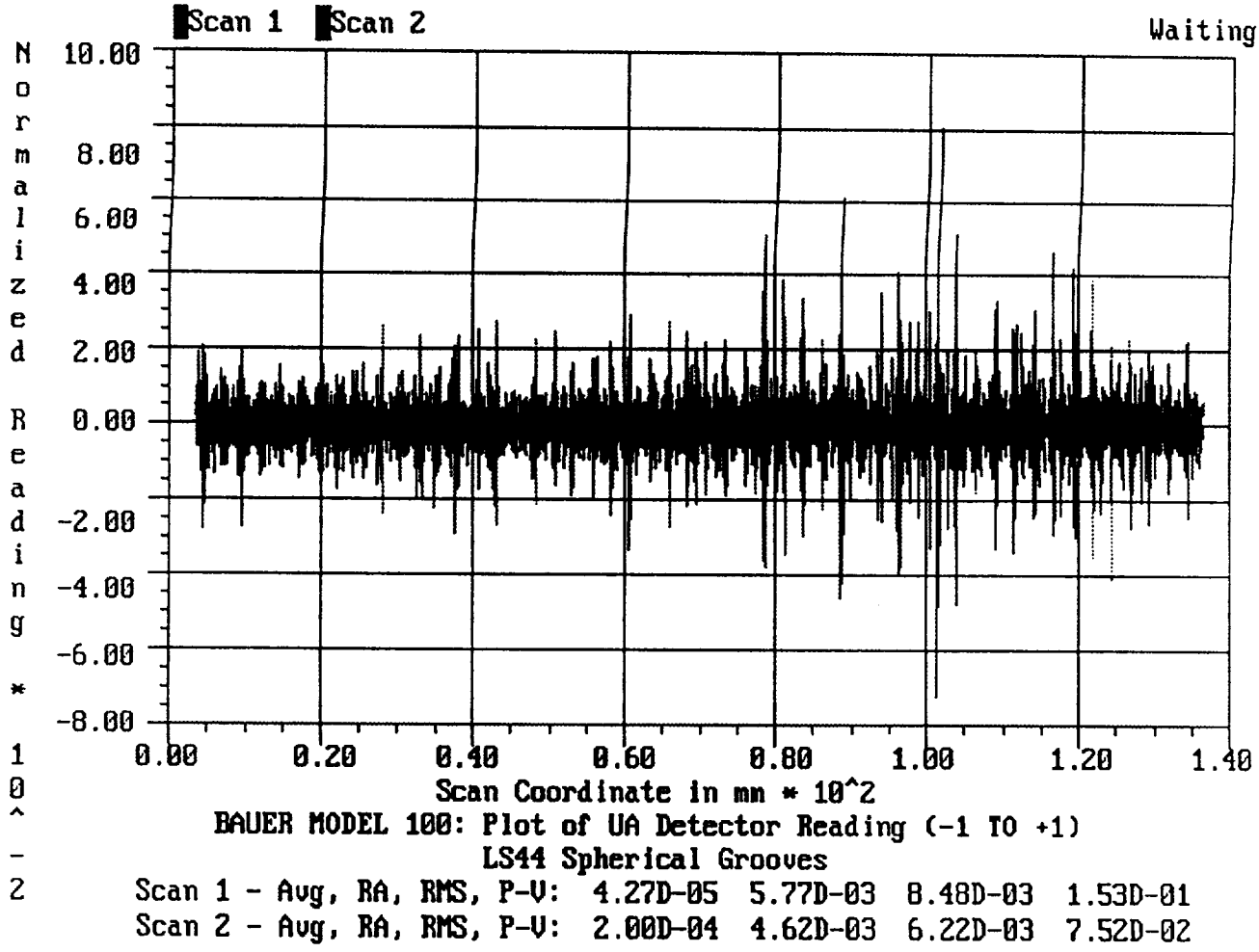

Figure II.17 Sample raw detector data profile.

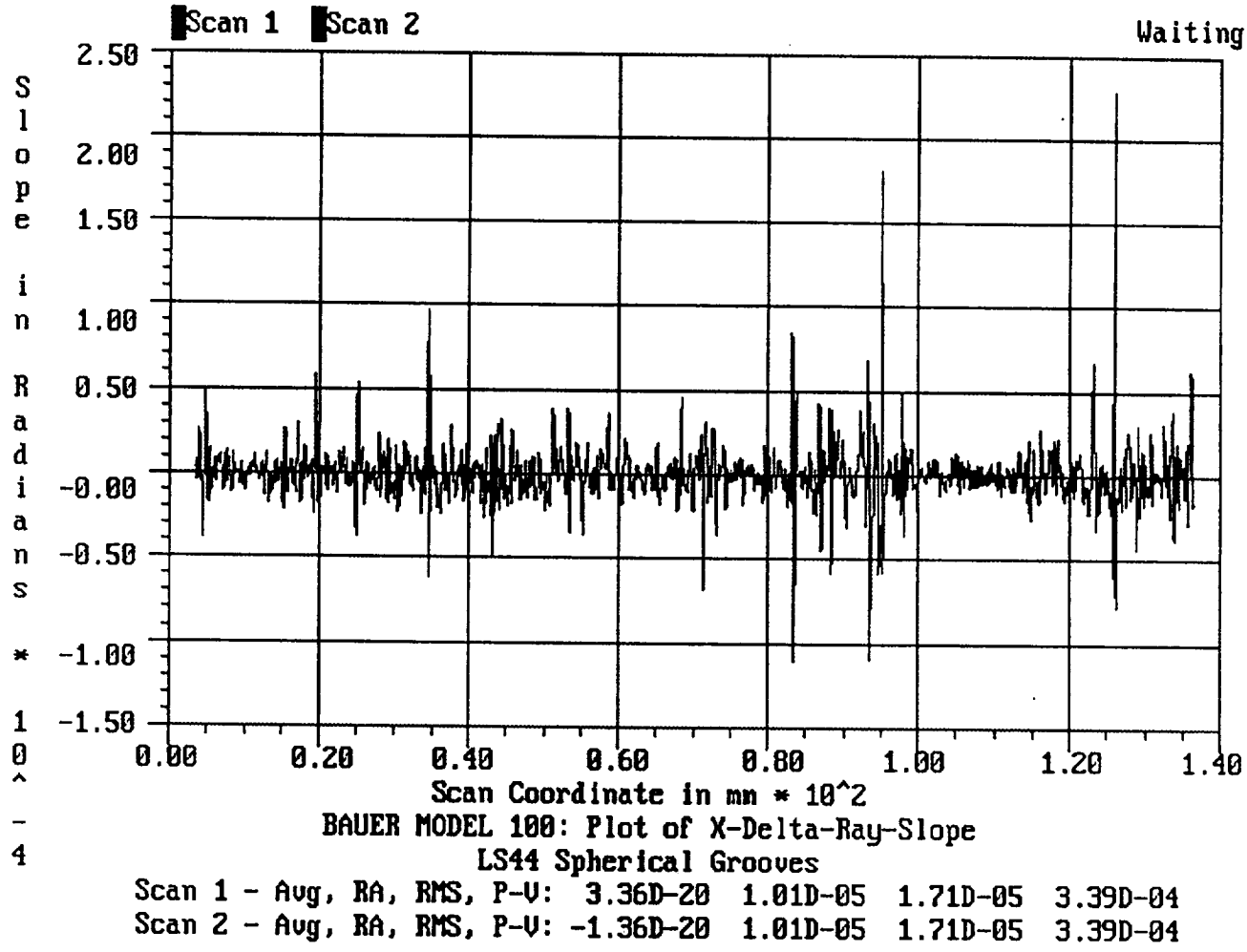

Figure II.18 Sample delta-ray-slope (curvature) profile.

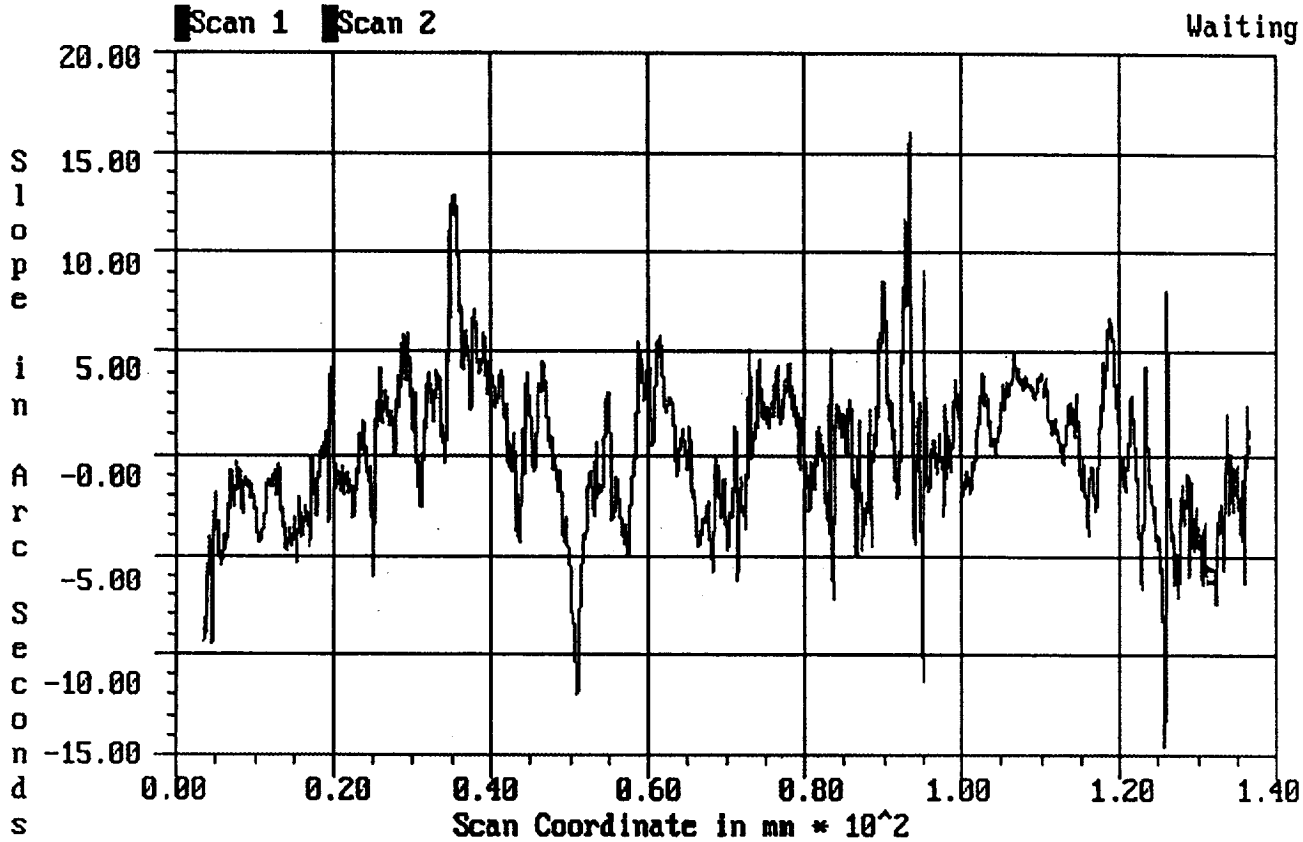

Figure II.19 Sample surface slope profile.

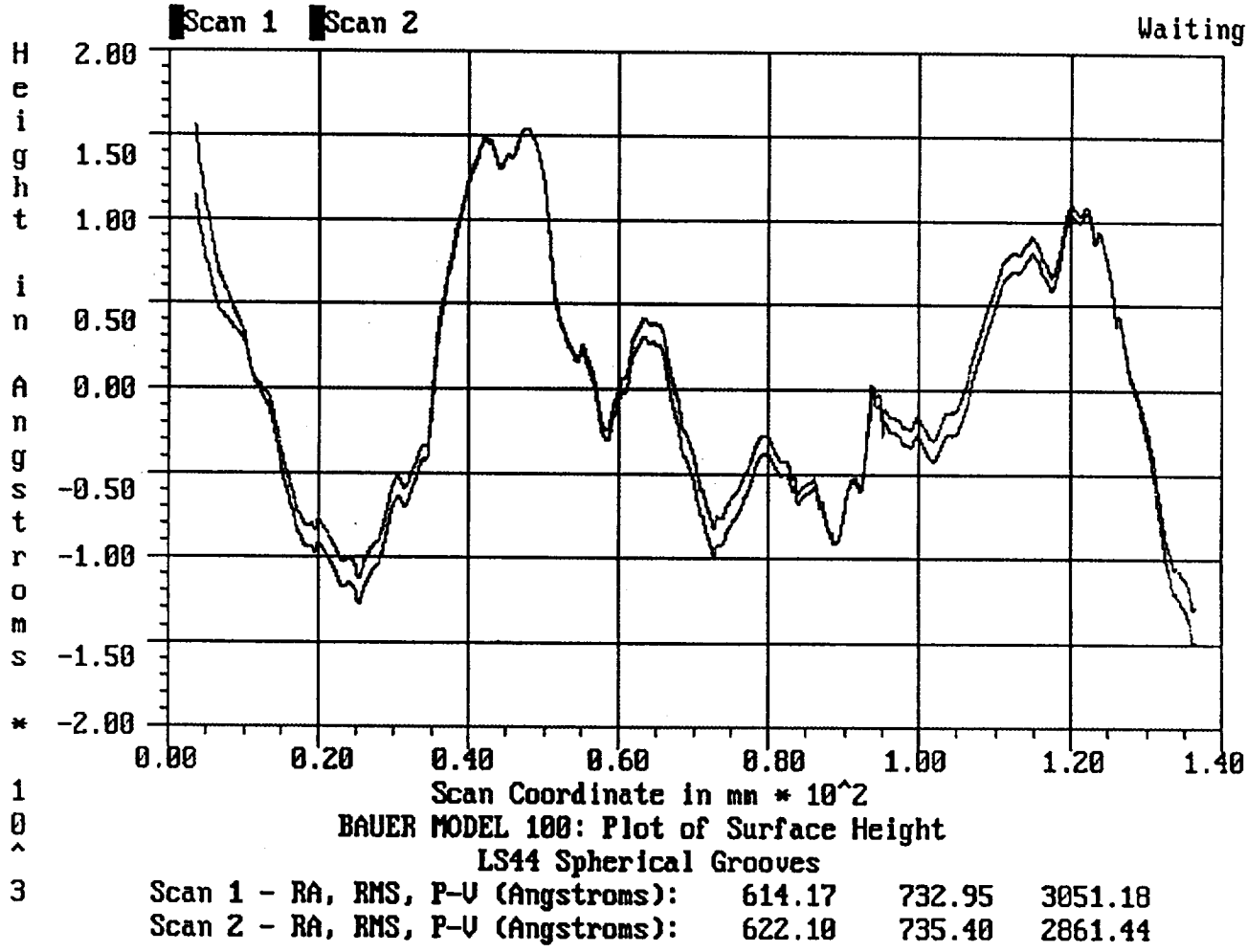

Figure II.20 Sample surface height profile.

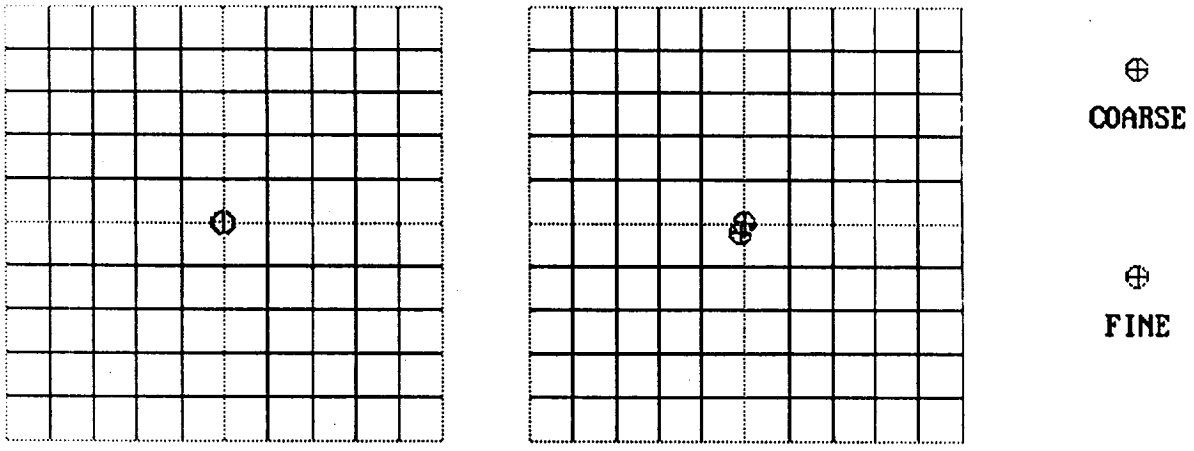

SCOPE MAGNIFCATION (1 GIVES +/- 1.0 FOR COARSE RANGE): 1.00000
CURRENT SCOPE PATTERN COARSE RANGE: +/- 1.00000
CURRENT SCOPE PATTERN FINE RANGE: +/- .10000

DETECTOR A:	X	Y	DETECTOR B:	X	Y
-1 TO 1:	-.000116	-.000225	-1 TO 1:	-.006808	.027265
POS'N (MM):	-.000133	-.000258	POS'N (MM):	-.007813	.031293

HIT 'M' FOR NEW SCOPE MAGNIFICATION HIT 'Q' TO QUIT

Figure II.21 Display from the SCOPE program.

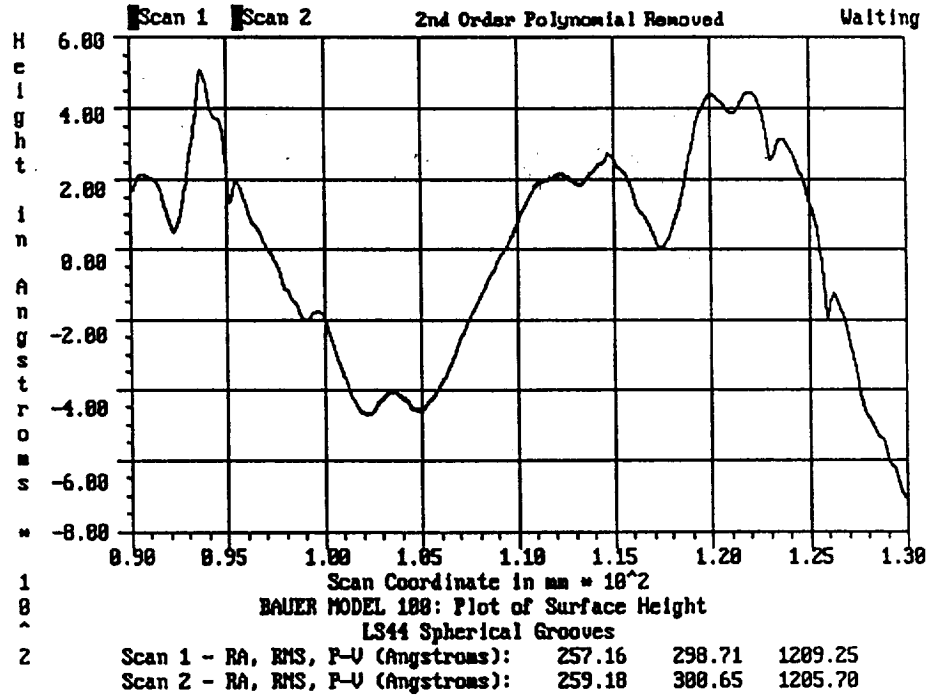

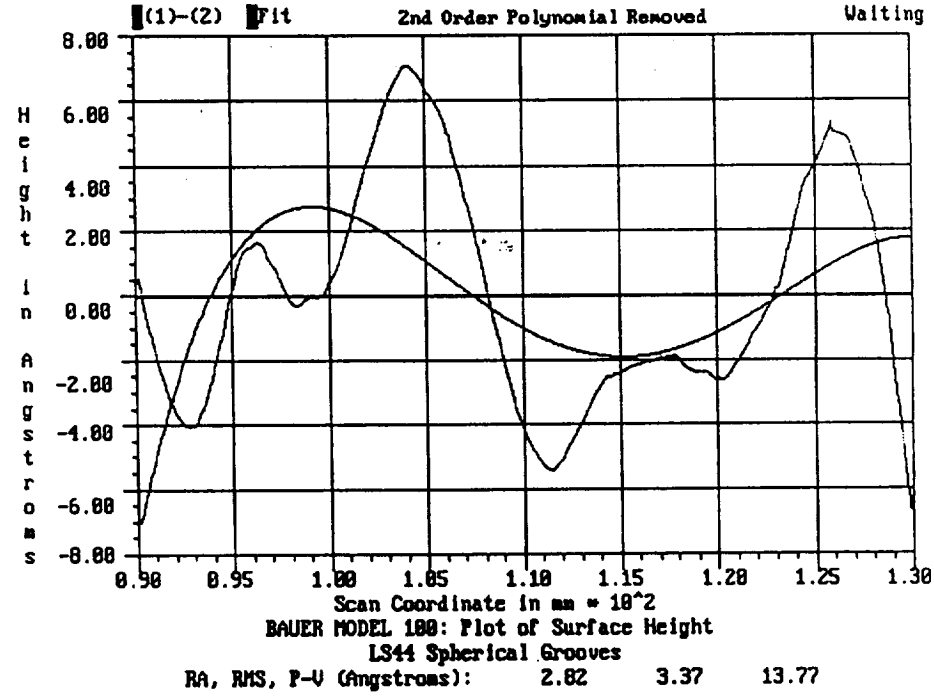

Figure II.22 40 mm surface profiles and difference plot. Base curvature has been removed from the profiles.

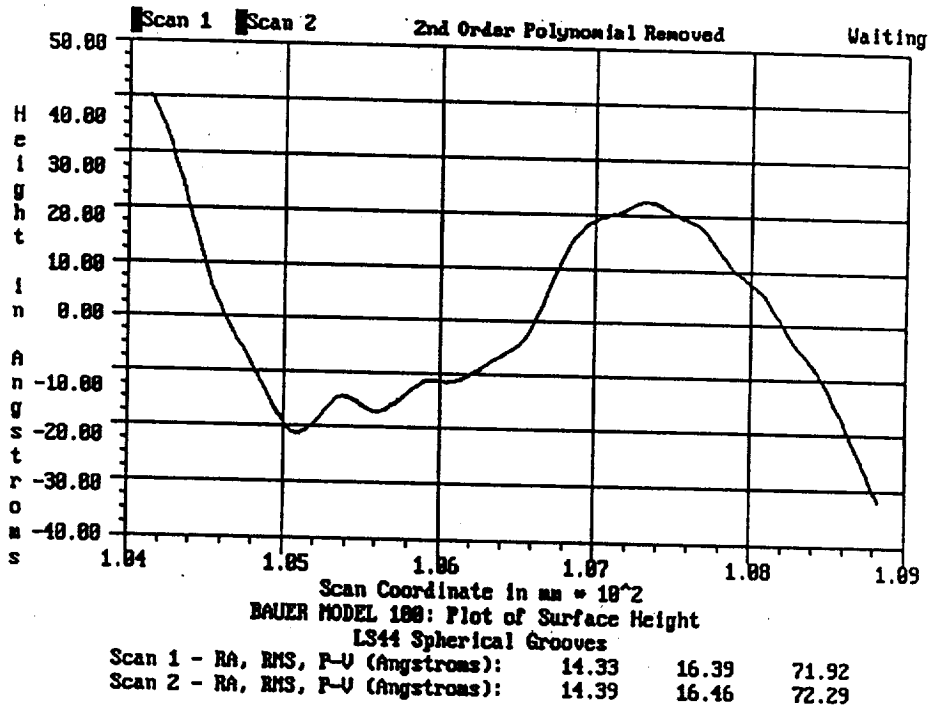

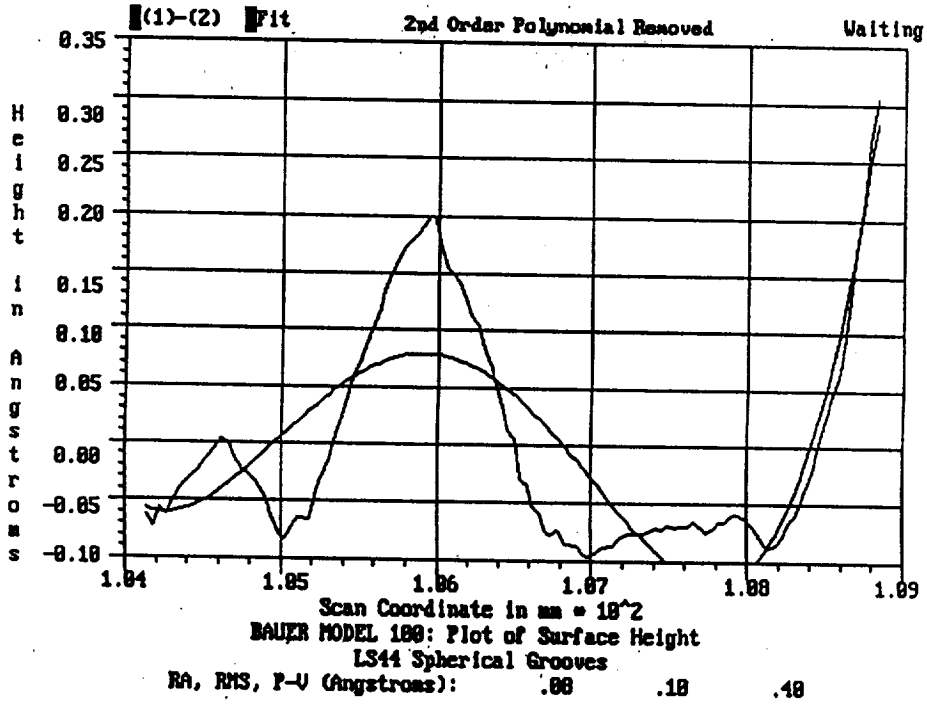

Figure II.23 5 mm surface profiles and difference plot. Base curvature has been removed from the profiles.

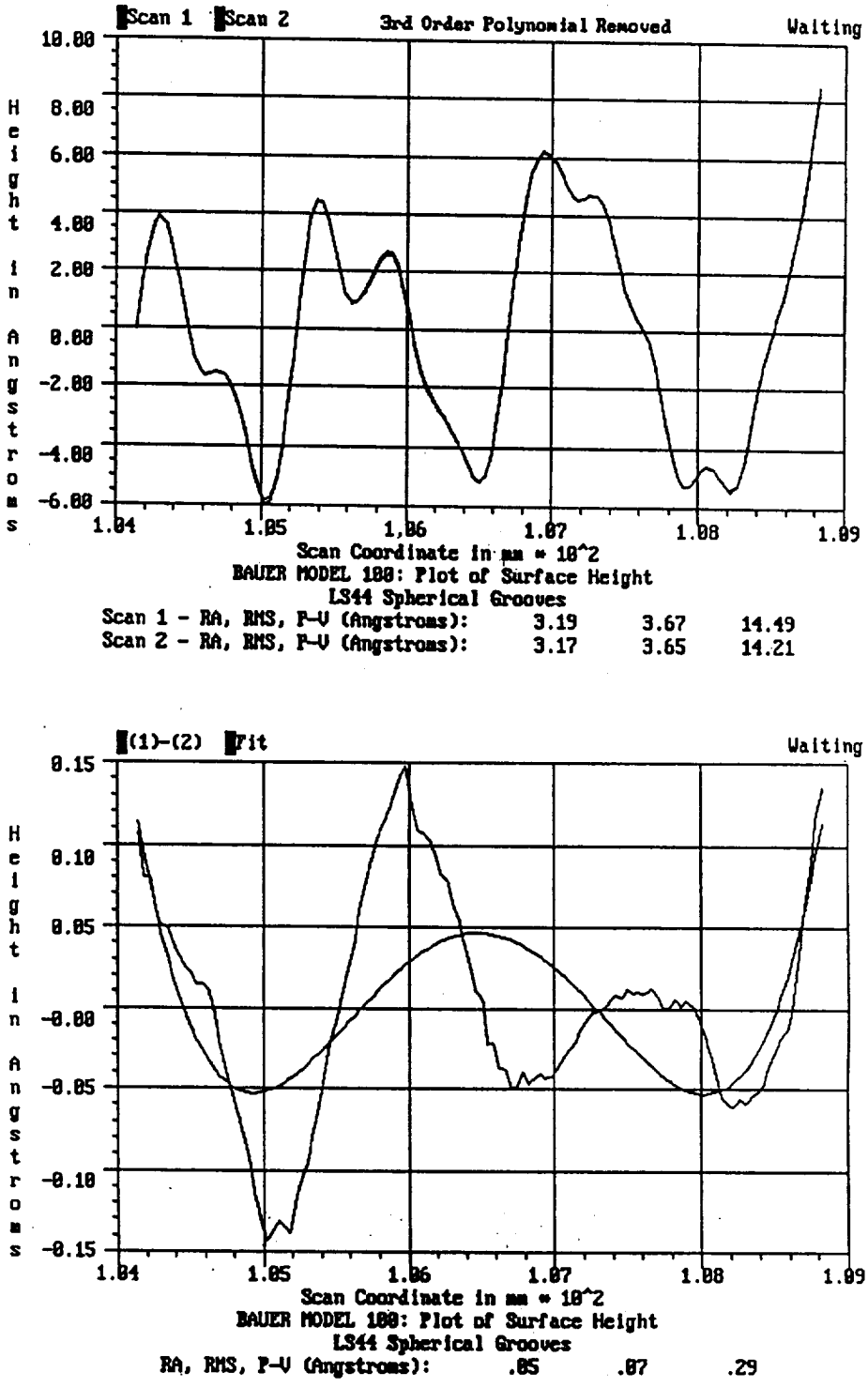

Figure II.24 5 mm surface profiles and difference plot. All third order polynomial content has been removed from the profiles.

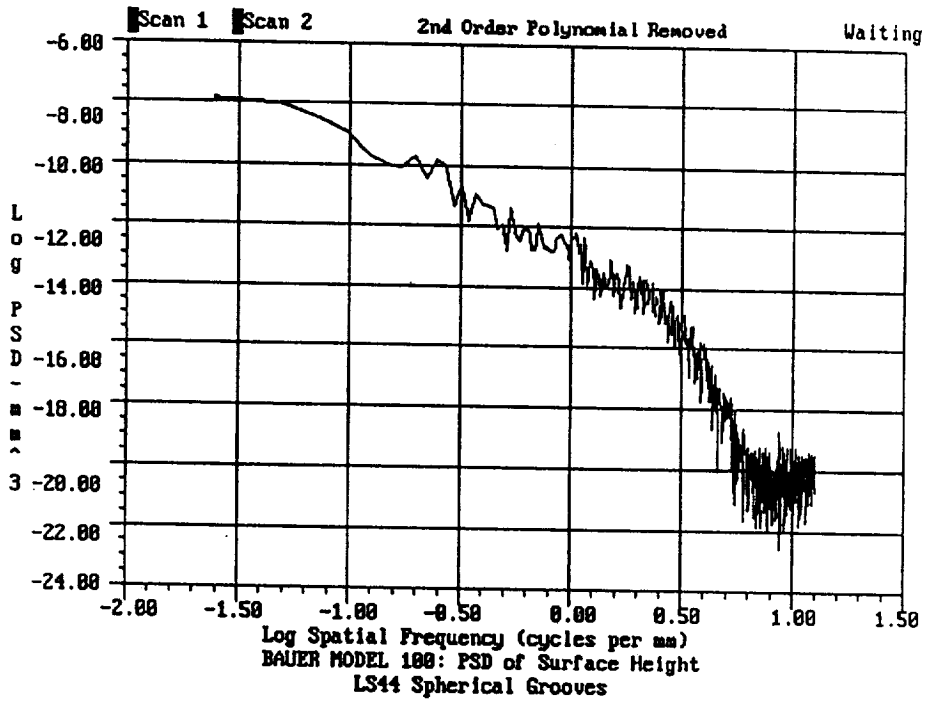

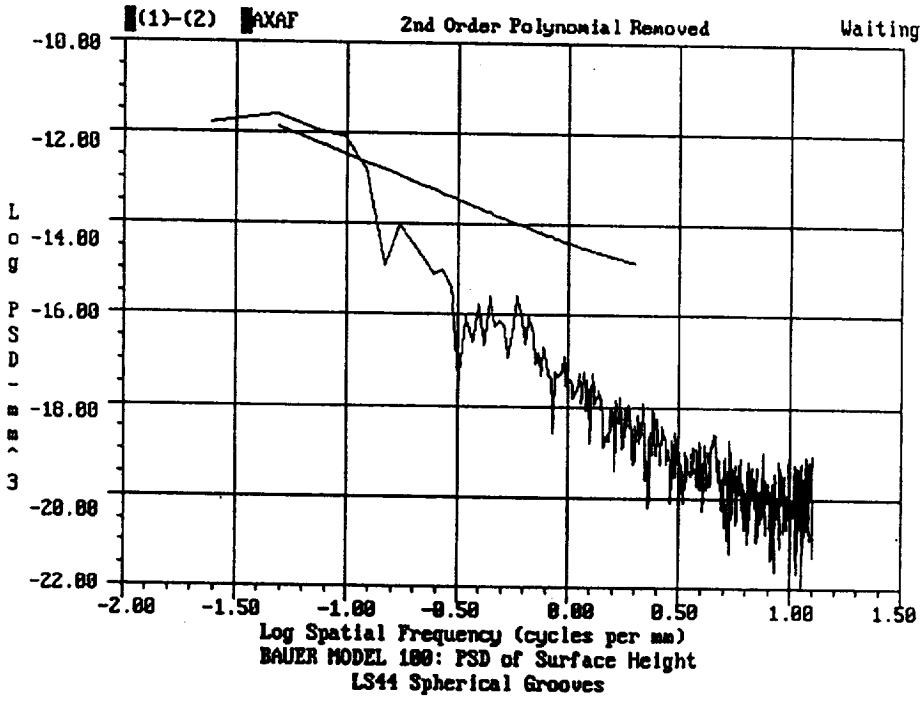

Figure II.25 PSD's for 40 mm profiles and their difference.

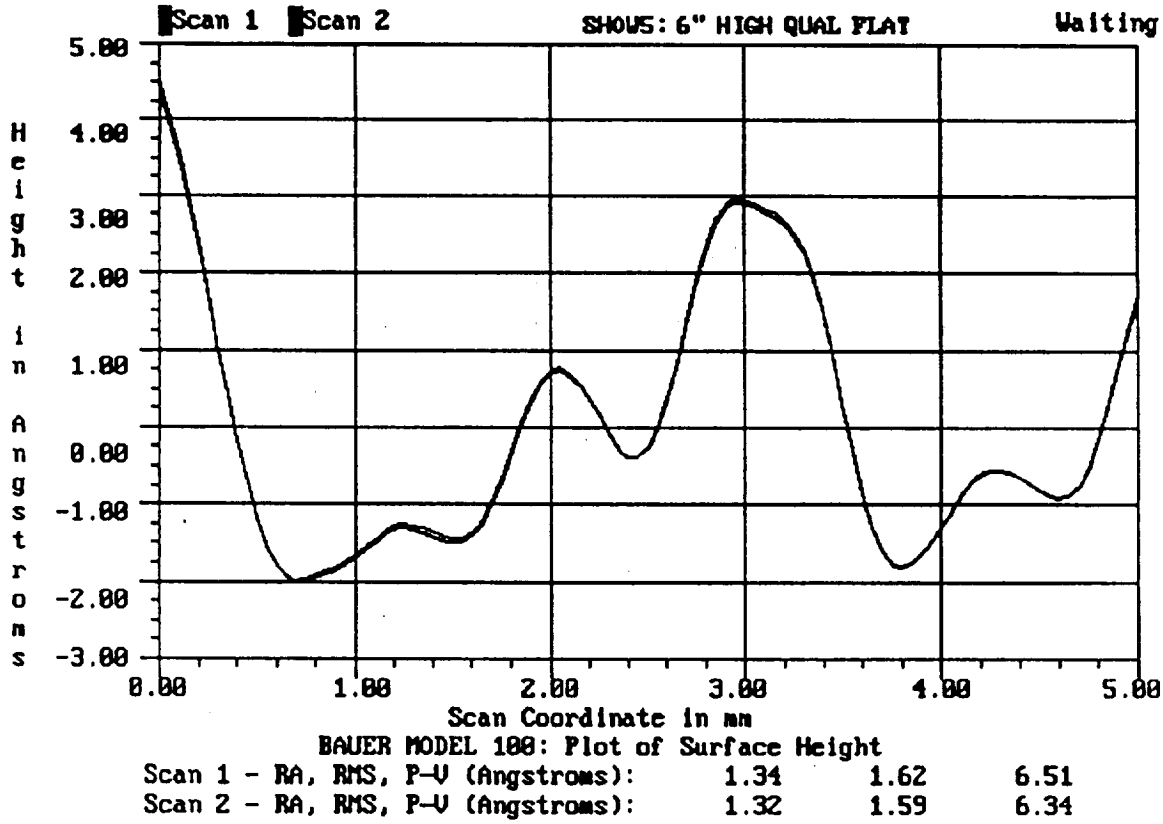

Figure II.26 Profiles of high quality 6" glass flat. Scan length is 5 mm. This very short scan shows the unprecedented sensitivity and repeatability in detecting midfrequency surface errors. Using a very short scan length of only 5 mm, the two successive profiles are nearly identical, with an RMS difference of only one-twentieth of an Angstrom. Note the spatial filtering performed naturally by the instrument, effectively eliminating all features with periods less than one-third mm. Average curvature of the test piece has been removed from the profiles. As shown, the surface quality under these conditions is approximately 1.6 Angstroms RMS.

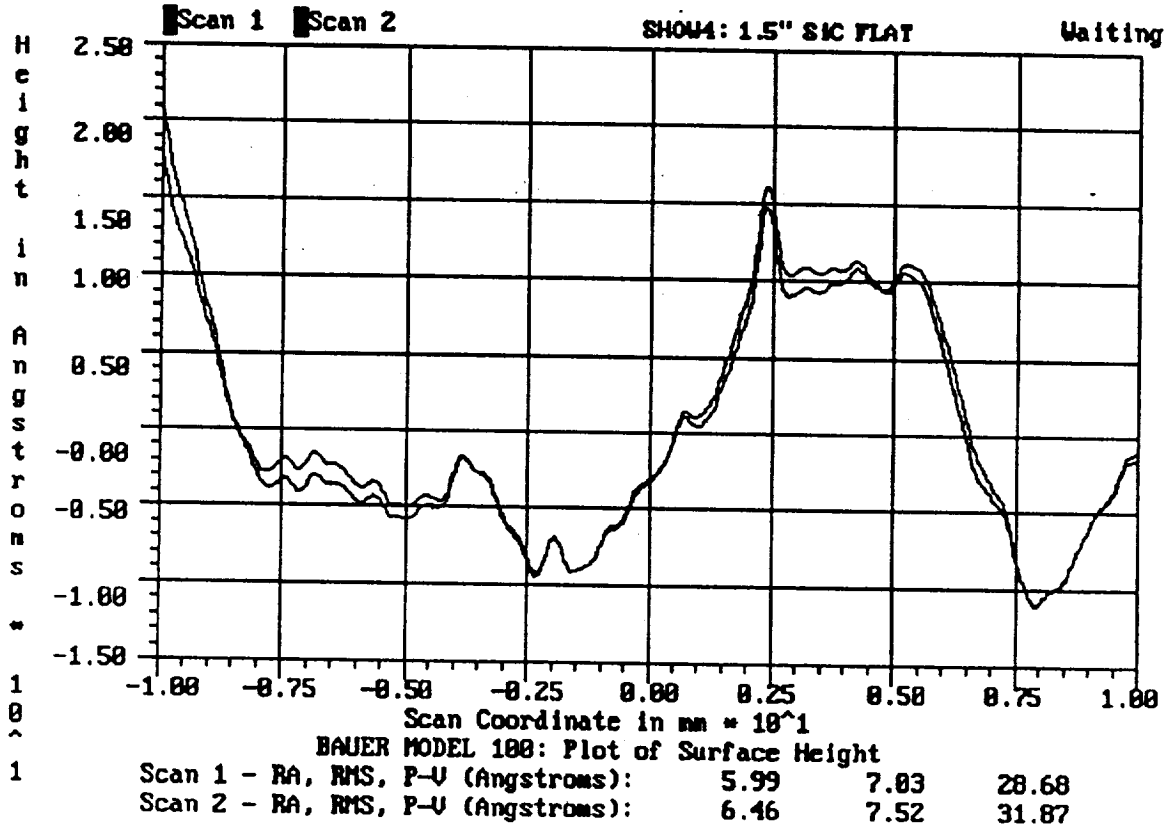

Figure II.27 Profiles of 1.5" silicon carbide flat. Scan length is 20 mm. This scan shows the excellent sensitivity and repeatability for a scan length between the 5 mm in Figure II.26, and the 132 mm in Figure II.28. Average curvature of the test piece has been removed from the profiles. As shown, the surface quality under these conditions is approximately 7 Angstroms RMS.

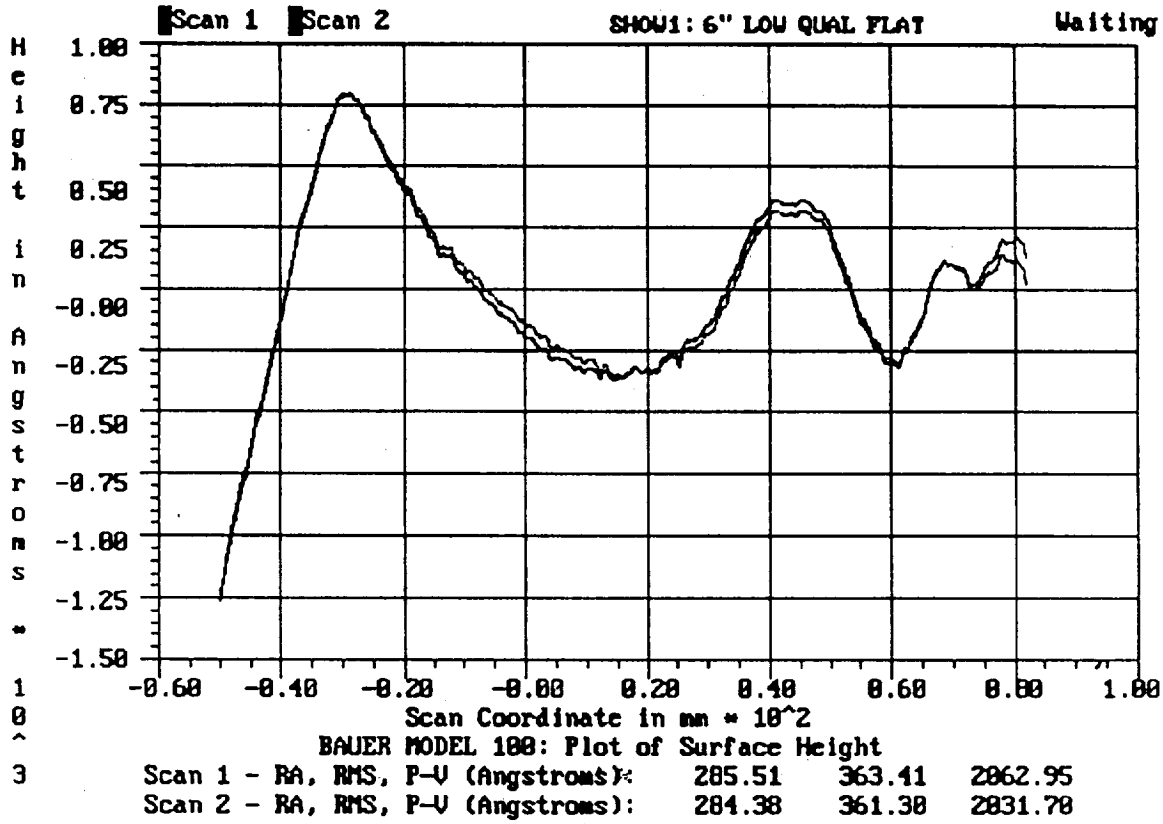

Figure II.28 Profiles of low quality 6" glass flat. Scan length is 132 mm. This full length scan shows the ability to acquire much longer profiles, even on test surfaces with lower surface quality. In this test, a one-third wave flat was scanned over essentially its entire diameter. The sensitivity and repeatability are excellent. Average curvature of the test piece has been removed from the profiles. As shown, the surface quality under these conditions is approximately 360 Angstroms RMS.

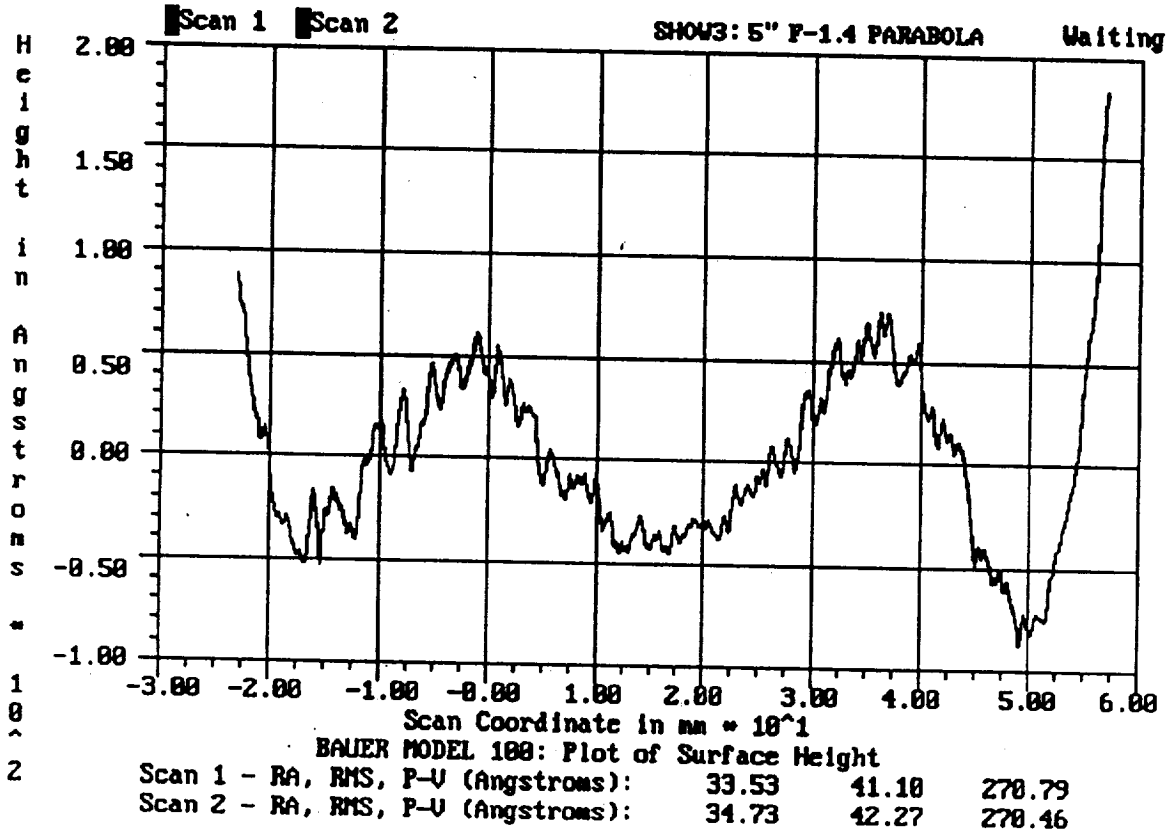

Figure II.29 Profiles of 5" F-1.4 Zerodur parabola. Scan length is 80 mm. This scan shows the ability to test steep aspheres. Note the extremely good repeatability, even when compared to the remarkably good surface quality of approximately lambda over one hundred fifty RMS. Polynomial errors through fourth order, corresponding to third order spherical aberration, have been removed from the profiles. As shown, the surface quality under these conditions is approximately 40 Angstroms RMS.

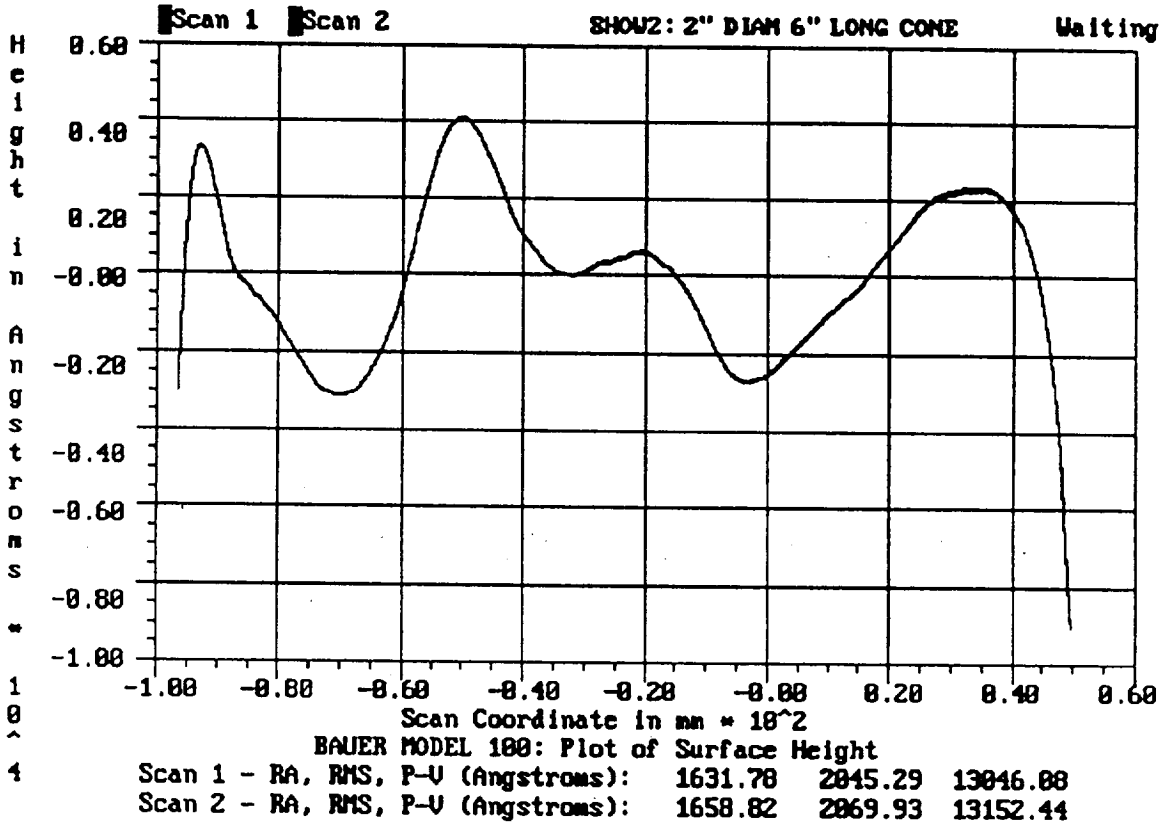

Figure II.30 Profiles of 6" aluminum cone. Scan length is 146 mm. This scan shows the ability to test the most exotic optics. The test piece is a nearly cylindrical aluminum mandrel for replicating X-ray optics. The profiles are axial and cover essentially the entire length of the piece. Polynomial errors through sixth order have been removed from the profiles. As shown, the surface quality under these conditions is approximately 2000 Angstroms RMS.

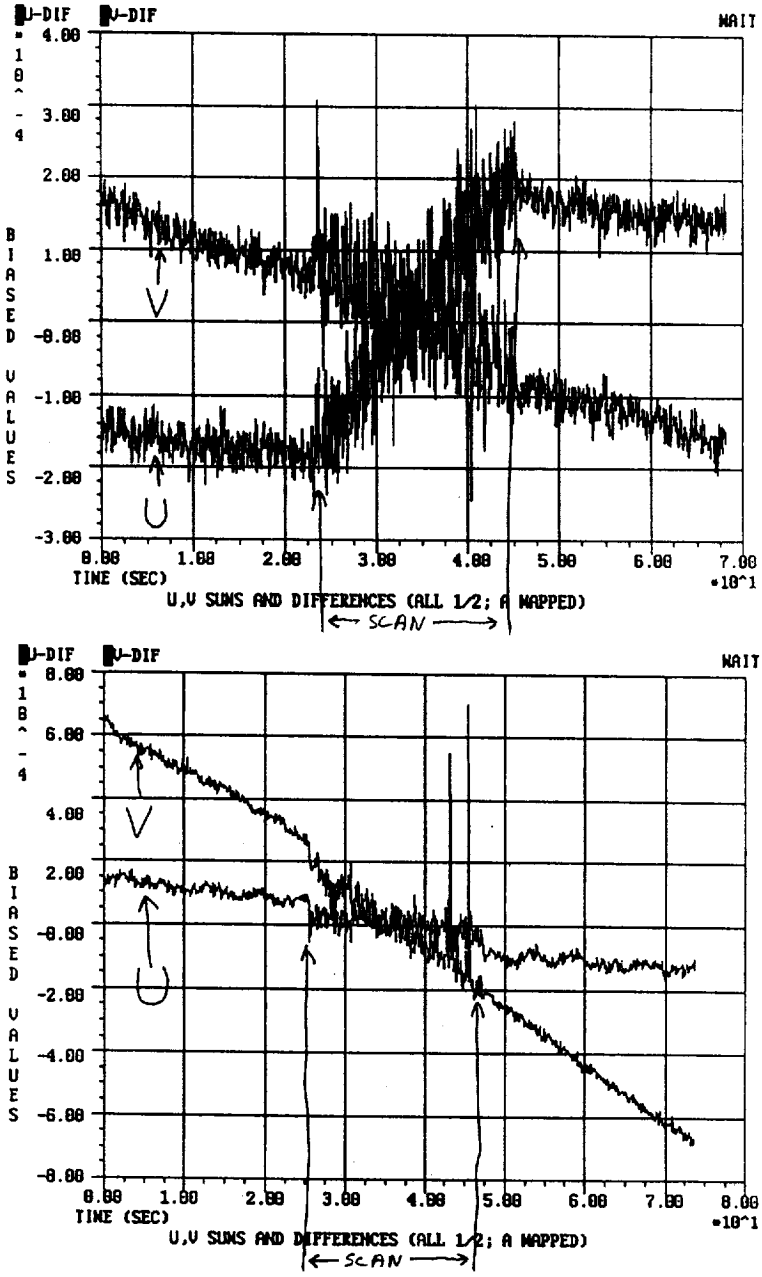

Figure II.31 Drift from distortion of the baseplate. Shown are two plots of measured curvature as a function of time during a constant velocity scan. (Thus the plots can be thought of as measured curvature as a function of scan location.) The plots were made with no calcite. The first plot corresponds to bolting the optics baseplate directly to the stage, while the second plot corresponds to a flexure attachment. Note the tremendous improvement. Note also that there is still some residual jitter, which is due to scanning related vibrations and is unimportant.

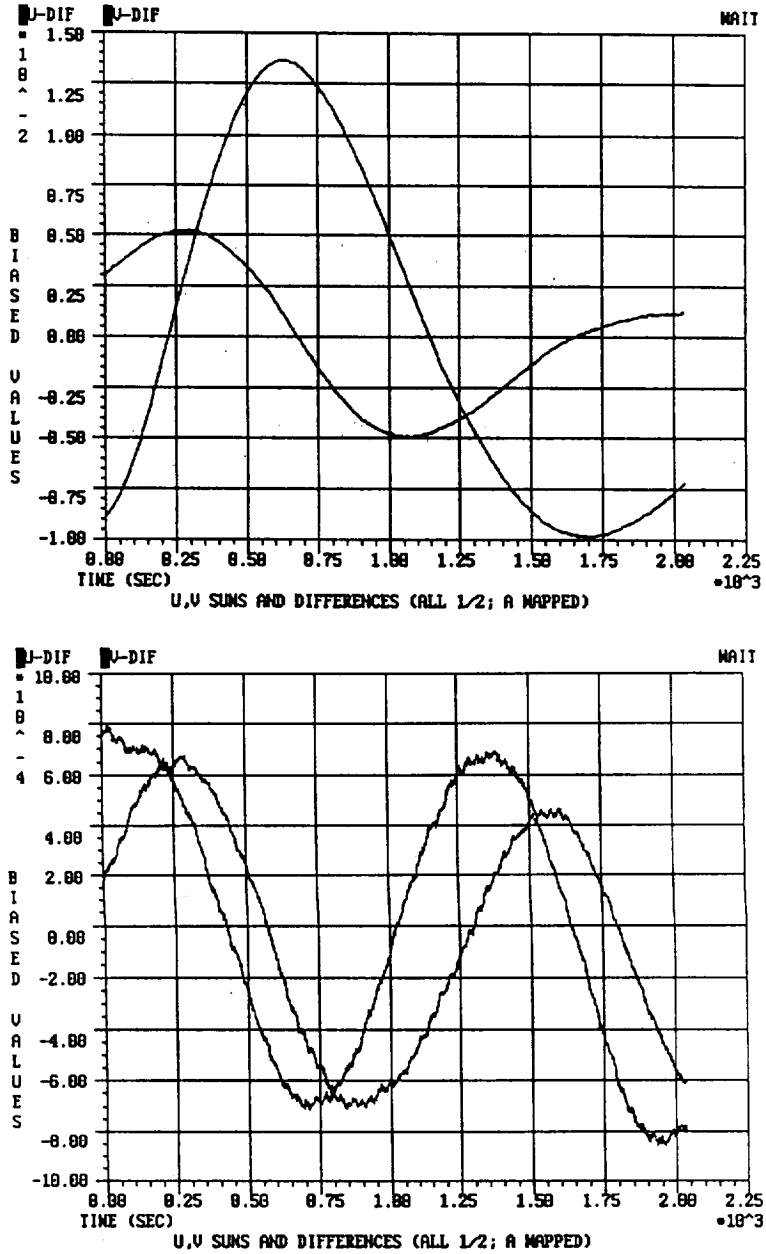

Figure II.32 Drift from AOM birefringence thermal variation. Shown are plots of drift before and after we instituted the polarization alignment step. Note the factor of 15 improvement.

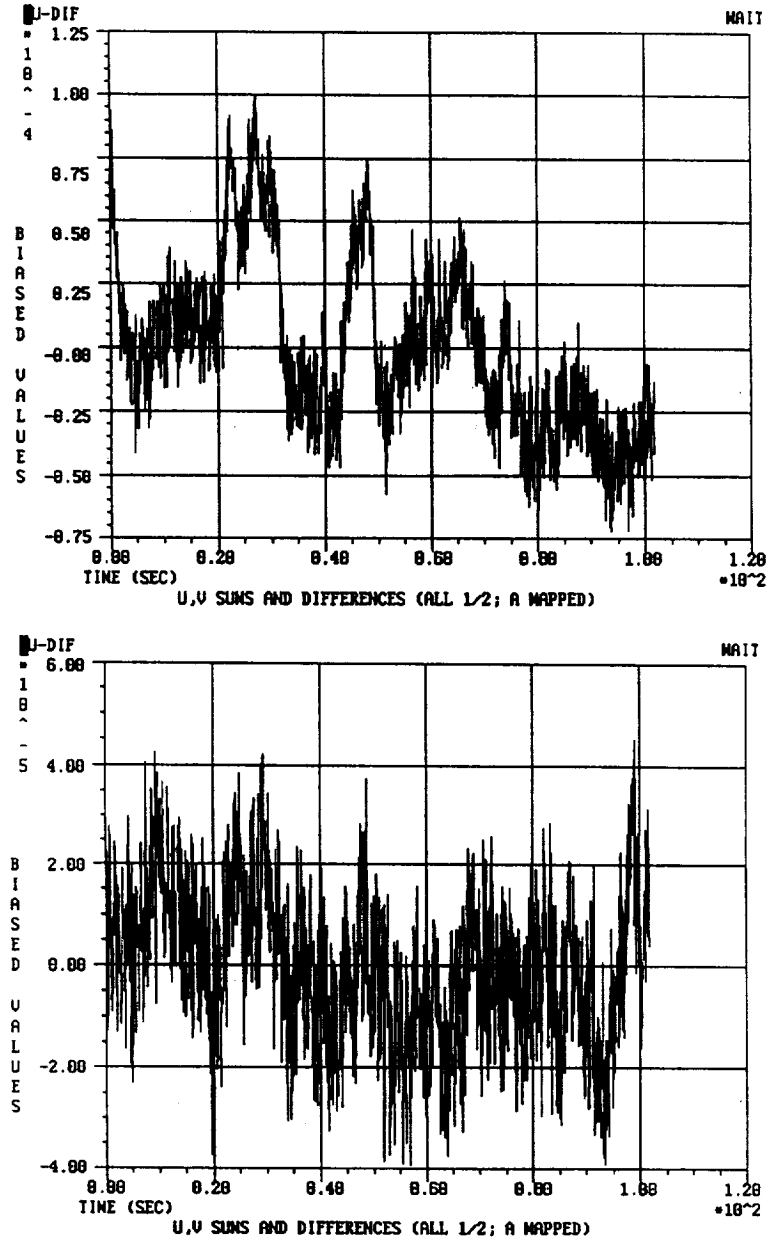

Figure II.33 Plots showing mild residual drift, and no drift.

NASA National Aeronautics and Space Administration

Report Documentation Page

1. Report No.	2. Government Accession No.	3. Recipient's Catalog No.

4. Title and Subtitle

Development of a Measurement of Upper Mid Frequency Errors on Arbitrary Grazing Incidence Optics - Final Report

5. Report Date

12/5/90

6. Performing Organization Code

7. Author(s)

Paul Glenn

8. Performing Organization Report No.

10. Work Unit No.

9. Performing Organization Name and Address

Bauer Associates, Inc.
177 Worcester Rd., Suite 101
Wellesley, MA 02181

11. Contract or Grant No.

NAS5-30311

13. Type of Report and Period Covered

Final: 10/88-10/90

12. Sponsoring Agency Name and Address

(NASA, Washington, DC 20546-0001)
NASA Goddard Space Flight Center
Greenbelt Rd, Greenbelt, MD 20771

14. Sponsoring Agency Code

15. Supplementary Notes

16. Abstract

The project was a great success. We developed two state-of-the-art subsystems (detection and servo), and achieved performance generally more than an order of magnitude better than comparable commercial subsystems. Most importantly, though, the breadboard instrument measured more than an order of magnitude more accurately than the original 1 Angstrom goal within the primary spatial period range. We took extensive measurements, and defined a useful set of Phase III modifications.

17. Key Words (Suggested by Author(s))	18. Distribution Statement
Detector, Synchronous Detection, Servo, Beam Steering, Subsystem Demonstration	Not available to public

19. Security Classif. (of this report)	20. Security Classif. (of this page)	21. No. of pages	22. Price
none	none	97	

NASA FORM 1626 OCT 86